

COMPARISON OF AIRBORNE SURVEYING TECHNIQUES FOR MAPPING SUBMERGED
OBJECTS IN SHALLOW WATER

A Thesis

by

BEHROKH NAZERI

BS, KHAJEH NASIREDDIN TOOSI UNIVERSITY, IRAN, 2000

Submitted in Partial Fulfillment of the Requirements for the Degree of

MASTER OF SCIENCE

in

GEOSPATIAL SURVEYING ENGINEERING

Texas A&M University-Corpus Christi
Corpus Christi, Texas

August 2016

© Behrokh Nazeri

All Rights Reserved

August 2016

COMPARISON OF AIRBORNE SURVEYING TECHNIQUES FOR MAPPING SUBMERGED
OBJECTS IN SHALLOW WATER

A Thesis

by

BEHROKH NAZERI

This thesis meets the standards for scope and quality of
Texas A&M University-Corpus Christi and is hereby approved.

Michael Starek, PhD
Chair

Richard Smith, PhD
Committee Member

Gary Jeffress, PhD
Committee Member

August 2016

ABSTRACT

In this study, bathymetric lidar, high resolution aerial imagery, and hyperspatial resolution imagery collected from a small unmanned aircraft system (UAS) were examined in order to delineate submerged objects in shallow coastal water. A region surrounding Shamrock Island in Corpus Christi Bay along the Texas Gulf Coast was chosen for this study. This area is significant because of the existence of submerged structures including oil pipelines, which may influence the marine environment and navigation in shallow water. Therefore, mapping submerged structures is the first step of any further study in this area in terms of environmental litter and navigation hazards.

Different methods were compared to each other in these categories in terms of efficiency and accuracy to map the bathymetric surface and detect submerged structures. First, three different interpolation methods including 2D Delaunay triangulated irregular network (TIN), inverse distance weight (IDW), and multilevel B spline were used to create digital elevation models (DEMs) using airborne lidar data to investigate their use on submerged pipeline detection. Then three different algorithms including Sobel, Prewitt, and Canny were examined in edge detection image processing to illustrate the potential pipelines using aerial imagery. To improve visibility, glint correction methods were implemented and compared to non-glint corrected imagery for pipeline delineation. Finally, a small UAS equipped with a digital camera was flown to evaluate structure from motion (SfM) photogrammetry for bathymetric mapping in the shallow bay. Methods examined included glint corrected imagery and single bands vs. original multiband imagery. The goal was to determine the effectiveness of image pre-

conditioning methods for improving UAS-SfM mapping of submerged bottom and structures in shallow water.

Results showed that B-spline interpolation method was the best fit compared to other methods for deriving bathymetric DEMs from the airborne lidar data. In edge detection image processing, Canny method performed better between all three methods in detecting the pipelines in the aerial imagery. In the last part, using glint removal methods and green single band imagery as inputs into the UAS-SfM photogrammetry workflow increased the quality of the produced point cloud over shallow water in terms of point density and depth estimation respectively.

In conclusion, bathymetric lidar data in fusion with aerial imagery improved the pipeline delineation. Due to inherent limitations in current bathymetric lidar system resolution power, it is recommended that future surveys targeted for this objective plan as best as possible for ideal water conditions in terms of visibility, employ more scan overlap. Sun glint correction improved the quality of the imagery in terms of penetrating through the water column. Avoiding sun glint by choosing appropriate place and time for data collection is the best way to deal with sun glint. In the UAS-SfM part, using a polarized filter on RGB cameras is recommended to assess the sun glint effect in the result.

INDEX WORDS: Bathymetric LiDAR, Aerial Imagery, Glint removal, UAS, Structure from Motion Photogrammetry, Benthic Mapping

TABLE OF CONTENTS

CONTENTS	PAGE
ABSTRACT.....	V
TABLE OF CONTENTS	VII
LIST OF TABLES	IX
LIST OF FIGURES	X
CHAPTER	
1 Introduction.....	1
Purpose	1
Objective	1
Overview	2
2 Background and Literature Review	3
Airborne Bathymetric LiDAR.....	3
Aerial Imaging for Benthic Mapping.....	8
Edge Detection	9
Sun Glint Removal	16
UAS Structure from Motion Photogrammetry.....	21
3 Study Area and Data Set.....	25
Study Area.....	25
Data Set	26
4 Methodology.....	32
Bathymetric Lidar.....	32
Lidar data classification.....	32

DEM	36
Vertical accuracy assessment	38
DEMs assessment for delineating the pipelines	39
Aerial Digital Imaging.....	40
Sun Glint Removal	40
Edge Detection	45
UAS Structure from Motion Photogrammetry	51
5 Results and Discussion	56
Results	56
Bathymetric lidar	56
Aerial digital imagery.....	66
UAS-SfM.....	73
Discussion	85
6 Conclusion	90
7 Challenges and future work	92
ACKNOWLEDGEMENT	96
REFERENCES	97
APPENDIX 1.....	106

LIST OF TABLES

TABLES	PAGE
Table 3.1. Flight parameters	29
Table 4.1. Turbid water data classification.....	34
Table 4.2. IDW interpolation parameter setting	37
Table 4.3. Shaded relief parameter setting.....	38
Table 4.4. Canny parameters tradeoff.....	48
Table 5.1. Interpolation methods vertical accuracy-all points.....	56
Table 5.2. Interpolation methods vertical accuracy-bathymetry	56
Table 5.3. Interpolation methods vertical accuracy-land.....	57
Table 5.4. Interpolation methods vertical accuracy-vegetation	57
Table 5.5. Evaluation based on ground truth	71
Table 5.6. Evaluation based on ground truth-deglint imagery.....	74
Table 5.7. Point cloud extraction in SfM processing.....	75
Table 5.8. Key point matching.....	75
Table 5.9. Statistical parameters UAS-SfM product over water	77
Table 5.10. Statistical parameters glint removal vs original multiband over land	77

LIST OF FIGURES

FIGURES	PAGE
Figure 2.1. Bathymetric lidar system	4
Figure 2.2. Refraction through water	4
Figure 2.3. Backscattering in turbid water	5
Figure 2.4. Convolution mask in Sobel method	11
Figure 2.5. Convolution mask in Prewitt method	11
Figure 2.6. Effect of Gaussian Parameter δ in noise	13
Figure 2.7. Canny method edge directions	15
Figure 2.8. Absorption in pure water	18
Figure 2.9. Regression analysis diagram	20
Figure 2.10. Bundle Block	21
Figure 3.1. Study area	25
Figure 3.2. Leica AHAB Chitoptera II	26
Figure 3.3. Lidar data	27
Figure 3.4. Aerial imagery	28
Figure 3.5. Camera canon powershot S110	29
Figure 3.6. Flight path UAS-SfM	30
Figure 3.7. Launching eBee	31
Figure 3.8. Structure from Motion image	31
Figure 4.1. Topo-bathymetric DEM	33
Figure 4.2. Turbid water data filtering	35

Figure 4.3. Bathymetric point cloud	36
Figure 4.4. RTK GPS points	40
Figure 4.5. Hedley method workflow	43
Figure 4.6. Lyzenga method workflow	44
Figure 4.7. Convolution mask in Sobel method	45
Figure 4.8. Sobel edge detection sample	46
Figure 4.9. The horizontal and vertical Prewitt edge detection masks	46
Figure 4.10. Prewitt edge detection sample	47
Figure 4.11. Canny parameters tradeoff	50
Figure 4.12. UAS-SfM workflow	55
Figure 5.1. B-Spline interpolation DEM	58
Figure 5.2. B-Spline interpolation DEM.....	59
Figure 5.3. B-Spline interpolation DEM.....	60
Figure 5.4. 2D Delaunay DEM.....	61
Figure 5.5. IDW DEM	62
Figure 5.6. DEM color coded by elevation-B-spline	64
Figure 5.7. DEM color coded by elevation- TIN.....	65
Figure 5.8. DEM color coded by elevation-IDW	66
Figure 5.9. Glint corrected result	67
Figure 5.10. Spectral analysis glint removal effect.....	68
Figure 5.11. Glint corrected mosaic.....	69
Figure 5.12. Sobel and Prewitt ground truth.....	70
Figure 5.13. Canny edge detection result and ground truth.....	71

Figure 5.14. Glint corrected effect on edge detection.....	73
Figure 5.15. Spectral analysis: UAS-SfM	75
Figure 5.16. Distribution of original multiband	77
Figure 5.17. Distribution of the red band	77
Figure 5.18. Distribution of the NIR band	77
Figure 5.19. Distribution of the green band	78
Figure 5.20. Distribution of the Hedley method	78
Figure 5.21. Distribution of the Lyzenga method	78
Figure 5.22. Original multiband point cloud and shaded relief	79
Figure 5.23. Glint corrected_ the Hedley 2005 point cloud and shaded relief	79
Figure 5.24. Glint corrected_ the Lyzenga 2006 point cloud and shaded relief.....	80
Figure 5.25. Original multiband image UAS-SfM product	80
Figure 5.26. The Lyzenga method UAS-SfM product	81
Figure 5.27. Hedley method UAS-SfM produc	81
Figure 5.28. Single band (green) UAS-SfM product	81
Figure 5.29. Single band (red) UAS-SfM product.....	82
Figure 5.30. Single band (NIR) UAS-SfM product.....	82
Figure 5.31. Comparing DEM results (NIR – Green)	83
Figure 5.32. Comparing DEM results (Green – Original multiband).....	83
Figure 5.33. Comparing DEM results (Hedley – Original multiband).....	83
Figure 5.34. Comparing DEM results (Lyzenga – Original multiband).....	84
Figure 5.35. Comparing DEM results (NIR – Original multiband).....	84
Figure 5.36. Comparing DEM results (Red – Original multiband).....	84

Figure 5.37. Comparing DEM results (Red – Green).....	85
Figure 5.38. Final result	86
Figure 7.1. Schematic view of rays.....	94

CHAPTER 1

INTRODUCTION

1.1 Purpose

Mapping benthic features using aerial and satellite images began several decades ago. Detection of features has been changed from visual interpretation to automated or semi-automated detection. For example, airborne light detection and ranging (lidar) data has proven to be highly effective in topographic mapping and, complementing aerial and satellite image information (Rodríguez-Cuenca & Alonso, 2014). Methods have been developed to model, measure, and predict different variables including water surface levels, water depth (bathymetry), and submerged structures. Comprehensive knowledge of water depth, or underwater topography respectively, is essential for many research fields that work offshore (Doneus et al., 2013). Bathymetric information is of fundamental importance to coastal and marine planning and management, nautical navigation, and scientific studies of marine environments. Monitoring navigation channels for shipping traffic safety and mapping underwater sand bars, rocks, shoals, reefs and other hazardous marine features relies on accurate and up-to-date water depth measurements (Jupp, 1988). Some nearshore activities such as recreation, fishing, and aquaculture, as well as offshore engineering works such as cable and pipeline laying, dredging, oil drilling, and beach nourishment, require knowledge of bathymetry (Su et al., 2008).

1.2 Objective

In this study, bathymetric lidar data and airborne high resolution imagery are evaluated for their capability to map submerged structures in a shallow water coastal estuarine environment along the Texas Gulf Coast. 3D and 2D methods for segmentation and detection of submerged pipelines within bathymetric lidar data and imagery are examined. Image enhancement methods

including glint correction and edge detection are applied to improve mapping benthic structures using the aerial imagery and results compared with the lidar data. In addition, Structure from Motion (SfM) photogrammetry using a UAS equipped with a consumer grade NIR digital camera is evaluated to assess the effectiveness of the technique for mapping in shallow water.

For the bathymetric lidar data, three spatial interpolation methods including Delaunay Triangulated Irregular Network (TIN), Inverse Distance Weighted averaging (IDW), and B-spline multilevel interpolation are examined to create bathymetric digital elevation models (DEMs) from classified point cloud data. The effect of interpolation on submerged pipeline delineation utilizing the DEMs is then assessed. For the acquired aerial imagery, three different algorithms including Sobel, Prewitt, and Canny are examined in edge detection image processing to illustrate the potential pipelines and their performance quantified. Furthermore, the impact of glint correction algorithms for enhancing the visualization of submerged structures in shallow water is investigated. Finally, several image preconditioning methods for enhancing UAS-SfM results over shallow water are examined, including non-glint vs. glint corrected imagery and single band vs. multiband feature correspondence, with the goal of determining the effectiveness of this approach for bathymetric imaging of submerged structures in the coastal zone.

1.3 Overview

This study is outlined as follows. In the next section, the background and literature review of bathymetric lidar technology, benthic mapping with aerial digital imaging, sun glint correction methods, edge detection approaches, and UAS-SfM photogrammetry are described. Next, the study area and data set are explained followed by a chapter explaining the methods and algorithms that are applied to this case study. Next, a discussion on the results and relevant findings is presented. In the last part, the conclusion and future work are explained.

CHAPTER 2

BACK GROUND AND LITERATURE REVIEW

2.1 Airborne bathymetric lidar

Light detection and ranging (lidar), is an active remote sensing technique versus passive remote sensing, like imagery (Nayegandhi et al., 2009). The development of lidar technology commenced in the 1970s, with early systems built in the USA and Canada (Ackermann et al., 1999). Bathymetric lidar systems have been developed to measure water depth and can also measure terrain heights. However, it has typically lower accuracy and spatial resolution compared to the topographic equivalent. Another limitation of all bathymetric lidar systems is their inability to measure depths where the water is not clear. Lidar systems consist of a high frequency laser, beam steering mechanism (e.g. scanning mirror), mobile platform, and an integrated navigation system consisting of a GPS (Global Positioning System) receiver and an IMU (Inertial Measurement Unit). The system is able to record the time difference between the emission of the laser pulse and the reception of the return signal (the round-trip time of flight). The distance between the laser source and the object (reflecting surface) is computed by knowing the speed of transmission of the laser pulse propagates at the speed of light and the time of flight. The 3D position and orientation of the laser transmitter at each laser pulse are determined by the GPS and IMU respectively (Quadros et al., 2008). Topographic lidar's typically employ a near-infra-red laser which is not able to penetrate water (Leatherman, 2003). In contrast, bathymetric lidar systems generally operate with a blue-green laser (e.g. 532 nm), and NIR laser. The green channel is ideal for penetrating water and therefore measuring the water depth. A green pulse at 532 nm is suited for lidar bathymetry from the air. The NIR signal is absorbed by the water surface and is used to detect it. In addition, Guenther, et al.'s (1994) work shows that some lidar

systems record the red wavelength Raman signal (647 nm) which comes from interactions between the blue-green laser and water molecules, causing part of the energy to be backscattered during the change in wavelengths (as cited in Klemas, 2011).

Knowing the water surface is a requirement to segment returns from the green laser pulse below the water surface, and to compensate for refraction due to the slowing of light propagation within the air-water interface. The amount of refraction is proportional to the angle of incidence as described by Snell's law (Fig. 2.1; Fig. 2.2).

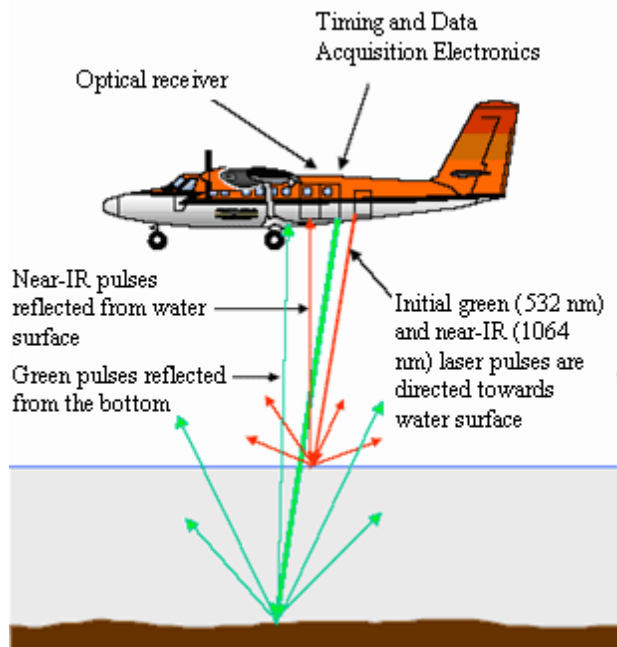


Figure 2. 1. Bathymetric lidar system (LaRocque and West, 1999)

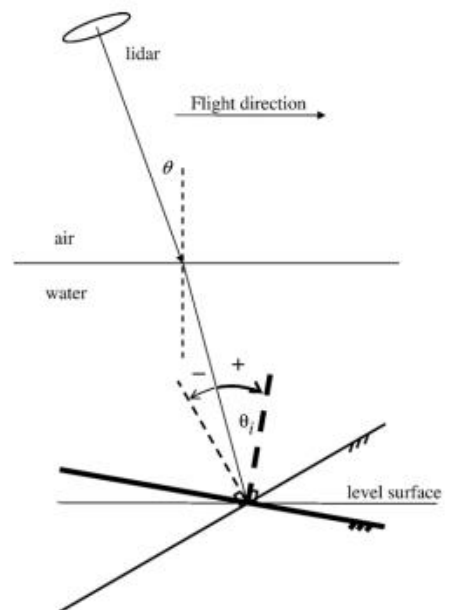


Figure 2. 2. Refraction through water; this figure shows the refraction of an incident light beam passing from air through water and reflecting from the sea bottom. The nadir angle is defined by θ (Wang & Philpot, 2007)

Three situations happen when the light pulse meets the sea floor: it undergoes absorption, scattering, and refraction. The combination of these effects limits the strength of the bottom return and therefore limits the maximum detectable depth. Turbidity and bottom type are the two most limiting factors for depth detection. In other words, bathymetric lidar for benthic detection is heavily limited by water turbidity and volume scattering from the water column, and therefore it is limited in its ability to map in deep or more turbid water (Fig. 2.3). It can vary considerably from just a few meters in very turbid water, to several tens of meters in clear water. According to Irish & Lillycrop (1999), lidar bathymetric sensor may collect data through depths equal to three times the site's Secchi (visible) depth (Irish & Lillycrop, 1999; Irish & White 1998; LaRocque & West, 1999; Tamari et al., 2011).

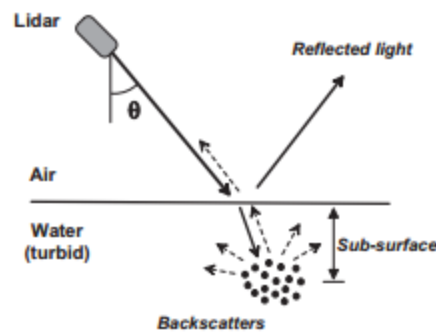


Figure 2.3. Backscattering in turbid water (Tamari et al., 2011)

The main purpose of airborne lidar data is to generate Digital Elevation Models (DEMs). A DEM is a numerical representation of topography, usually made up of equal-sized grid cells, each with a value of elevation. There are some interpolation algorithms to generate DEM out of lidar data. In what follows, multilevel B-spline Interpolation, 2D Delaunay Triangulated Irregular Network (TIN), and Inverse Distance Weighted (IDW) averaging are explained. Multilevel B-Spline was proposed by Lee et al. (1997). This algorithm makes use of a coarse-to-fine hierarchy of control lattices to generate a sequence of bicubic B-spline functions $f(k)$,

whose sum approaches the desired interpolation function. In the sequence, a function from a coarse lattice provides a rough approximation, which is further refined in accuracy by functions derived from finer lattices (Lee et al., 1997, Cichocinski & Basista, 2013).

Delaunay triangulation is one of the most important geometric structures in computational geometry. This algorithm has many practical applications including Geographic Information Science (GIS). Delaunay triangulation illustrates a unique triangulation of the points which are in the plane. This unique triangulation exhibits a large class of well-defined properties. An important property of the Delaunay triangulation is that edges correspond to empty circles. In fact, this property can be used as the definition of Delaunay triangulation (Lee and Lin 1986, Chew 1989).

IDW interpolation method assumes that each input point has a local influence that diminishes with distance. In other words, the closer point has more influence on predicting value. This method uses a linear-weighted combination set of sample points to estimate an unknown point value. The weights are defined as the inverse proportion to a power of distances between the data location and the particular point to be estimated. The limitation of IDW is that it cannot estimate outside of the minimum and maximum range of sample point values because of its weighted average method. In contrast, spline method can estimate values that are below and above the minimum and maximum respectively. In other words, it can predict the ridges and valleys where they are not in the sample data. Therefore, the result is more smooth compare to other methods (Liu 2008).

Doneus et al. (2013) used airborne bathymetric lidar for the documenting of submerged archaeological structures at the small island of Sveti Petar in northern Croatia. The results demonstrate the potential of this method to map submerged archaeological structures in shallow

water at a maximum depth of 8.2 m over large areas in 3D. Doneus et al. (2013) shared a variety of technical information on methodology that included the point density of data which was 10-50 points per square meter in their case (very dense for bathymetric lidar and typical). Least squares adjustment was used to minimize the error between stripes stemming from a model of the water surface. Digital model of the underwater topography with a grid spacing of 25 cm could be derived. In most cases the walls are 1 m broad and show height differences to the surrounding sea floor between 5 cm and 15 cm. The floors are often raised by 15-20 cm (Doneus et al., 2013). This shows that using lidar data in order to detect submerged structures is possible via creating a DEM from point clouds. However, there are some limitations to airborne bathymetric lidar. The most significant limitation is water clarity, which limits the maximum depth penetration. This requires that the incoming laser pulse be strong and free from water column absorption and excessive scattering before reaching the underlying surface. The authors contended that the second limitation for airborne bathymetric lidar was that detecting small objects that were the size of 1-meter cube or less was difficult or impossible based on their lidar system survey characteristics (most notably point density). The detection probability for small objects could be increased by greatly increasing the survey density.

Wedding et al. (2008) used bathymetric lidar to define near shore benthic habitat complexity in Hawaii. The authors assessed the potential application of lidar data for examining the relationship between habitat complexity and Hawaiian reef fish assemblage characteristics. Lidar-derived rugosity (4 m grid size) was found to be highly correlated within situ rugosity and was concluded to be a viable method for measuring rugosity in analogous coral reef environments (Wedding et al., 2008).

Kumpumaki et al. (2015) used bathymetric lidar waveform analysis to classify benthic cover type in Olkiluodonvesi Bay, Finland. In this method the waveform of the bathymetric lidar return pulse was modeled as a sum of three functions based on Gaussian pulse. By defining two variables (features and various conditions), a regression analysis was conducted to eliminate the effect of the condition variables on the features. In the last step, features were mapped onto a cell lattice using a self-organizing map. Seabed substrate map based on sonar measurements was used to evaluate the result, as well as delineation of photic zones in the study area (Kumpumaki et al., 2015).

2.2 Aerial Imaging for Benthic Mapping

Image segmentation is one of the most fundamental and difficult problems in image analysis. Image segmentation is an important part in image processing. In other words, image segmentation is a major step for automated object recognition systems. There are many methods and algorithms to delineate submerged features using high resolution imagery. Padmavathi et al. (2010) investigated image segmentation to detect submerged features. In many cases, image processing is affected by illumination conditions, random noise and environmental disturbances due to atmospheric pressure or temperature fluctuation. Authors defined the different methods of image segmentation algorithms for underwater images in their study including edge based image segmentation method, adaptive thresholding method, watershed method, region growing by active contour method, quadtree method, and fuzzy c-means clustering method. In edge based image segmentation method, the edge detector is used to process the two parameter images and then the derived edges are added to derive the final edge detection results. Thresholding is called adaptive thresholding when different thresholds are used for other regions in the image (Padmavathi et al., 2010; Shafaita et al., 2008; Zhang & Liu, 2006).

2.2.1 Edge Detection

The edge of an image is the most basic feature of the image. It contains a wealth of internal information of the image. Generally, edges in an image can be divided into two categories: intensity edges like a pipe reflectance and wall edges or texture edges like boundaries of texture regions. In a gray level image, an edge may be defined as a sharp change in intensity. Therefore, edge detection is one of the key research works in image processing. Edge detection is the process that detects the presence and locations of these intensity transitions. The edge representation of an image extremely reduces the amount of data to be processed, because it retains important information about the shapes of objects in the scene. Filter operators (e.g. high frequency band pass filter) are used in the process of locating the object edges, which are discontinuous. These discontinuities bring changes in pixels intensities, which define the boundaries of the objects. There are two steps in the edge detection process. First, edge enhancement operator is used to highlight the local edge of the image. Then the threshold and edge strength are set to extract the edge point set. The main two operators in image processing are gradient and Gaussian operators. The gradient method detects the edges by looking for the maximum and minimum in the first derivative of the image (e.g. the Sobel and Prewitt methods) while the Gaussian method searches for the zero crossings in the second derivative of the image to find edges (e.g. the Canny method). Gradient operator is a classical one and simplicity is one of the primary advantages of it. The second advantage of the classical operator is detecting edges and their orientations. In this cross operator, the detection of edges and their orientations is said to be simple due to the approximation of the gradient magnitude. The disadvantage of this operator is sensitivity to noise, in the detection of the edges and their orientations. The increase

in the noise to the image will eventually degrade the magnitude of the edges (Basu, 2002; Tan et al., 1989; Shrivakshan & Chandrasekar, 2012).

Sobel operator is a kind of orthogonal gradient method which is pixel-level edge detection arithmetic. It can detect edges by calculating partial derivatives in 3x3 neighbors. This method utilizes two masks S_x and S_y , to do convolution on the image to detect the edges based on the abrupt change of the gray level and then obtain the edge intensities E_x and E_y in the vertical and horizontal directions, respectively. In other words, for a continuous function $f_{(x,y)}$, when in the position (x, y) , its gradient can be expressed as a vector (the two components are two first derivatives which are along the X and Y direction respectively):

$$\nabla f(x, y) = [G_x \ G_y]^r = \left[\frac{\partial f}{\partial x} \ \frac{\partial f}{\partial y} \right] \quad (2.1)$$

The magnitude and direction angle of the vector are:

$$mag(\nabla f) = |\nabla f_{(2)}| = [G_x^2 \ G_y^2]^{1/2} \quad (2.2)$$

$$\emptyset(x, y) = \tan^{-1} \left(\frac{G_x}{G_y} \right) \quad (2.3)$$

The partial derivatives of the formulas above need to be calculated for each pixel location. In practice, small area template convolution is used to do approximation. G_x and G_y each need a template, so there must be two templates combined into a gradient operator. The two 3x3 templates are illustrated in Figure 2.4 used by the Sobel method. Every point in the image should use these two kernels to do convolution. One of the two kernels has a maximum response to the vertical edge, and the other has a maximum response to the level edge. The maximum

value of the two convolutions is used as the output bit of the point, and the result is an image of edge amplitude.

-1	-2	-1
0	0	0
1	2	1

-1	0	-1
-2	0	2
-1	0	1

a) Convolution template S_x

b) Convolution template S_y

Figure 2.4. Two convolution masks in Sobel method (Kang and Wang 2007)

The reason of using Sobel operator is that it is insensitive to noise and it has relatively small masks compared to other operators. Unfortunately, the edge line detected by Sobel method is usually thicker than the actual edge (Gao et al., 2010, Ying-Dong et al., 2005).

Prewitt method is another operator in gradient category. In this method, the edges are detected by convolving horizontal and vertical masks G_x and G_y respectively (Formula 2.4, Fig. 2.5), through the image. The masks are orthogonal to each other and used to measure the difference among the adjacent pixels gray level in horizontal and vertical direction. The detected edges are displayed by combining the horizontal and vertical edges (Seif et al., 2010).

$$|G| = |G_x| + |G_y| \tag{2.4}$$

$G_x =$	<table border="1" style="display: inline-table;"> <tr><td>-1</td><td>0</td><td>1</td></tr> <tr><td>-1</td><td>0</td><td>1</td></tr> <tr><td>-1</td><td>0</td><td>1</td></tr> </table>	-1	0	1	-1	0	1	-1	0	1
-1	0	1								
-1	0	1								
-1	0	1								

$G_y =$	<table border="1" style="display: inline-table;"> <tr><td>-1</td><td>-1</td><td>-1</td></tr> <tr><td>0</td><td>0</td><td>0</td></tr> <tr><td>1</td><td>1</td><td>1</td></tr> </table>	-1	-1	-1	0	0	0	1	1	1
-1	-1	-1								
0	0	0								
1	1	1								

Figure 2.5. The horizontal and vertical Prewitt edge detection masks (Seif et al., 2010)

The Canny edge detection algorithm is considered a standard method which is used by many researchers. The Canny method was proposed by Canny (1986). This method is categorized as Gaussian operators. Canny edge detection uses linear filtering with a Gaussian kernel to smooth noise and then computes the edge strength and direction for each pixel in the smoothed image. These processes are done by differentiating the image in two orthogonal directions and computing the gradient magnitude as the root sum of squares of the derivatives. The gradient direction is computed using the arctangent of the ratio of the derivatives. Candidate edge pixels are identified as the pixels that survive a thinning process called non-maximal suppression. In this process, the edge strength of each candidate edge pixel is set to zero if its edge strength is not larger than the edge strength of the two adjacent pixels in the gradient direction. In the next step, thresholding is done on the thinned edge magnitude image using hysteresis. In hysteresis, two edge strength thresholds are used. All candidate edge pixels below the lower threshold are labeled as non-edges and all pixels above the low threshold that can be connected to any pixel above the high threshold through a chain of edge pixels are labeled as edge pixels. The Canny edge detector allows the user to specify two parameters. The first is sigma, the standard deviation of the Gaussian filter specified in pixels. The size of the Gaussian filter is controlled by the greater value and the larger size. The larger size produces more noise, which is necessary for noisy images, as well as detecting larger edges (Fig. 2.6).

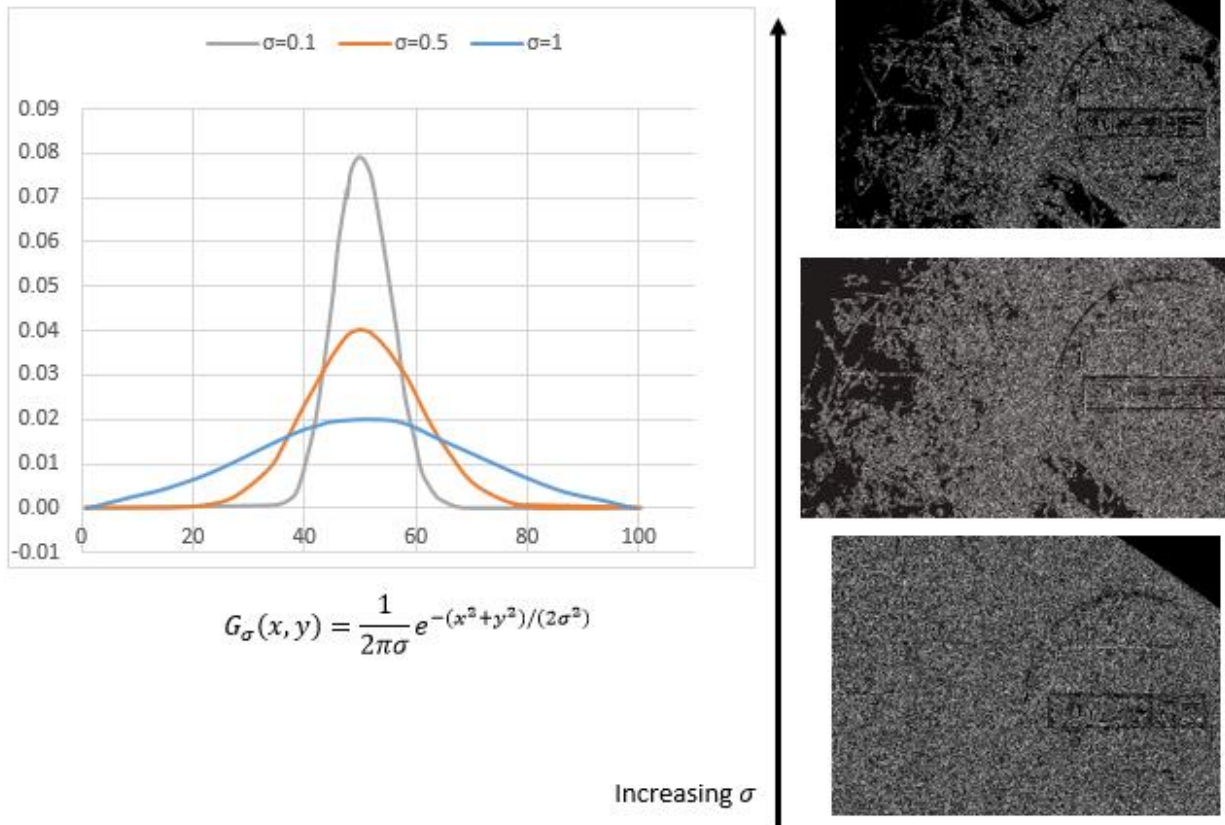


Figure 2.6. Effect of sigma on image smoothing; the more sigma increases the more detail lost.

The second parameter is a gray-level threshold (low and high). Thresholding is an important technique in image segmentation applications. The basic idea of thresholding is to select an optimal gray-level threshold value for separating objects of interest in an image from the background, based on their gray-level distribution.

$$g(x, y) = 1 \text{ if } f(x, y) \geq T \tag{2.5}$$

$$= 0 \text{ otherwise}$$

Thresholding operation is defined as:

$$T = M [x, y, p(x, y), f(x, y)] \tag{2.6}$$

In this equation, T stands for the threshold; $f(x, y)$ is the gray value of point (x, y) and $p(x, y)$ denotes some local property of the point such as the average gray value of the

neighborhood centered on point (x, y) . Thresholding is divided into thresholding methods. When T depends only on $f(x, y)$ (in other words, only on gray-level values) and the value of T solely relates to the character of pixels, this thresholding technique is called global thresholding. If threshold T depends on $f(x, y)$ and $p(x, y)$, this thresholding is called local thresholding. This method divides an original image into several sub regions, and chooses various thresholds T for each sub region reasonably. The high threshold is a fraction of the gradient magnitude and the low threshold is a fraction of the calculated high threshold value. The thresholds are set according to the amount of noise in the image, which is determined by a noise estimation procedure. The performance of the Canny algorithm relies mainly on changing these parameters. The user can modify the algorithm by changing these parameters to suit the different environments (Canny 1986; Vala and Baxi 2013).

In fact, Canny modifies Sobel method and determines the direction angle of the edge point by analyzing vertical and horizontal edge intensities of the pixel, and then uses non-maxima suppression to extract the edge points. Canny method uses the same edge intensity as that of Sobel method to define the edge angle as $\tan^{-1}\left(\frac{E_x}{E_y}\right)$. Four possible edge directions in a mask, shown in Figure 2.7, are used to approximate the edge angle. The Canny method can detect much thinner edges than the Sobel method (Kang and Wang 2007).

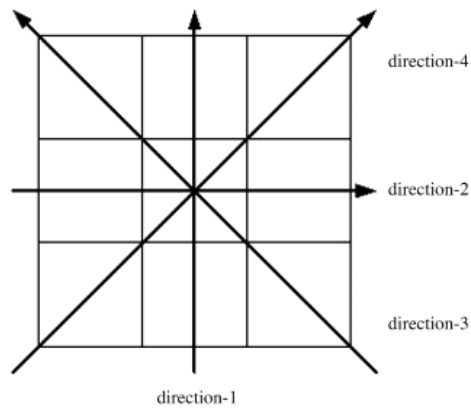


Figure 2.7. Four directions of edge (Kang and Wang 2007)

Shrivakshan and Chandrasekar (2012) worked on several gradient and Gaussian operators on picture of sharks to detect the edges. They examined different types of algorithms including Sobel, Prewitt, and Canny. The authors concluded that gradient-based methods have major drawbacks in sensitivity to noise. In addition, the performance of the Canny algorithm relies on the changing parameters which are standard deviation for the Gaussian filter, and its threshold values. Their evaluation showed that under the noisy conditions, Canny, Sobel, Prewitt, exhibited better performance, respectively (Shrivakshan, & Chandrasekar 2012).

Ying-Dong et al. (2005) enhanced the Sobel algorithm by combining Sobel operator and Zernike moments operator with subpixel accuracy. For the Zernike moments operator, two 7x7 masks were deduced and a new criterion was used for edge recognition. They claimed that detection precision of the proposed technique was close to Zernike moments operator, while the run time of image processing was greatly reduced compared to Zernike moments operator, based on their results (Ying-Dong et al., 2005).

There are many methods for assessing the performance of edge detection. Theoretical evaluation is one of the methods for this purpose, which is done by applying a mathematical analysis without the algorithm(s) ever being applied to an image. However, the input to the

algorithm is mathematically characterized and the performance is determined. The other method is evaluating using ground truth. In this method, the edges are evaluated in detection and noising, localization, thinness, and edge continuity (Heath et al., 1997, Strickland and Chang, 1990).

2.2.2 Sun glint removal

Multispectral airborne sensors have the potential to provide detailed spectral information with high spatial resolution. Such information would provide great benefits for mapping submerged benthic structures in coastal areas where the spatial incongruity is high (Vahtmäe & Kutser, 2007). However, the mapping of submerged structures can be hindered by water surface. When sky is clear and the water surface is not calm, specular reflection of the incident radiation blocks the benthic component of the remotely sensed data with areas of bright white, which is called sun glint. The reflected radiance does not contain any information about the water constituents and benthic features. There are some conditions that are likely to affect the amount of the glint including: clear skies, shallow waters, and images being collected at a high spatial resolution (Hedley et al., 2005).

Hence, to achieve this goal a variety of methodologies have been developed to date towards correcting glint from remotely sensed data, i.e. hybrid airborne sensor data (Lyzenga, 1985), satellite images of high resolution (Hochberg et al., 2003; Hedley et al., 2005), and multispectral or hyperspectral imagery data (Goodman et al., 2008).

Eugenio et al., (2015) improved an algorithm for sun glint removal (Kay et al., 2009) based on combined physical and image processing techniques. After the glint was removed, subsurface features popped up and the bathymetry algorithm could be successfully applied. Then, they used the corrected multispectral data to implement an efficient multichannel physics-based algorithm. They stated that atmospheric correction and deglinting method should be

applied to imagery before developing the bathymetric and benthic map in order to increase the accuracy of the final products.

Kay et al. (2009) provided a thorough review of current glint correction techniques. Existing methods and algorithms can be divided into two categories, which are shallow water and open ocean. The imagery data for open ocean applications have spatial resolution on the scale of 100–1000 m. In these methods, statistical models of the sea surface are used to conduct the probability that the sea surface will be orientated to cause glint, depending on the sun and sensor position, wind speed and direction. The important note about these methods is that they can only correct moderate glint, so large errors remain in the brightest glint areas. Methods of second category employ imagery data of high spatial resolution (less than 10m) acquired over shallow coastal environments. In theory, almost the entire incident near-infrared and middle-infrared wavelengths of light is absorbed by the water column with negligible scattering (Fig. 2.8). The main assumption in this case is that the water leaving radiance in the near-infrared (NIR) should approach zero; hence, any NIR signal remaining after atmospheric correction must be due to sun glint. The estimated glint value and the pixel values of visible bands are then used to form the function for glint correction. Of course sediment in the water, subaqueous vegetation near the surface and other objects can still result in NIR reflection over water. In other words, this assumption is not valid when the water has turbidity or where vegetation reaches the surface (Kay et al. 2009).

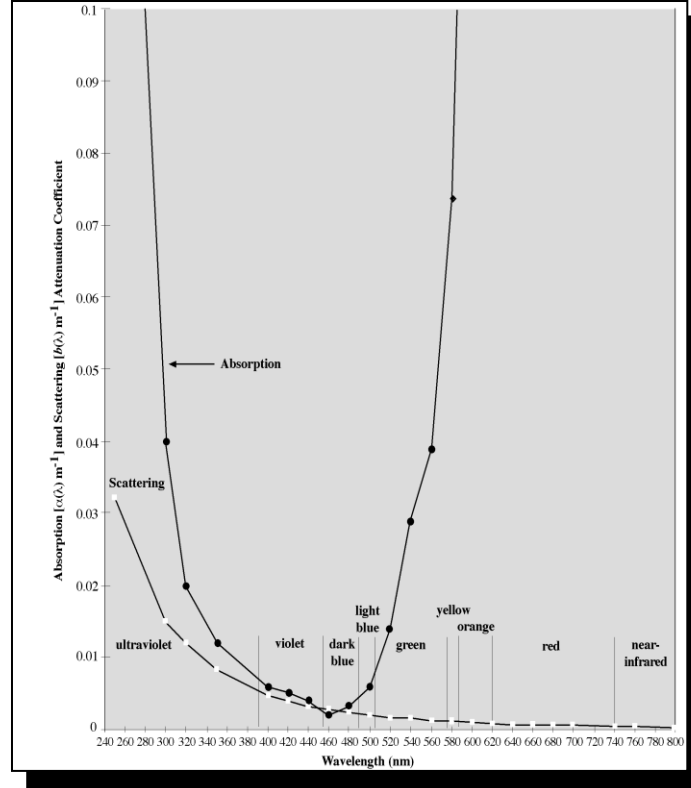


Figure. 2.8 Absorption in pure water (Jensen, 2000)

The Lyzenga algorithm describes glint correction from multispectral images depicting shallow waters (Lyzenga et al., 2006). According to his approach, sun glint is estimated by employing the covariance of the visible band (red, green, and blue) (Formula 2.7) that was used for depth processing and the near-infrared band. The high absorption of water at NIR band radiation should result in pixel brightness value close to zero and higher pixel values should imply atmospheric haze or glint effect (Doxani et al., 2013).

$$Cov(i, j) = \frac{1}{N} \sum_{n=1}^N L_{in} L_{jn} - \frac{1}{N} \sum_{n=1}^N L_{in} \frac{1}{N} \sum_{n=1}^N L_{jn} \quad (2.7)$$

$$L_i(VIS)' = L_i(VIS) - r_{ij} [L_j(NIR) - mean(L_j(NIR))] \quad r_{ij} = \frac{Cov(i, j)}{Var(j)} \quad (2.8)$$

Here $L_i(VIS)'$ = the corrected pixel value, $L_i(VIS)$ = the initial pixel value, and $mean L_j(NIR)$ is the mean NIR radiance in the region of interest.

Hochberg et al. (2003) proposed a simple and innovative method employing a physical atmospheric model for glint removal in shallow waters. In Hochberg et al.'s (2003) method the sun glint component of the remotely sensed signal is removed from visible wavelength spectral bands by utilization of information from a spectral band in near-infrared (NIR, 700–910 nm). The method is applicable to imagery from sensors that include an NIR band (e.g. satellites such as Ikonos or Landsat) or suitably configured multispectral and hyperspectral imagery (e.g. from airborne sensors such as CASI, Compact Airborne Spectrographic Imager). Image pixels are adjusted to remove the glint component of the recorded signal, thereby leaving only the component derived from benthic reflectance and radiative transfer processes within the water column (Hedley et al., 2005). There are two significant notes in this method that should be considered. The initial consideration describes that the radiance is highly absorbed by water at NIR band and so the pixel brightness value should tend to zero. The second consideration is that the refractive index is independent of wavelength. Therefore, the brightness value of glint pixels $f_g(x, y)$ is equal for visible and infrared bands. The deglinted visible bands were resulted by subtracting the quantity $f_g(x, y)$ from the glinted pixel values (Doxani et al., 2013). The weakness in the method is that in order to establish the linear relationship between the NIR brightness and sun glint in the visible wavelengths, only two pixels are used. Hedley et al. (2005) suggested that these should be the 'brightest and darkest' NIR pixels found across the whole image set, so this change makes this methodology more simplified (Hedley et al., 2005).

Hedley et al. (2005) refined the Hochberg et al. (2003) method and introduced a simplified and strong methodology for glint removal. The new suggestion was the use of one or more samples of image pixels rather than only two pixels, i.e. the brightest and the darkest one. The image processing for glint correction involves a linear regression analysis between the

sample pixels of every visible band (y-axis) and the corresponding pixels of NIR band (x-axis) (Fig. 9).

The image pixels are corrected according to the following equation:

$$L_i(VIS)' = L_i(VIS) - b_i [L(NIR) - L_{min}(NIR)] \quad (2.9)$$

where $L_i(VIS)'$ = the corrected pixel value, $L_i(VIS)$ = the initial pixel value, b_i = the regression line slope, $L(NIR)$ = the corresponding pixel value in NIR band and $L_{min}(NIR)$ = the minimum NIR value existing in the sample.

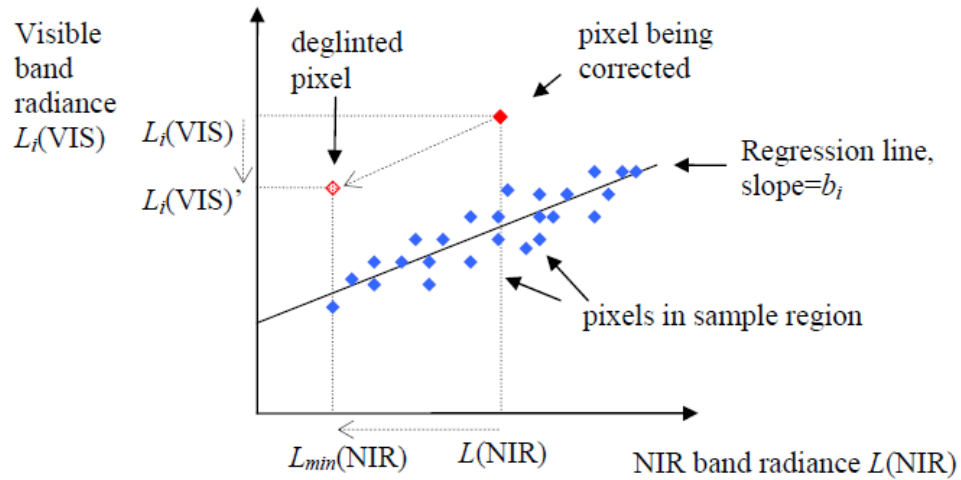


Figure 2.9. The regression analysis diagram illustrates relation between a visible and NIR brightness values. The pixels with no glint are homogeneous and close to the regression line. According to Hedley et al. (2005), the other pixels are corrected by estimating the slope of the regression and the minimum NIR brightness value of a sample (Kay et al., 2009).

Some important issues exist regarding this revised method. First, because this modification over Hochberg et al. (2003) method depends on user-based selection of a sample set of pixels, it is not necessary to mask out non-submerged or cloud pixels prior to deglinting. Second, sample pixels do not contain any non-submerged objects, but the regression will nevertheless mitigate the impact of isolated invalid pixels. However, non-submerged areas will

not contain valid data after deglinting because the algorithm is valid for only submerged pixels (Hedley et al., 2005).

2.3 UAS-Structure from Motion (SfM)

UAS-SfM photogrammetry is a technique that solves the camera pose (position and orientation) and scene geometry problem simultaneously and automatically, using a highly redundant bundle adjustment based on matching features in multiple overlapping images (Westoby et al., 2012). A bundle of rays that originates from an object point and passes through the projective center to the image points (Fig 2.10), forms the basic computational unit of aerial triangulation. Bundle adjustment means the simultaneous least squares adjustment of all bundles from all exposure stations, which implicitly includes the simultaneous recovery of the exterior orientation elements of all photographs and the positions of the object points.

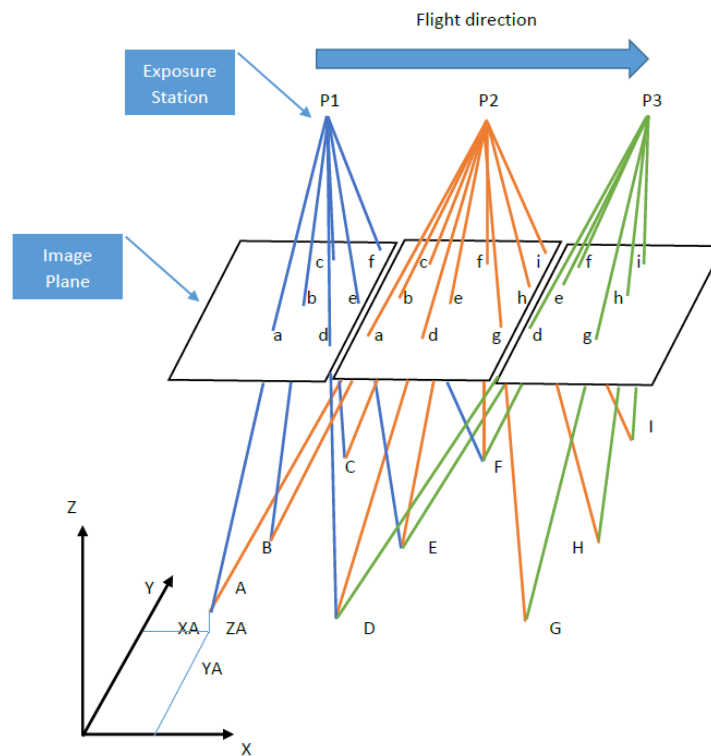


Figure 2.10. Bundle Block

UAS-SfM operates under the same basic principles as stereoscopic photogrammetry using collinearity equations (Wolf et al., 2000).

$$F_x = x_i - x_0 + c \frac{m_{11}(X_i - X_0) + m_{12}(Y_i - Y_0) + m_{13}(Z_i - Z_0)}{m_{31}(X_i - X_0) + m_{32}(Y_i - Y_0) + m_{33}(Z_i - Z_0)} = 0 \quad (2.10)$$

$$F_y = y_i - y_0 + c k_y \frac{m_{21}(X_i - X_0) + m_{22}(Y_i - Y_0) + m_{23}(Z_i - Z_0)}{m_{31}(X_i - X_0) + m_{32}(Y_i - Y_0) + m_{33}(Z_i - Z_0)} = 0 \quad (2.11)$$

where

$$M = \begin{bmatrix} m_{11} & m_{12} & m_{13} \\ m_{21} & m_{22} & m_{23} \\ m_{31} & m_{32} & m_{33} \end{bmatrix} = \quad (2.12)$$

$$\begin{bmatrix} \cos \varphi \cos k & \cos \omega \cos k + \sin \omega \sin \varphi \cos k & \sin \omega \sin k - \cos \omega \sin \varphi \cos k \\ -\cos \varphi \sin k & \cos \omega \cos k - \sin \omega \sin \varphi \sin k & \sin \omega \cos k + \cos \omega \sin \varphi \sin k \\ \sin \varphi & -\sin \omega \cos \varphi & \cos \omega \cos \varphi \end{bmatrix}$$

and

- (x_i, y_i) are the image coordinate,
- (x_0, y_0) are the principle point coordinate,
- c is the camera constant,
- m_{ij} is an element of rotation matrix,
- (X_i, Y_i, Z_i) are the feature point coordinates,
- (X_0, Y_0, Z_0) are the exposure station coordinates
- M is the rotation matrix,
- k_y is the scale factor for y axis

Camera pose and scene geometry are reconstructed simultaneously through the automatic identification of matching features in multiple images. Image matching is one of the important aspects in UAS-SfM photogrammetry. Scale Invariant Feature Transform (SIFT) algorithm is used for image matching that transforms image data into scale-invariant coordinates relative to local features and it is differ from those used in standard photogrammetry. These features are tracked from image to image, enabling initial estimates of camera positions and object coordinates that are then refined using non-linear least squares optimization. Unlike traditional

photogrammetry, the camera positions derived from SfM lack the scale and orientation provided by ground-control coordinates. Consequently, the 3-D point clouds are generated in a relative ‘image-space’ coordinate system, which must be aligned to a real world ‘object-space’ coordinate system (Westoby et al., 2012; Snavely et al., 2008; Lowe 2004). SfM photogrammetry works well with low-budget research and application in remote areas. SfM is a low cost photogrammetry method when coupled with unmanned aircraft systems (UAS) as an image acquisition platform (Everaerts 2008; Siebert & Teizer 2014).

SfM approach using UAS was examined to collect low-altitude aerial imagery in order to create a Digital Surface Model (DSM) of a beach dune system in Mariana di Ravenna (Italy) by Mancini et al. (2013). The authors mentioned that the vertical accuracy of the UAS- SfM approach was comparable with results obtained by terrestrial laser scanner (TLS) technology (Mancini et al., 2013). Woodget et al. (2014) used UAS-SfM photogrammetry method in order to produce a DEM of submerged fluvial topography for depths up to 0.70 meter in Coledale Beck (UK). The authors considered refraction correction in their calculation. Hence, the accuracy increased by applying this correction. The accuracy of results was compared with blue- green TLS approach that could penetrate water. Based on the authors’ statement, UAS-SfM technique has potential as a valuable tool for creating high resolution, high accuracy topographic datasets for assessment of fluvial environments at the mesoscale and a wide range of other geomorphological applications (Woodget et al., 2014).

Westoby et al. (2012) examined the accuracy of the SfM method for measuring cliff erosion. In terms of accuracy, the SfM results have acceptable output comparing with TLS results. The authors mentioned that the nature of the SfM method eliminates the requirement for manual identification of image control prior to processing, instead employing automatic camera

pose estimation algorithms to simultaneously resolve 3-D camera location and scene geometry; this is an extremely significant advantage of the technique over traditional digital photogrammetric methods (Westoby et al., 2012).

CHAPTER 3

STUDY AREA AND DATA SET

3.1 Study Area

The study area is located in the Shamrock Cove region of the Corpus Christi Bay system along the lower-central Texas Gulf Coast (Fig. 3.1). Corpus Christi Bay is a shallow embayment in the Texas Coastal Bend region with a flat bottom between 3 and 4 m deep over roughly 90% of the bay (Montagna and Ritter 2006; Simms et al., 2008). It is connected with the Gulf of Mexico through a narrow ship channel (15 m depth), which runs from east to west. Corpus Christi Bay is the nation's seventh largest port, with numerous petrochemical facilities (Islam et al., 2011). The importance of the study area is because of the heavy oil and gas exploration activities in the area resulting submerged structures including pipelines, which may influence the marine environment, shipping navigation, and recreational boating. Therefore, mapping submerged structures is the first step of any further study in this area.



Figure 3. 1. Study area (google & GLO website)

3.2 Data set

The data set contains three types of data: bathymetric lidar data, high resolution aerial imagery from piloted aircraft, and hyperspatial resolution imagery acquired by a UAS at low altitude.

The lidar data were acquired by the University of Texas Bureau of Economic Geology (BEG) on January 30th and February 5, 2015 using their Chiroptera airborne lidar system, which is developed and manufactured by Airborne Hydrography AB (AHAB) (Fig. 3.2). The system is capable of recording up to 4 returns per a transmitted laser pulse and enables simultaneous topographic and bathymetric scanning. The topographic lidar scanner was operated at a wavelength of 1 μm , a pulse rate as high as 400 kHz while the bathymetric lidar scanner was operated at a shorter wavelength (0.5 μm) and a lower pulse rate (36 kHz). The shorter wavelength allows the laser to penetrate water of reasonable clarity. Horizontal accuracy quoted by the BEG is +/- 5 meters to true ground at 95 percent confidence level. Vertical accuracy for flat bottom bathymetry is quoted to be 15 cm (BEG metadata). The system can operate to a maximum height of about 1500 m. The point density for topographic lidar and bathymetric lidar were approximately 7 point per square meter and 3 points per square meter respectively (Fig. 3.3). The coordinate system is to WGS84 UTM- 14N and uses NAVD88 as the vertical datum.



Figure 3.2. Leica AHAB Chiroptera II (<http://www.airbornehydro.com>)

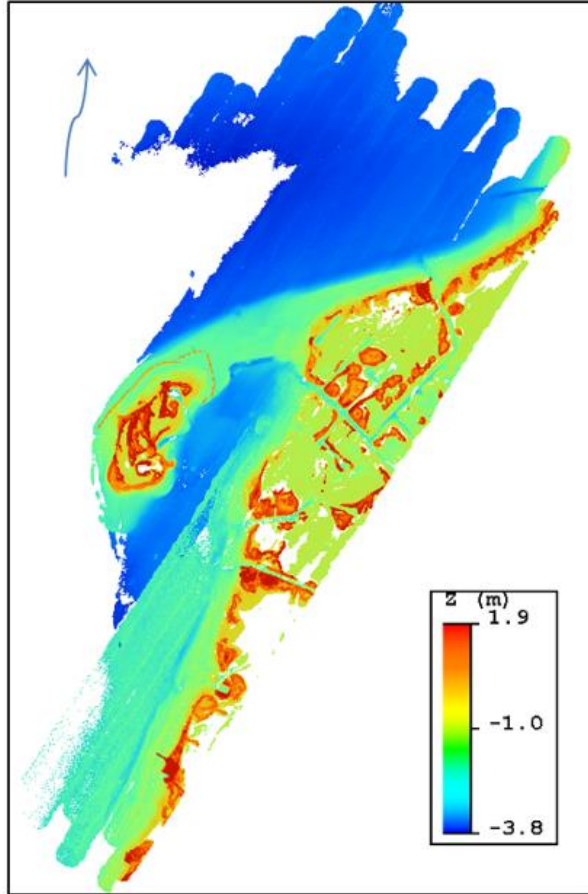


Figure 3.3. Lidar data (Point Cloud); color-coded by elevation (blue = lower elevation and red = higher elevation)

Two sets of aerial images were used for this study: the first set was recorded January 30th and February 5, 2015 using the Bureau of Economic Geology’s airborne system with 10 cm resolution. Images were recorded using the DigiCAM 50 megapixel natural color, or color infrared camera, that acquires frame images at a resolution of 8,176 by 6,132 pixels. Image sets were acquired from a maximum altitude of 1500 m above ground level. The horizontal accuracy was +/- 5 meters to true ground at 95 percent confidence. The images contain three bands based on the metadata. First band is near infrared, the second one is red, and the third band is green (Fig. 3.4).

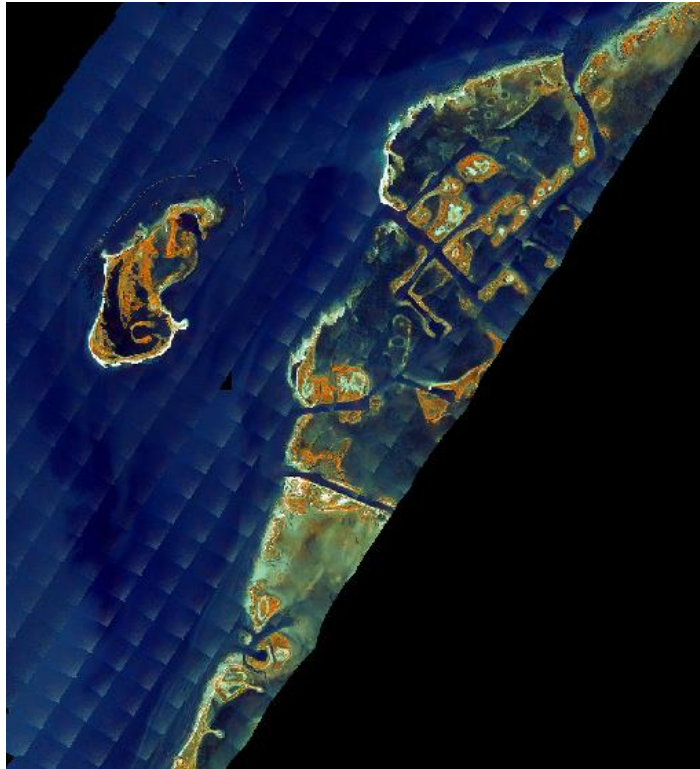


Figure 3.4. Aerial Imagery

The second set of imagery was recorded in April 2016 using a small professional-grade mapping UAS called the SenseFly eBee. The UAS has fully autonomous flight that can be programmed to acquire imagery at a desired flying height, percent image endlap, and percent image sidelap. The system can fly for a maximum time of approximately 50 minutes dependent on wind conditions. A 12-megapixel Canon Powershot S110 with a sensor size of 7.44 by 5.58 mm, capable of storing images in RAW and JPEG format, was modified to capture imagery in three bands of the electromagnetic spectrum: green (500-575 nm), red (575-650 nm), and near-infrared (800-900 nm) (Fig. 3.5).



Figure 3.5. Camera Canon Powershot S110

A shallow water region of Shamrock Cove equating to roughly 50 acres was flown with the UAS at a target altitude above ground of 310 ft. Image overlap (sidelap and endlap) was set at 80% resulting in a total of 189 high resolution TIFF images with an average pixel ground sample distance (GSD) of 3.45 cm ground sample distance. The data collection had two steps. First, the flight path for data collection using the eBee UAS flight planning software developed by MANTIS lab at Texas A&M University –Corpus Christi. Some parameters are needed to determine the amount of overlap of images which then determines the intervals of taking images, altitude or flight height (the lower flying height, the higher resolution imagery), the number of rows of flight and length of each row which depend on the flight area that the user needs to cover, and wind speed and direction. Therefore, the flight duration and distance were determined by software.

Table 3.1 shows these parameters and Figure 3.6 illustrates the flight path.

Table 3.1. Flight parameters

Flight Parameters		
1	Sidelap and endlap	80%
2	Altitude	310 ft.
3	Row	14
4	Wind speed	5.2 kts
5	Flight duration	16 min
6	Flight distance	6.7 mi



Figure 3.6. Flight path UAS-SfM (emotion- Pix4D)

The second part was field work (Fig 3.6). The flight time was set in the middle of the day when it is sunny. The images were taken by canon power shot S110-5.2 mounted on eBee UAV. The Figure 3.6 shows the starting and ending of taking photos. The 189 photos are downloaded into the computer. The raw images are JPEG and they are converted to geotiff. The third part is preprocessing/processing the images and producing the results in the lab. Figure 3.8 shows the camera pose in the initial processing and UAS-based SfM image.



Figure 3.7. Launching eBee By Dr. Starek (MANTIS lab)

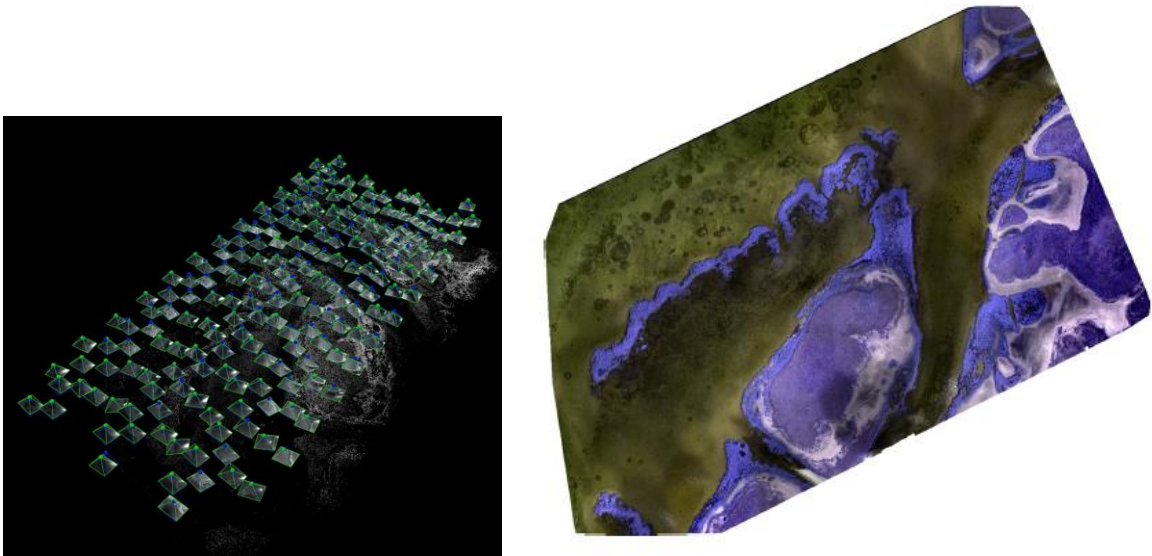


Figure 3.8. Structure from Motion image Left: Camera pose solving- Pix4D. Right: UAS-Based SfM image

CHAPTER 4

METHODOLOGY

This chapter contains three parts detailing the methods employed for implementing each research component. In the first part, bathymetric lidar data is investigated for its potential to detect submerged pipelines. As mentioned prior, three different spatial interpolation algorithms for deriving bathymetric DEMs are investigated (TIN, IDW, B-spline) and their effects on structure delineation results examined. In the second part, 3-band false-color infrared aerial imagery is examined for submerged pipeline detection. Three different methods of edge detection are employed for evaluating automated delineation of submerged structures, and the performance of glint correction on results is also examined. In the last part, imagery acquired from a small UAS equipped with a 3-band RGB camera modified for NIR capture is processed using SfM photogrammetry to assess the utility of the method for bathymetric mapping of submerged structures and benthic cover. Image preconditioning methods including sun glint correction and single band vs multiband image inputs are evaluated to determine their effect on SfM performance results over shallow water.

4.1 Bathymetric lidar

4.1.1 Lidar data classification

The first step consisted of classifying the 3D lidar point cloud. Classification is the process of distinguishing and assigning individual 3D points to object or terrain classes, so that in subsequent processing, surface and object modelling may be based only on the points from relevant surfaces. Filtering the point cloud into ground and non-ground returns is the core component of a lidar data processing (Chen, 2007). The last-return points from the lidar point cloud were filtered to remove non-ground points using a triangulated irregular network (TIN)

densification filter implemented with LAStools lidar post-processing software. The classification is important because generating a bare earth DEM from lidar and performing further analysis, such as deriving the elevation information for benthic features, is possible via classification. This data set contains LAS format bathymetric, topo, and turbid water point data from the Shamrock cove in Corpus Christi Bay, Texas.

Initial inspection of the bathymetric lidar survey revealed a data gap due to attenuation of the laser pulse in the water column (Fig. 4.1).

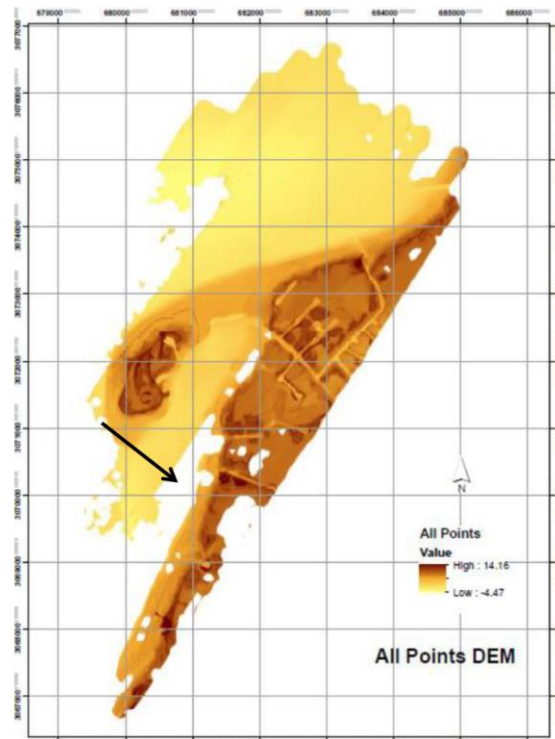


Figure 4.1. Topo-bathymetric DEM generated from the initial UT BEG survey product at Shamrock (all points here means topographic and bathymetric). Elevation in meters

In order to fill the gap area in the data set, the raw waveform returns were reprocessed by the UT BEG using a turbid water enhancement algorithm over that portion of the study site provided by the software of the lidar system manufacture. In order to have the proper data for processing, different parameters of filtering are examined to find the optimal match. The filter parameters

were tuned based on visual inspection and comparisons of DEM shaded relief products derived from different parameter settings. The most important filter parameter is called step size, which is governed by the size of objects and level of detail to retain. The data set is examined in 3, 5, 10, and 15 meters in different search cases including standard, fine, and hyper fine using LASTools ground point filter (Table 4.1).

Table 4.1. Turbid water data classification

No	STEP	SEARCHING CASE	# GROUND	# NON-GROUND
1	3m	Standard	1268270	671207
2	3m	Fine	1321125	618354
3	3m	Hyper-Fine	N/A	N/A
4	5m	Standard	1091551	847928
5	5m	Fine	1120655	818824
6	5m	Hyper-Fine	1140119	799360
7	10m	Standard	832133	1107346
8	10m	Fine	841215	1099264
9	10m	Hyper-Fine	849923	1089556
10	15m	Standard	654516	1284963
11	15m	Fine	658215	1281264
12	15m	Hyper-Fine	669681	1269798

All values in table 4.1 were examined and as a result hyper-fine research case with step size of 15 meters was determined “optimal” based on the filter tuning process. This step size allowed for the majority of above ground features to be removed while retaining the bare-earth surface area of the island (Fig. 4.2). The merged point clouds contain three different parts because of an existing gap in the initial data collection. In addition, the data was provided from UT-BEG as classified into seafloor points; however, the data is implemented by new classification to better refine the classification and improve results. The first part is bathymetric point cloud which is classified as class 7 (bottom/seafloor). The second part is a topographic point cloud that is classified as class 9 (ground). The third part is in the turbid water. This new

dataset is fused with the original dataset (Fig. 4.3) to try and derive a complete topo-bathymetric DEM for the purposes of mapping submerged structure.



Figure 4.2. Turbid water data filtering

As observed, the new dataset did provide returns from the data gap zone shown in Figure 4.2, but very few returns appear to reflect from the bottom. It is determined that the majority of these data points stemmed from the water column or near the surface. As such, the new dataset is not deemed useful for the purposes of pipeline detection in the data gap zone.

The three data sets were merged and duplicate points were removed from the new data set. Duplicate points might occur when two points have the same x, y coordinates and different z value or have the same x, y, and z coordinates in the data set. Entering duplicate points in the interpolation cause to create an incorrect DEM. Therefore, it is necessary to remove duplicate points before creating the DEM.

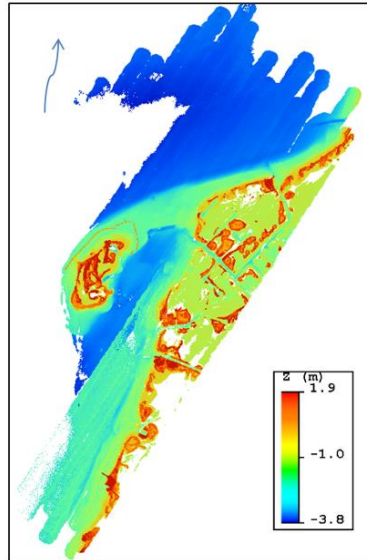


Figure 4.3. Bathymetric point cloud data. The merged new point cloud with the original data set color-coded by elevation (blue = lower elevation and red = higher elevation). The color of gap area shows the turbidity of water because it is not represented the real depth.

4.1.2 DEM

In this step, bathymetric DEMs from the classified ground point data were created. There are many spatial interpolation algorithms used to interpolate a digital surface such as a DEM. In this study, multilevel B-spline Interpolation, IDW, and 2D Delaunay TIN were applied to create the DEM. In each method there are multiple parameters that are needed to be set such as a weighting factor or the size of the radius that determines the number of weighed points that influence the interpolation; however, all methods require specifying a cell size for the output raster. Different cell sizes were examined including 0.50 m, 1 m, and 2 m. LASTools is used in order to create DEM with TIN interpolation. The parameters are only needed to set the step size (cell size) and item (elevation, slope, intensity, and rgb). Item was set to elevation in actual values and step size was set to 0.50 m, 1 m, and 2 m. ArcGIS was used in order to generate DEM with the IDW method. Several parameters are needed for this method, which are cell size, power, number of points, and maximum distance or search radius. The power is the exponent of inverse

distance that controls the significance of surrounding points on the interpolated value for considering the weight. A lower power results in more influence from distant points. ‘Number of point’ indicates how many points should be used to perform interpolation. Maximum distance specifies the distance, in map units, by which to limit the search for the nearest input sample points. In IDW method different parameter setting were examined (Table 4.2).

Table 4.2. IDW interpolation method parameter setting

No	Cell size	Power	Search radius
1	0.50	1	30
2	0.50	2	50
3	1	1	30
4	1	2	50
5	2	1	30
6	2	2	50

SAGA open source is used to generate DEM by multilevel B-spline method. In this method two parameters are set: cell size and the maximum level that determines the maximum size of the final B-spline matrix and increases exponential with each level. This parameter can be set between 1 and 14. Cell size is set to 0.50, 1, and 2 m. Maximum level is set to 10, 11, and 12. Shaded relief of the study area is created for each DEM which is extracted from those three interpolation methods for better visualization. A shaded relief (hillshade) is just a model for visualization derived from a DEM that is used to visualize the DEM by making it look 3D. The values of the shaded relief model no longer has any relevance to elevation and refer to shading values used by the software to view the surface to make it appear 3D. The parameters that should be mentioned in shaded relief are azimuth, altitude, and z factor. Table 4.3 shows the shaded relief parameters.

Table 4.3. Shaded relief parameter setting

No	AZ	Height	Exaggeration (Z factor)
1	315	30	1
2	315	30	2
3	315	45	1
4	315	45	2
5	315	60	1
6	315	60	2

4.1.3 Vertical accuracy assessment

There are many factors that affect the DEM accuracy. In other words, accuracy of DEM derived from lidar stems from lidar vertical/horizontal accuracy (Horizontal accuracy quoted by the BEG is +/- 5 and vertical accuracy for flat bottom bathymetry is quoted to be 15 cm), complexity of the terrain surface, sampling density of the terrain, classification or filtering error of the data, and finally interpolation method used to create the DEM. The overall performance of the interpolator is evaluated by the Root Mean Square Error (RMSE). In general, RMSE is calculated by observed value and predicted value (Equation 4.1):

$$RMSE = \sqrt{\left(\frac{1}{n} \sum_{i=1}^n (y_i - \bar{y}_i)\right)^2} \quad (4.1)$$

where y_i is predicted value, \bar{y}_i is observed value and n is number of points in the sample. Here, observed values are RTK GPS observations and predicted values are the values of the same points derived from DEM. In other words, DEM and GPS observations are used to assess the vertical accuracy of the different interpolation methods. Real Time Kinematic (RTK) GPS with virtual reference station (VRS) corrections applied was used to collect ground truth elevation data around the shoreline and shallow water at Shamrock Island near the date of the airborne lidar (on January 29, 2015). NAD83 State Plane Texas South (2011) Epoch 2010 (Meters) with

the elevations in NAVD88 using Geiod 12A are horizontal projection and vertical datum of GPS data respectively. The existing horizontal datum was reprojected to UTM Zone 14N - World Geodetic System of 1984 (WGS84) in meters. 879 land and shallow water RTK measurements were collected in depths of about one meter or less using Altus-APS-3, so vertical error near shore is conducted. Most of the GPS observations come from land (bare and vegetated) but still provide a good estimate of the accuracy of the derived DEMs for each spatial interpolation method (Fig. 4.4). The data were differentially corrected using broadcast Virtual Reference Station (VRS) corrections providing an estimated horizontal and vertical accuracy of less than 2 cm and less than 4 cm respectively.

4.1.4 DEMs assessment for delineating the pipelines

Different DEMs were created based on three interpolation methods and different parameter settings including cell size. Ground truth is the General Land Office (GLO) shapefile of the existing pipelines which is overlaid over the DEMs to assess the efficiency of the generated DEMs. The results are compared to each other in terms of finding pipelines in the generated DEMs.



Figure 4.4. RTK GPS transects collected at Shamrock Island using Altus-APS-3 by MANTIS lab crew

4.2 Aerial digital imagery

In this section, two sun glint correction algorithms are applied to the images since the acquired imagery is exposed to varying degrees of sun glint that can occlude visibility below the water surface. Then, edge detection image processing is applied to the imagery in order to detect linear features including submerged pipelines. Three different algorithms are examined including Sobel, Prewitt, and Canny. The chosen method is run over original and glint removal images and the results are compared to non-glint corrected imagery for pipeline delineation.

4.2.1 Sun glint correction

In fact, the principle of the all glint correction methods is to estimate the glint contribution to the radiance meeting the sensor, and then subtract it from the received signal. As

it was explained in the literature review, there are two main categories for sun glint removal. The first category deals with resolutions of the scale of 100-1000 m which is used for Open Ocean and deep water imagery. The second category is used for coastal and shallow water images with a pixel size less than 10 m. These methods use the NIR to indicate the amount of glint in the received signal. (Kay et al., 2009). Based on the location of the study area which is in shallow water, the method that will be used in this study fell in the second category.

4.2.1.1 Hedley et al. (2005)

Hedley et al. (2005) is one of the regression-based methods and deals with NIR. Therefore, this method is one of the best choices for conducting sun glint on this data set. In what follows, there is an explanation of how this method works. The imagery consists of three bands which are NIR, red, and green. Each image is split based on its components. The regression slope is calculated for each image, using the least squares regression slope to give the relationship between the visible (green and red) and NIR bands. In other words, the relationship between green band and NIR is established. This same process also occurs for red band and NIR. The corrected pixel value is conducted by using Formula (4.2):

$$L_i(VIS)' = L_i(VIS) - b_i [L(NIR) - L_{min}(NIR)] \quad (4.2)$$

where $L_i(VIS)'$ is the corrected pixel value, $L_i(VIS)$ is the initial pixel value, b_i is the regression line slope, $L(NIR)$ is the corresponding pixel value in NIR band and $L_{min}(NIR)$ is the minimum NIR value existing in the sample.

The corrected bands (green and red) are combined again at the end of processing. The output of this process is a deglint image. Figure 4.5 illustrates the processing steps in the workflow.

4.2.1.2 Lyzenga et al. (2006)

Lyzenga et al. (2006) is the other algorithm in the second category and is used to conduct sun glint. This method uses the covariance between each visible band (green and red) and the NIR instead of the regression used in the Hedley et al. (2005) method. In addition, this algorithm uses the mean NIR in the region of interest instead of minimum NIR. The sample images are conducted in this method to compare with the previous method. Figure 4.6 shows the process of the Lyzenga et al. (2006) method.

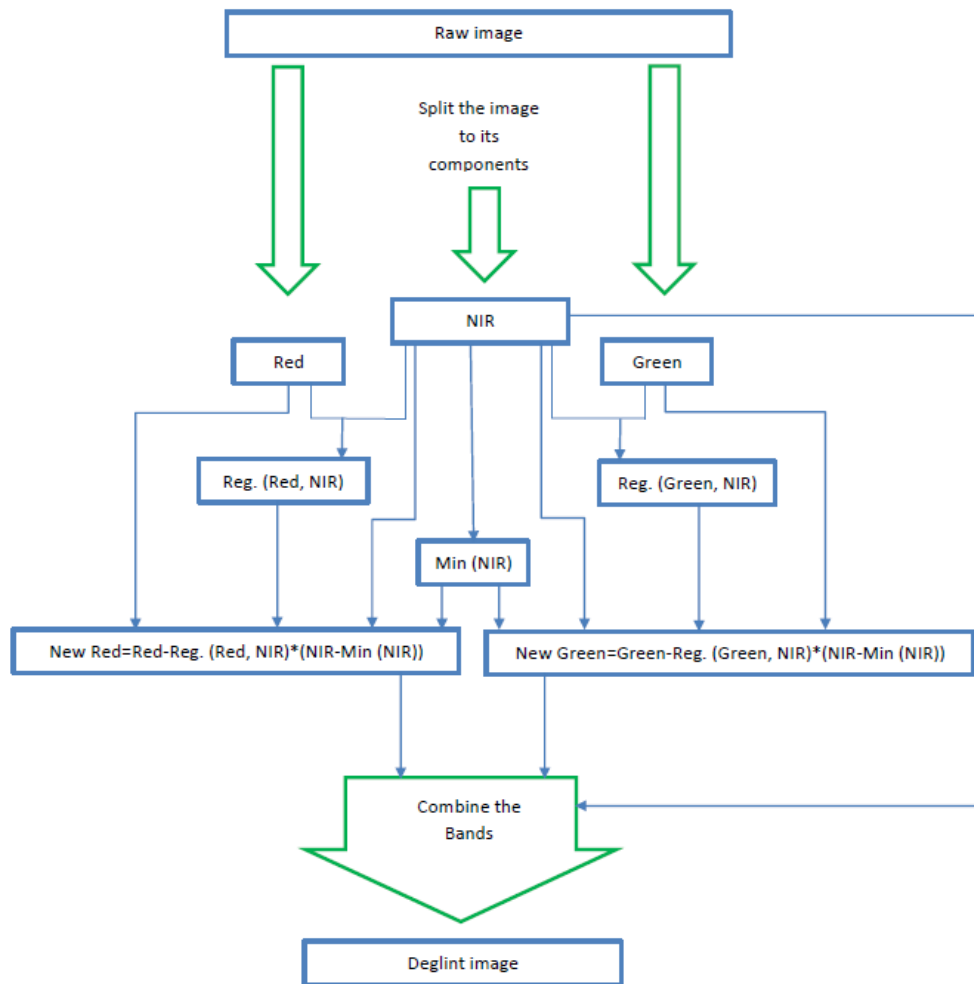


Figure 4.5. Flowchart of Hedley et al. (2005) algorithm for glint removal

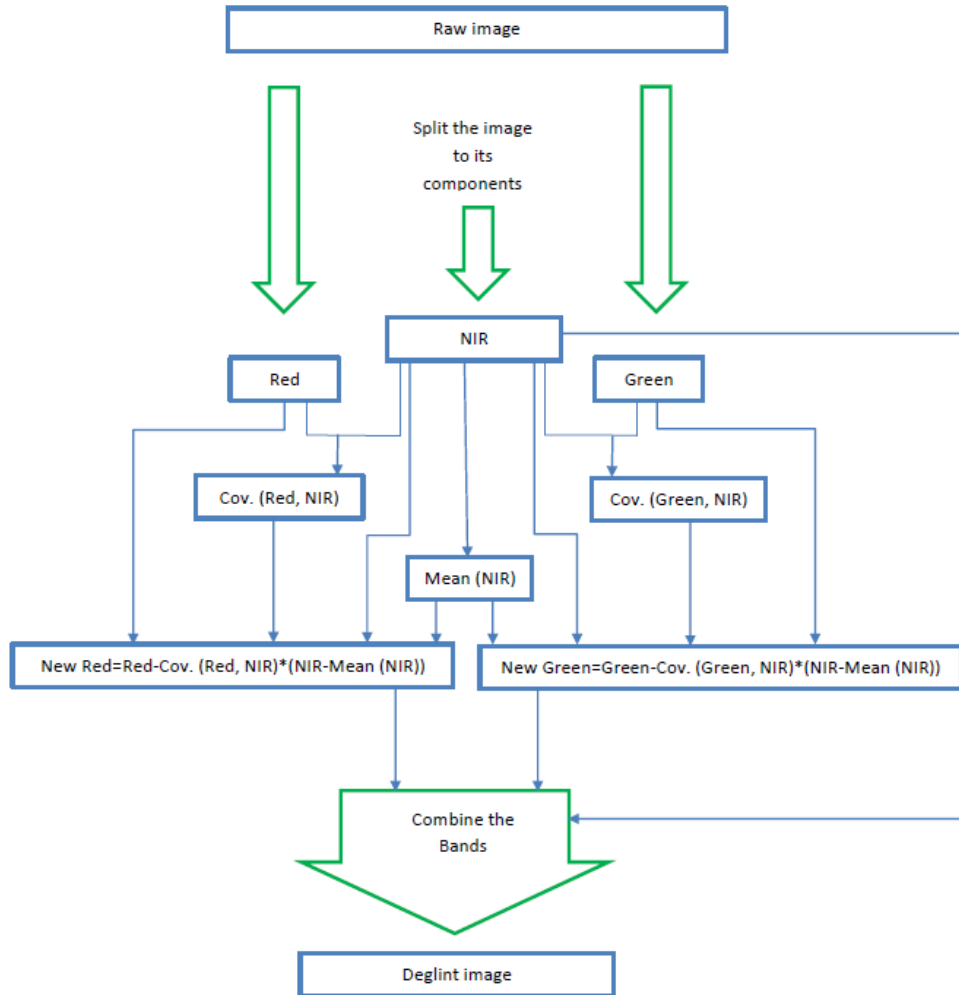


Figure 4.6. Flowchart of Lyzenga et al. (2006) algorithm for glint removal

Two codes were developed to implement these two algorithms in Matlab and process the imagery (Appendix 1). The imagery was then exported and analyzed in ArcGIS. The same process is done on the UAS images, which is explained in the UAS-SfM section.

The effectiveness of the sun glint removal imagery is examined in two ways: first, the submerged pipelines are delineated manually and the result is compared to the submerged pipeline delineation in the original imagery using ArcGIS. Second, the two glint corrected imagery are used as inputs to the edge detection image processing. The images are processed for

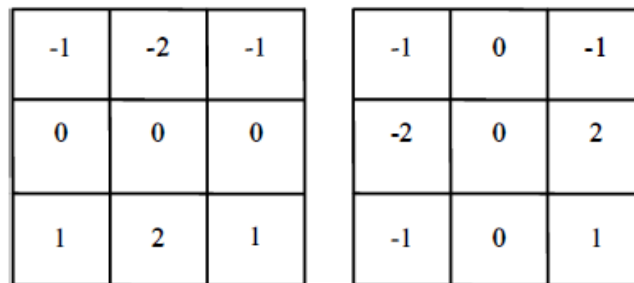
detecting the edges. The results are compared to the original imagery result in terms of noise and number of detected edges.

4.2.2 Edge detection

In this section, three different methods including Sobel, Prewitt, and Canny are examined to detect the edges in the imagery in order to delineate submerged pipelines. In all three methods the multiband images were converted to gray cell images and then processed. Routines were developed in Matlab to implement these algorithms (Appendix 1). The outputs were then exported in ArcGIS to analyze and illustrate.

4.2.2.1 Sobel

In this method, a pair of 3 x 3 convolution masks (Fig. 4.7) are slid over the image manipulating a 3 x 3 square of pixels at a time. The first convolution mask estimates gradient in the x-direction and the second estimates gradient in the y-direction. This operator works better on pixels that are closer to the center of the masks. In other words, edges of an image contain some error because of this mask. The detected edges are shown in the sample image in Shamrock Cove shoreline (Figure 4.8).



a) Convolution template S_x

b) Convolution template S_y

Figure 4.7. Two convolution masks in Sobel method (Kang and Wang 2007)

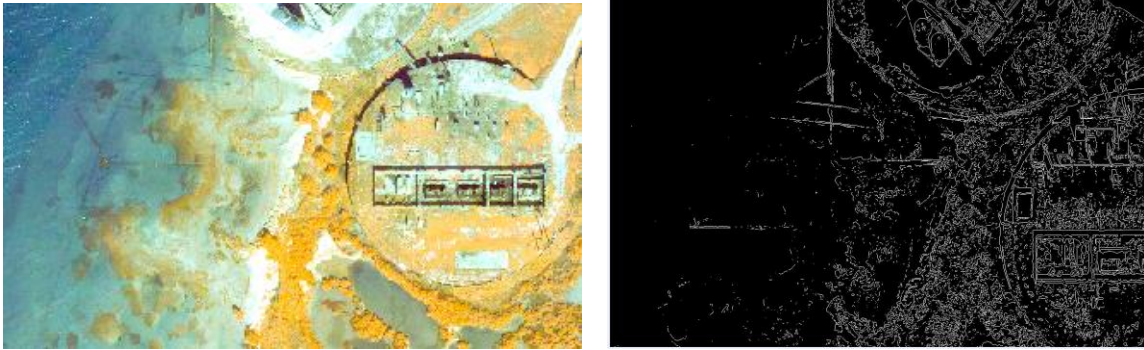


Figure 4.8. Sobel edge detection sample in Shamrock Cove shoreline

5.2.2.2 Prewitt

This method works similar to the Sobel method. However, its masks are different from the Sobel method (Fig. 4.7). In addition, unlike the Sobel operator, Prewitt operator does not place any emphasis on pixels that are closer to the center of the masks.

$$G_x = \begin{bmatrix} -1 & 0 & 1 \\ -1 & 0 & 1 \\ -1 & 0 & 1 \end{bmatrix} \quad G_y = \begin{bmatrix} -1 & -1 & -1 \\ 0 & 0 & 0 \\ 1 & 1 & 1 \end{bmatrix}$$

Figure 4.9. The horizontal and vertical Prewitt edge detection masks (Seif et al., 2010)

The sample output of Prewitt method in Shamrock Cove shoreline is shown in Figure 4.10.

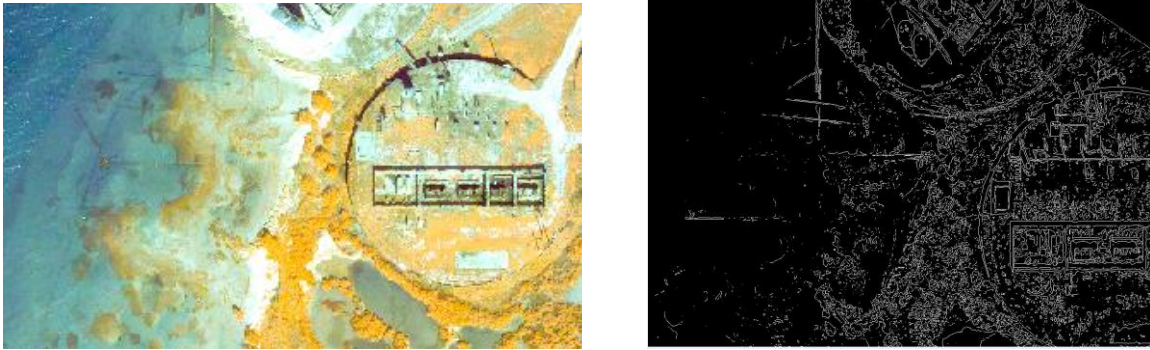


Figure 4.10. Prewitt edge detection sample in Shamrock Cove shoreline

4.2.2.3 Canny

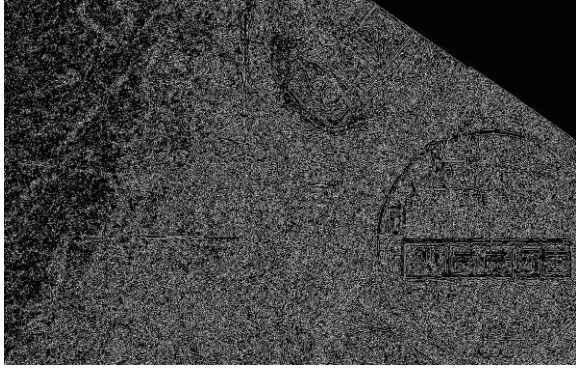
Canny edge detection uses linear filtering with a Gaussian kernel to smooth noise, and then computes the edge strength and direction for each pixel in the smoothing image. In the following, the steps for the Canny edge detection are explained. In the first step, the image becomes smooth with a Gaussian filter. Then the gradient magnitude and orientation is computed using finite-difference approximations for the partial derivatives. In the last step, non-maxima suppression (thinning process) is applied to the gradient magnitude using the double thresholding algorithm (Otsu) to detect and link edges. In this process, the edge strength of each candidate edge pixel is set to zero if its edge strength is not larger than the edge strength of the two adjacent pixels in the gradient direction. Thresholding is then done on the thinned edge magnitude image using hysteresis. In hysteresis, two edge strength thresholds are used. All candidate edge pixels below the lower threshold are labeled as non-edges and all pixels above the low threshold that can be connected to any pixel above the high threshold through a chain of edge pixels are labeled as edge pixels (Heath et al., 1997).

Canny method is a tradeoff between three parameters which are sigma, low threshold, and high threshold. By changing the value of these parameters, the connectivity and noise will be changed in the output image. These parameters are chosen based on trial and error in terms of

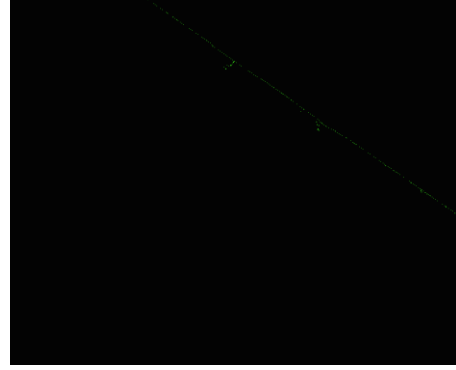
noise and edge connectivity in the output. Therefore, in order to find the optimal amount for the parameters, the different values are given to sigma and thresholds to examine the noise of the output and the connectivity of the detected edges (Table 4.4). First, the values of low threshold and high threshold are given [low T=.5, high T=1(pixel size)]. Then the other values are examined [low T=5, high T=10]. In this case, the output shows that most of the edges are lost. When the value of low threshold and high threshold are given 1 and 3 respectively, the results are much better comparing to other amounts of thresholds. Different values of sigma are examined as well. The results show that small values of sigma that are less than one, for example 0.1 or 0.5 make more noise in the output while the detection of large values is weak with blurry edges. Figure 4.11 displays tradeoffs for the Canny edge detector. The best fit parameters (Sigma=1, Threshold [1, 3] (pixel size)) are chosen to run this algorithm on all images. In addition, the Canny edge detector is run on the deglint images and two outputs are compared to each other.

Table 4.4. Canny parameters tradeoff

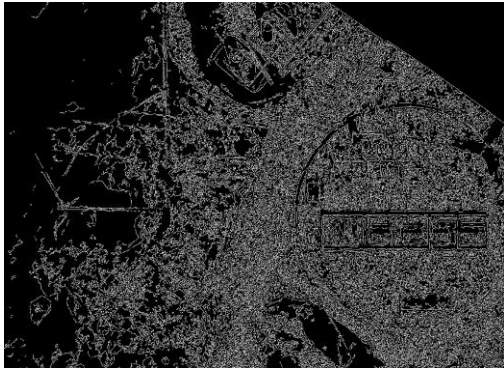
No	Operator	Sigma	Low Threshold	High Threshold
1	Canny	1	.5	1
2	Canny	1	5	15
3	Canny	1	1	3
4	Canny	0.1	1	3
5	Canny	0.5	1	3
6	Canny	2	1	3
7	Canny	5	1	3
8	Canny	10	1	3



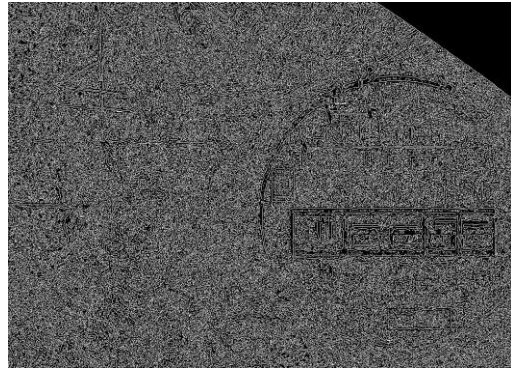
(1)



(2)



(3)



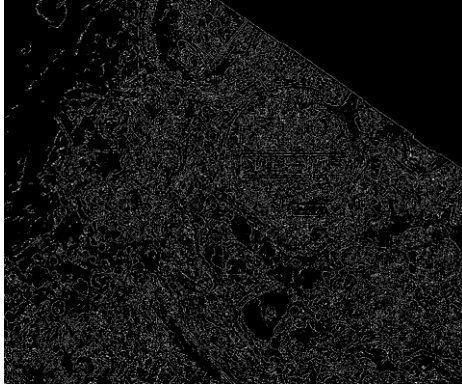
(4)



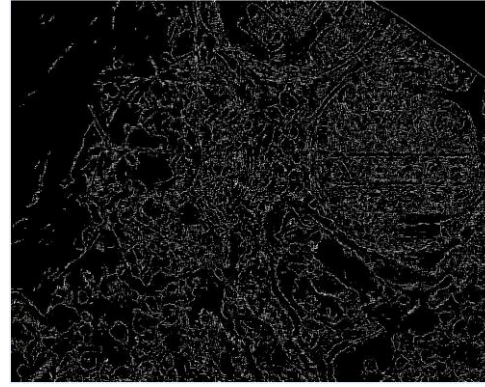
(5)



(6)



(7)



(8)

Figure 4.11. Canny parameters tradeoff based on Table 4.2

4.2.2.4 Evaluation using ground truth

Usually, the assumed-true data are derived from ground-truth data. In this study two sources are used for ground truth. First one is the existing shape file of GLO website. Second source is submerged pipelines which are manually delineated using the aerial imagery. ArcGIS is used for the geodatabase and the outputs are overlaid with each other in it. This evaluation is based on visual inspection, which means that the pipes could be detected by the operator. To evaluate the approaches above several parameters are defined including number of the edges, noise or unwanted detail, localization or displacement from the original position, and edge continuity. Detected edges are counted manually by comparing to ground truth. Localizations are derived directly from the map by measuring the perpendicular distance between the edge and ground truth pipe in ArcGIS. Noise is a salt and pepper effect in the result or unwanted edges that causes ambiguity in the result. Edge continuity means the detected edge is a continuous line not dash line. Noise and edge continuity are described as the attributes: High, Medium, and Low. Noise and edge continuity are not absolute. They are evaluated by relative comparison from one method to another.

The three edge detection methods were run over glint corrected images as well as the original images. The processing was the same as the original images but the result might change in terms of detecting edges.

4.3 UAS Structure from Motion photogrammetry

Previous research shows that SfM photogrammetry for shallow water bathymetric mapping can often result in erroneous clusters of point elevations due to false feature matching and correspondence breakdowns stemming from sun glint (Giessel and Starek, 2015). Sun glint is often evident in remotely sensed imagery of high spatial resolution that depicts aquatic environments. The problem occurs when the water surface is not flat and the sun radiation is directly reflected to the sensor affecting the pixel brightness values. Therefore, in this section the effectiveness of sun glint correction and single band vs. multiband image preconditioning on SfM results are assessed.

The images are preprocessed to generate single band (red, green, NIR) images and deglint images using the Lyzegna et al., 2006 and Hedley et al., 2005 algorithms implemented with Matlab (same as done for the aerial imagery). Each of the generated “deglinted” data sets is then input into the SfM- processing chain to generating a 3D topo-bathymetric point cloud and subsequently generate a DSM. All SfM processing here was performed using the well-known and powerful commercial UAS photogrammetry software Pix4D.

Following is the brief description of the steps perform to create a 3D point cloud and subsequent DSM from the non- processed and preconditioned UAS imagery using Pix4D. A project is set up where the images and camera model are entered into the software. In the camera model, the type of the bands is set in terms of single or multiband. For instance, R-G-NIR includes three bands, which are red with a peak spectral response near 625 nm wavelength, green

near 580 nm wavelength and NIR near 880 nm wavelength. However, in the case of using single band, just one of the bands is involved in the calculation. In the next step, image-by-image key point extraction occurs using scale-invariant feature transform (SIFT) algorithm. The vertical datum which is used in this study is the ellipsoid and horizontal datum and projection is WGS 84- UTM-14N. In contrast to traditional photogrammetry, SfM does not explicitly require use of ground control points (GCPs), clearly identifiable locations with known or assumed real-world coordinates. Adding ground control points to the project results in accurately georeferencing the point clouds generated after accurate image matching. In general, accurate ground control data are used to optimize the parameters with higher accuracy. However, in this study, ground control points were not used to avoid the subjectivity involved with picking coordinates based on control points in the images. By removing any subjectivity, the assessment remains focused on the main SfM components of feature correspondence and point cloud density results under the water. Picking targets were not selected for more absolute georeferencing because it induces some subjectivity in the process whereas the goal is to assess the differences in SfM-output 3D point cloud characteristics. In the next phase, automatic aerial triangulation which computes the 3D coordinate of individual key points is done. By using bundle block adjustment technique to image block adjustment, accurate information (position and orientation (interior and exterior)) of camera is recomputed for every image. The point cloud generated during the initial processing step was matched along the multiple images which caused a much more dense point cloud. Dense stereo matching algorithm (Zhang et al., 2012) is used to generate dense point clouds. In the last step, the dense point clouds generated this way are then interpolated to form a tin in order to obtain a digital surface model in the software. As it is mentioned above, single band images are extracted from original imagery by splitting the green band (near 550 nm), red (near 625 nm),

and NIR (near 880 nm). The same process is run for single band images and a DSM is generated. In addition, glint removal algorithms are applied on original images and the process of extracting a point cloud and creating a DSM are repeated from the beginning to the end. Each single band imagery including red, green and NIR is processed separately in the Pix4D as well as the multiband UAS imagery. Point density, key point matching, and number of points are conducted.

In order to evaluate glint corrected and single bands vs original multiband, the generated point clouds are clipped in water and land separately. The height outliers (out range elevations) are calculated based on quartiles: first the lower and upper quartile (Q_1, Q_3) are conducted, then the interquartile range is calculated, and finally the inner fence is defined for the data set.

$$D = Q_3 - Q_1 \quad (4.3)$$

$$Range = [Q_1 - (Q_3 - Q_1)^2, Q_3 + (Q_3 - Q_1)^2] \quad (4.4)$$

A tile with the dimensions of 5x5 m is defined and used to pass through all of the data set (point clouds). The outliers are removed from the sample by comparing each point to the range in the boundary of the 5x5 m tile separately in all data sets. Because the comparisons within the tile occur in a small space, the tile successfully compares the outliers and removes them. Statistical parameters (min, max, mean, mode, median, and standard deviation) of x, y, and z (height) are calculated for each single band (green, red, NIR), two glint removal methods, and the original generated point clouds. The results are compared with each other in terms of statistic elements, point density, key point matching, and number of points.

The 3D point clouds derived from the SfM technique for each method (non-processed image inputs, glint corrected image input, and single vs. multiband image input) are assessed in terms of point density, number of points, statistical parameters, and elevation. Statistical analyzes

and outlier removals are conducted in Matlab. The procedure of this process is shown in Figure 4.12.

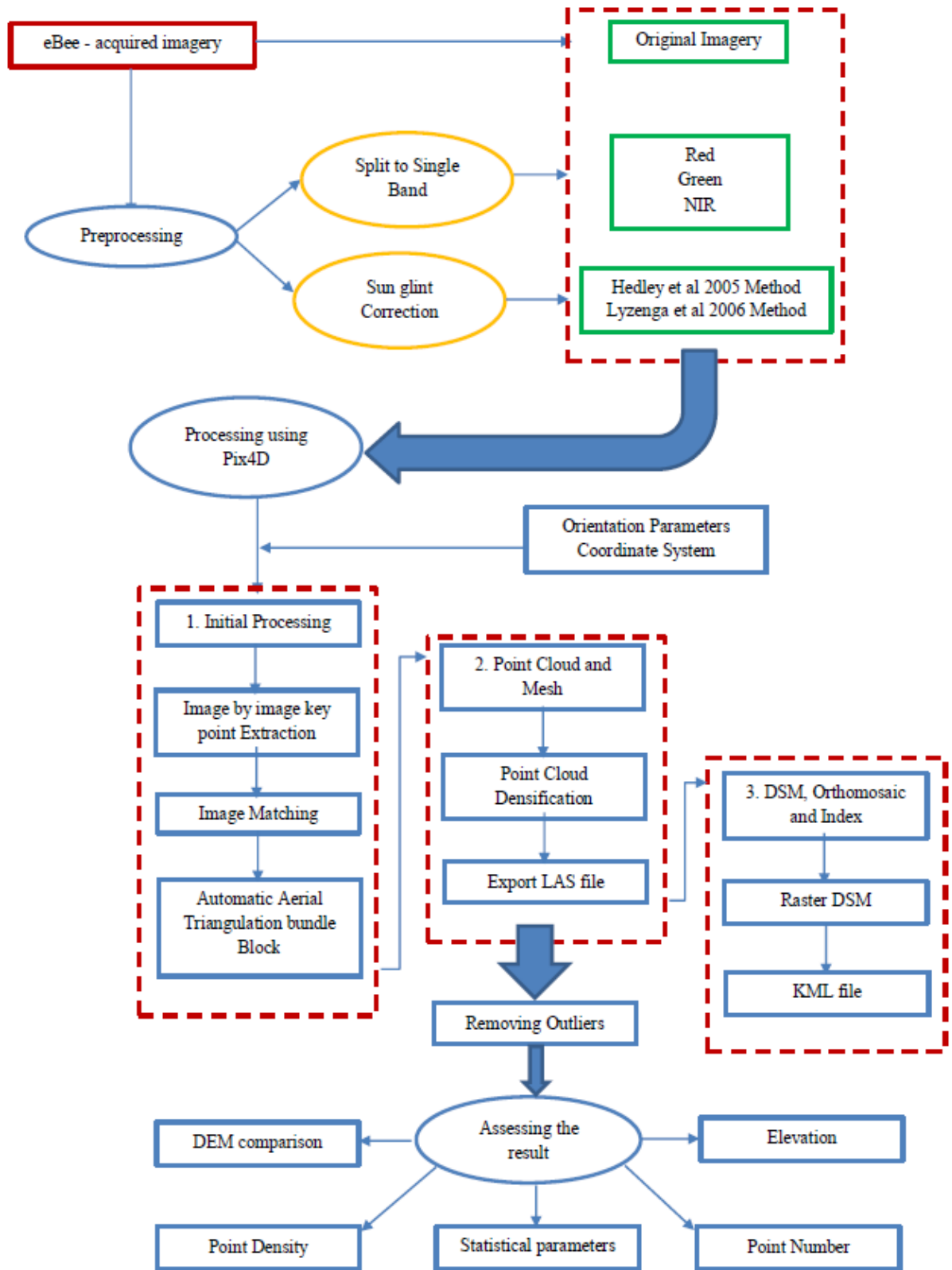


Figure 4.12. UAS-SfM workflow

CHAPTER 5

RESULT AND DISCUSSION

5.1 Result

5.1.1 Bathymetric lidar

DEMs were generated for three cell sizes (0.50, 1, and 2 m) in each interpolation method: TIN, IDW, and B-spline. DEMs and Shaded reliefs with different settings were created for each cell size in all methods (Fig. 5.1 to Fig. 5.5).

In regards to assessing the different methods of interpolation, the output of three methods are compared in terms of vertical accuracy and delineating pipelines. RMSE is calculated for each method based on RTK-GPS points and corresponding points in the DEM. RMSE is calculated for each cell size (0.5, 1, and 2 m). Table 5.1 shows the result for each method evaluated: TIN, IDW, and B-spline for all points. In addition, RMSE of three different land types (bathymetry, land, and vegetation) are calculated for each cell size (Table 5-2 to Table 5.4).

Table 5.1. Interpolation methods vertical accuracy based on RMSE- all points

No	Interpolation Method	RMSE (m) Cell size =0.50 m	RMSE (m) Cell size =1 m	RMSE (m) Cell size =2 m
1	Multilevel B-Spline	0.16	0.17	0.21
2	2D Delaunay TIN	0.30	0.24	0.27
3	IDW	0.29	0.25	.28

Table 5.2. Interpolation methods vertical accuracy based on RMSE- bathymetry

NO	Interpolation Method	RMSE (m) Cell size =0.50 m	RMSE (m) Cell size =1 m	RMSE (m) Cell size =2 m
1	Multilevel B-Spline	0.17	0.06	0.28
2	2D Delaunay TIN	0.09	0.07	0.10
3	IDW	0.10	0.14	.15

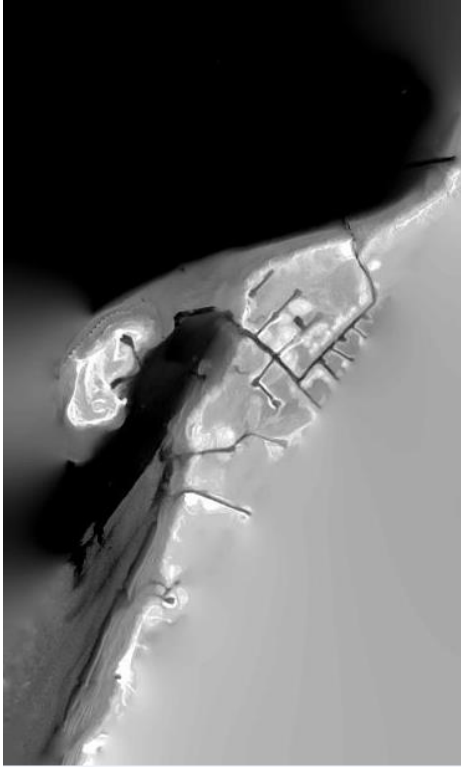
Table 5.3. Interpolation methods vertical accuracy based on RMSE- land

NO	Interpolation Method	RMSE (m)	RMSE (m)	RMSE (m)
		Cell size =0.50 m	Cell size =1 m	Cell size =2 m
1	Multilevel B-Spline	0.13	0.09	0.20
2	2D Delaunay TIN	0.08	0.08	0.13
3	IDW	0.13	0.28	0.31

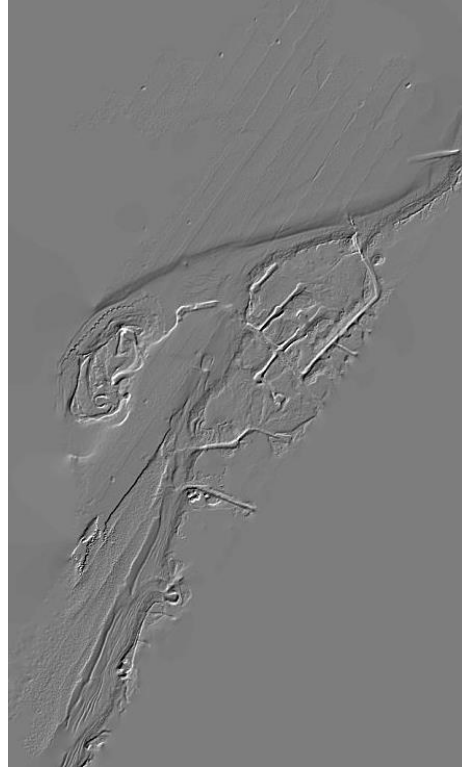
Table 5.4. Interpolation methods vertical accuracy based on RMSE- Vegetation

NO	Interpolation Method	RMSE (m)	RMSE (m)	RMSE (m)
		Cell size =0.50 m	Cell size =1 m	Cell size =2 m
1	Multilevel B-Spline	0.11	0.05	0.13
2	2D Delaunay TIN	0.43	0.44	0.27
3	IDW	0.15	0.06	0.30

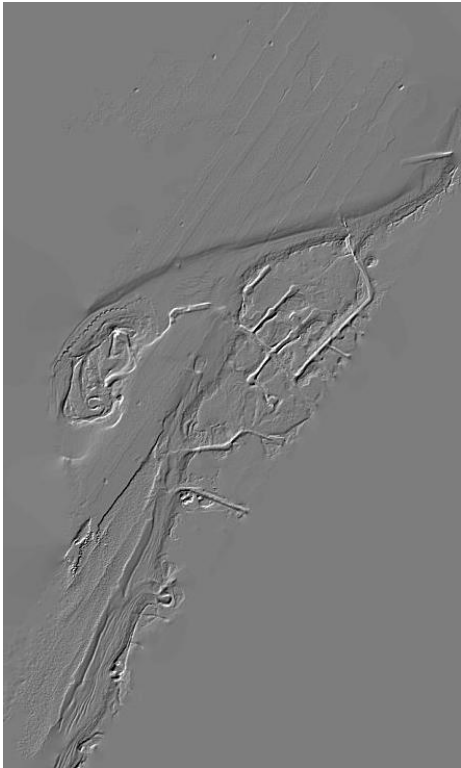
The RMSE- all points showed that the multilevel B-spline method had the lowest RMSE between all three methods for all three cell sizes. In this case, it showed slightly more accurate surface reconstruction compared to the other methods tested here. In the bathymetry section, the multilevel B-spline performed best with a cell size of 1 m compared to TIN and IDW in the same cell size, while this method had the worst result for the cell size of 2 m. TIN method had the best result in land RMSE, while this method had the worst result in vegetation RMSE in all for all cell sizes. IDW had the lowest RMSE in vegetation area compared to RMSE of this method on land and water.



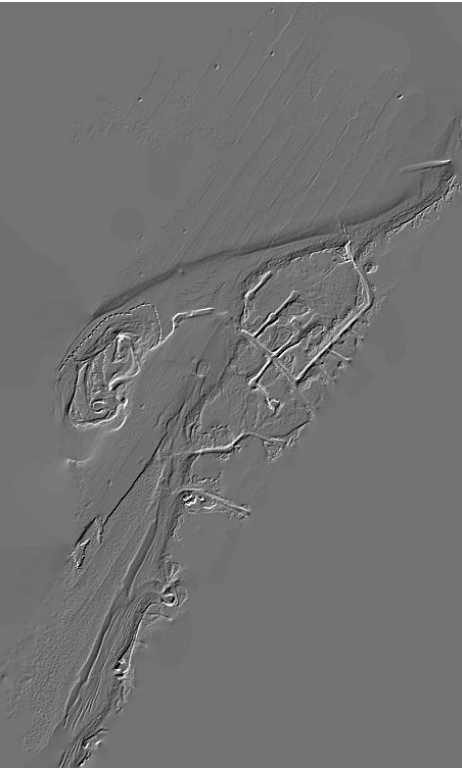
(a)



(b)

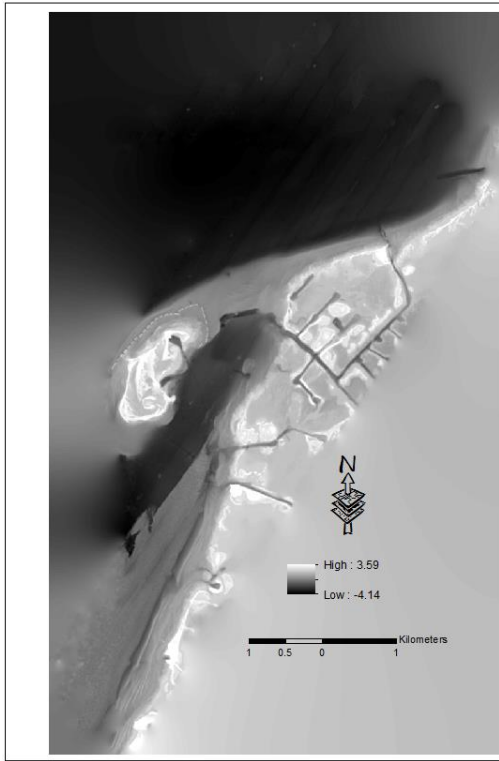


(c)

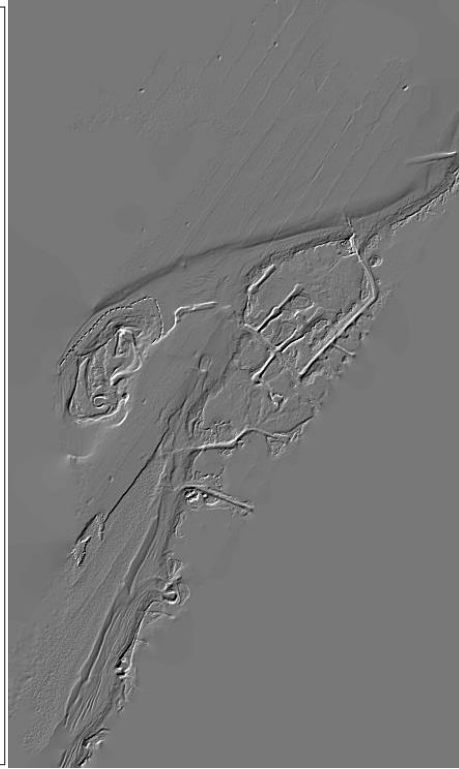


(d)

Figure 5.1. B-spline interpolation cell size=2 a) DEM b) Shaded relief h= 30 c) Shaded relief h= 45 d) Shaded relief h= 60



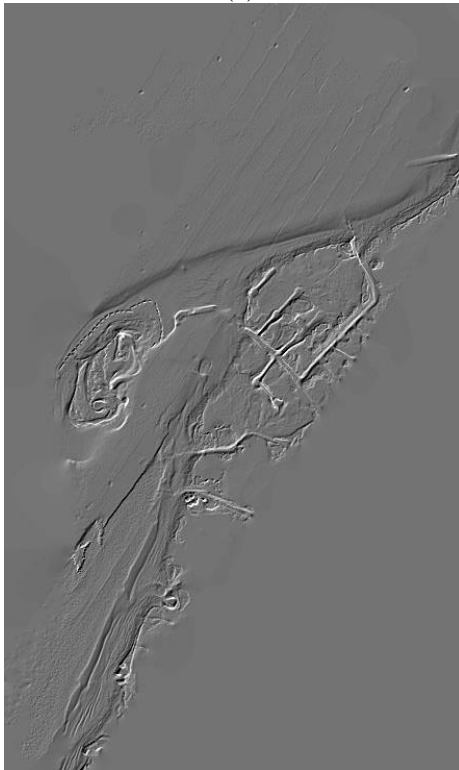
(a)



(b)

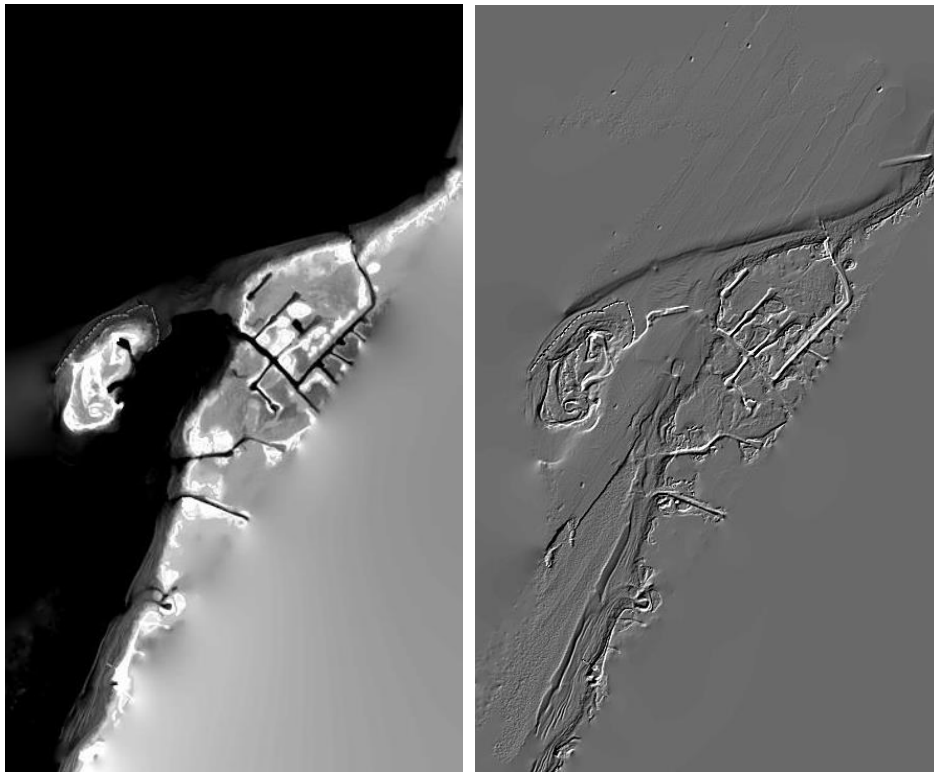


(c)



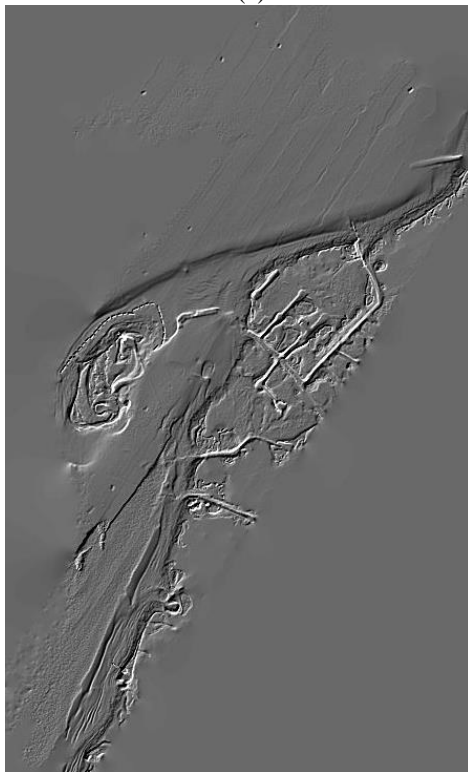
(d)

Figure 5.2. B-spline cell size=1 a) DEM b) Shaded relief h=30 c) Shaded relief h=45 d) Shaded relief h=60

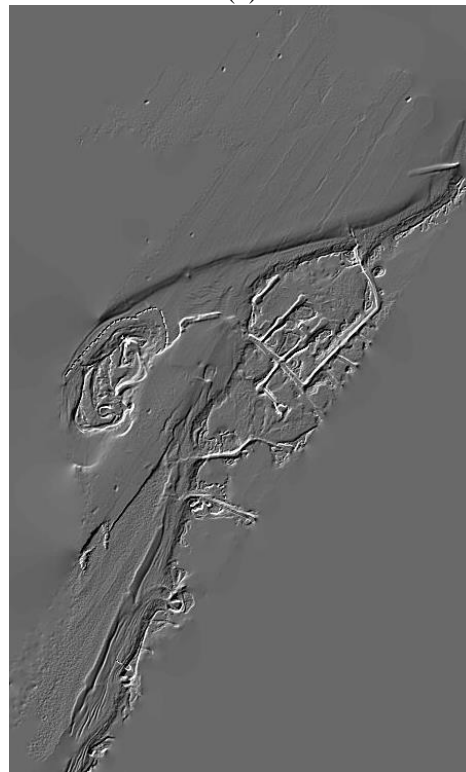


(a)

(b)



(c)



(d)

Figure 5.3. B-spline cell size 0.50 a) DEM b) Shaded relief $h=30$ c) shaded relief $h=45$ d) shaded relief $h=60$

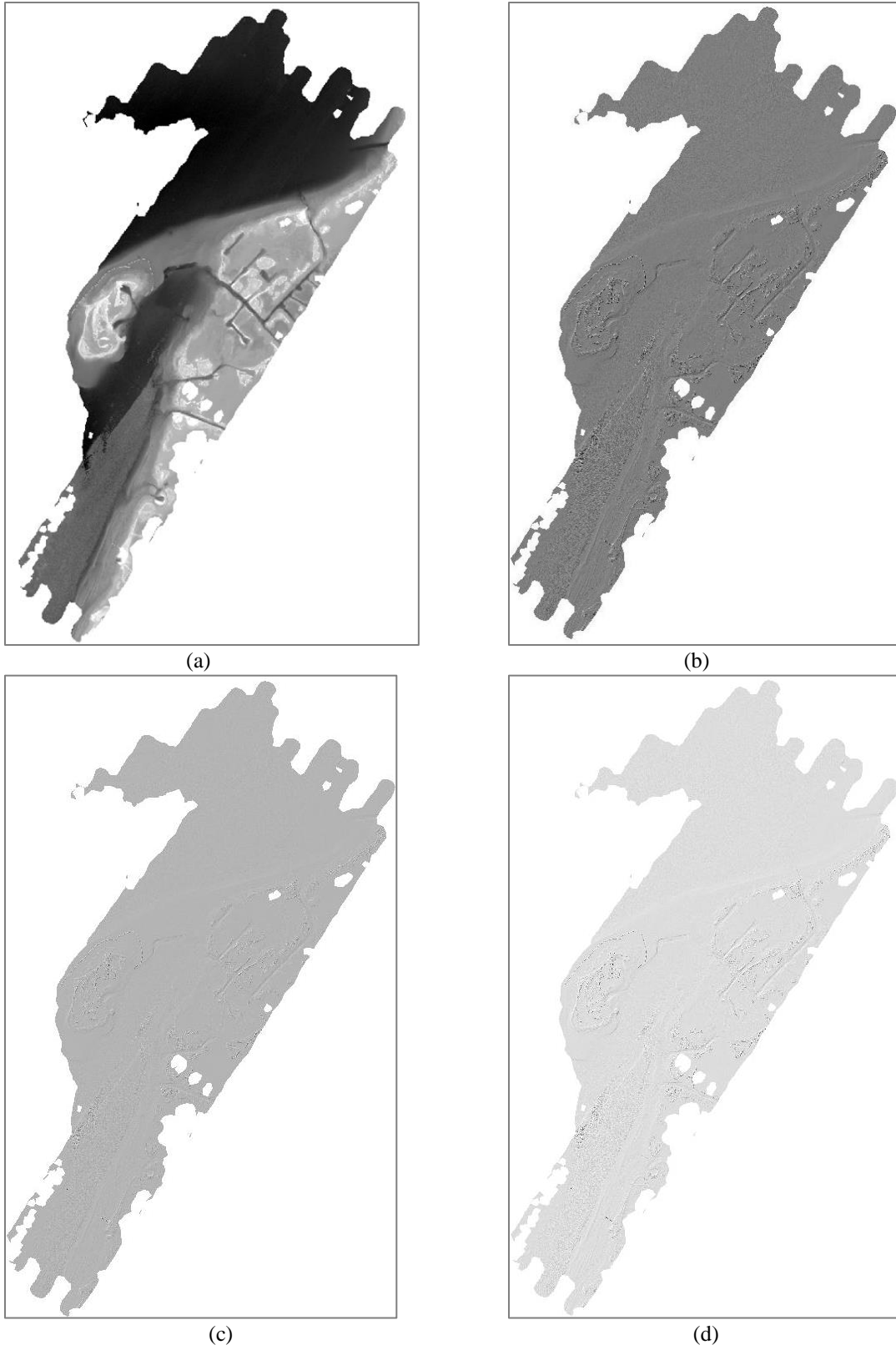


Figure 5.4. TIN cell size 2 a) DEM b) Shaded relief $h=30$ c) shaded relief $h=45$ d) shaded relief $h=60$

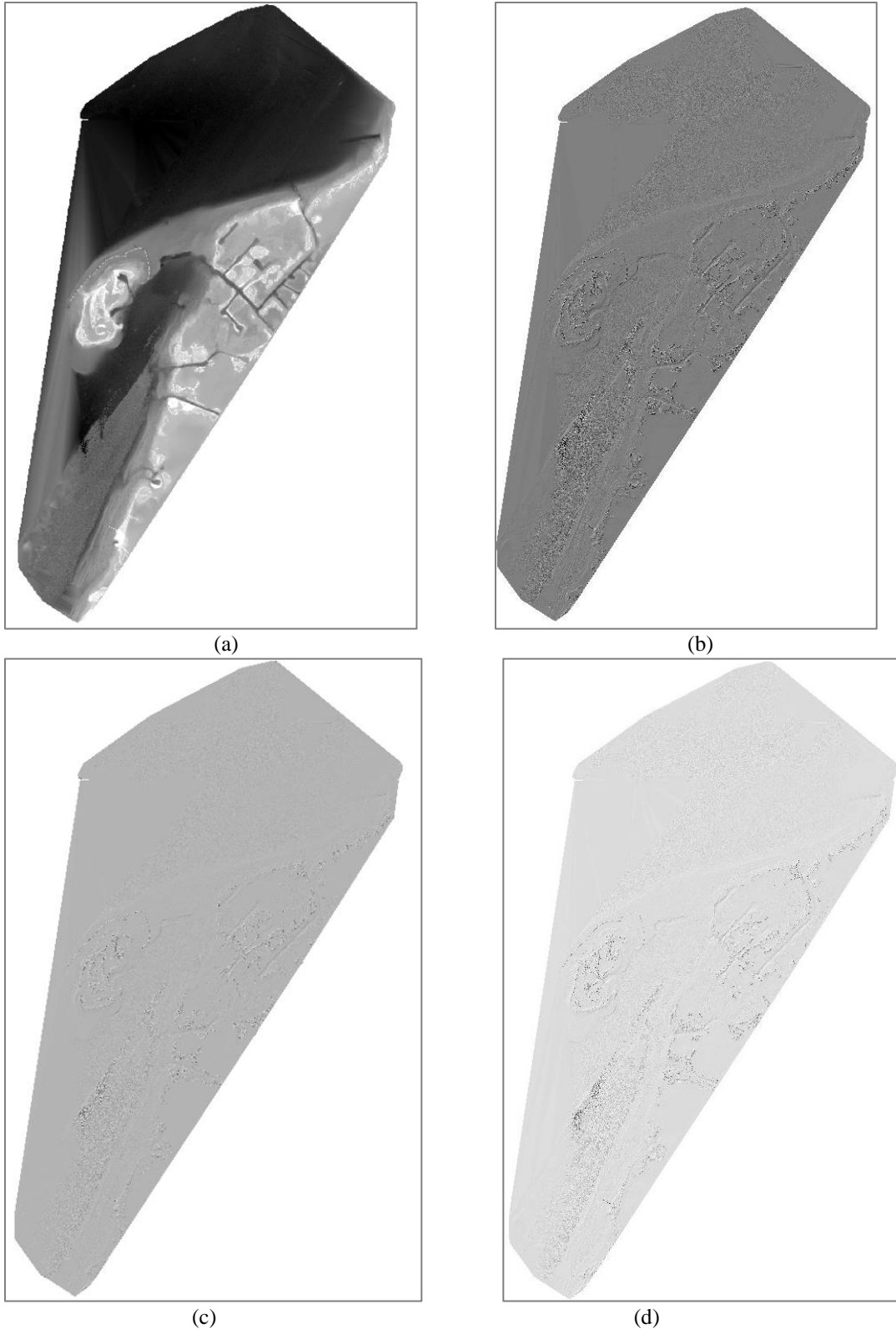
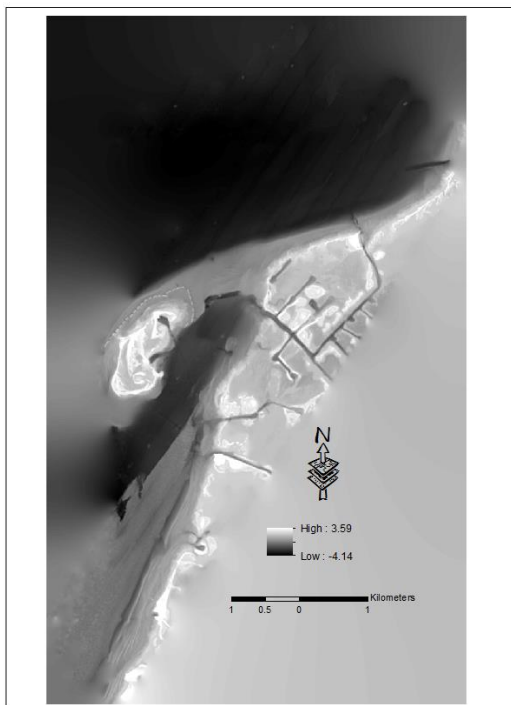
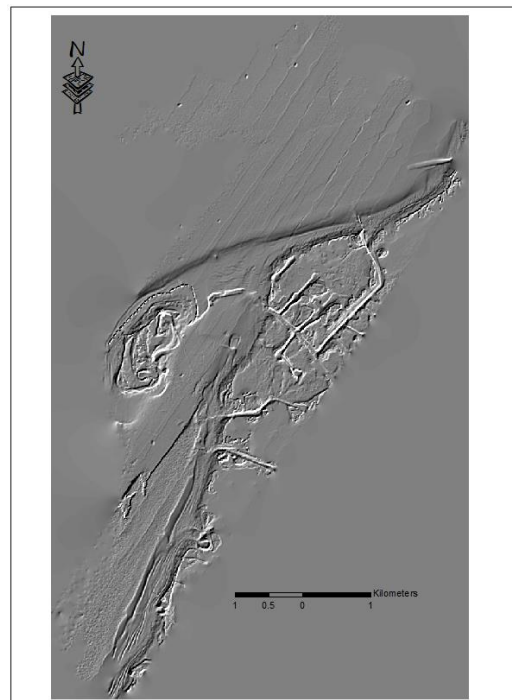


Figure 5.5. IDW cell size 2 a) DEM b) Shaded relief $h=30$ c) shaded relief $h=45$ d) shaded relief $h=60$

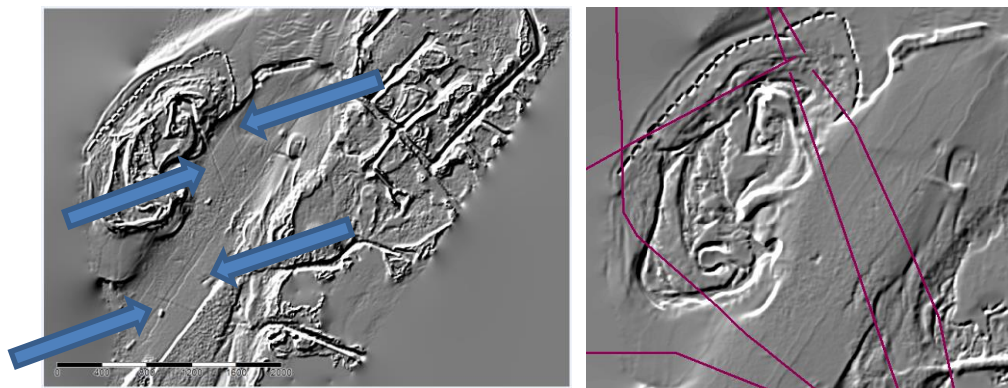
For the submerged pipeline delineation, all the DEMs of these three interpolation methods and related shaded relief models with different parameters that were mentioned in methodology including sun angle were inspected. The inspection based on known locations shows that the four major submerged pipelines are apparent in the multilevel B-spline interpolation with all three cell sizes tested (Fig. 5.6) while in the 2D TIN Delaunay method, two pipelines are found (Fig. 5.14). Only one pipeline is found in the IDW method (Fig. 5.15). To prove what pipelines are found, the existing pipeline shapefile by GLO is overlaid on these shaded reliefs as ground truth. It should be noted that some of the pipes in the DEM do not coincide with those in the GLO shapefile. The misplacement may occur because of little to no updating of the GLO maps.



(a)



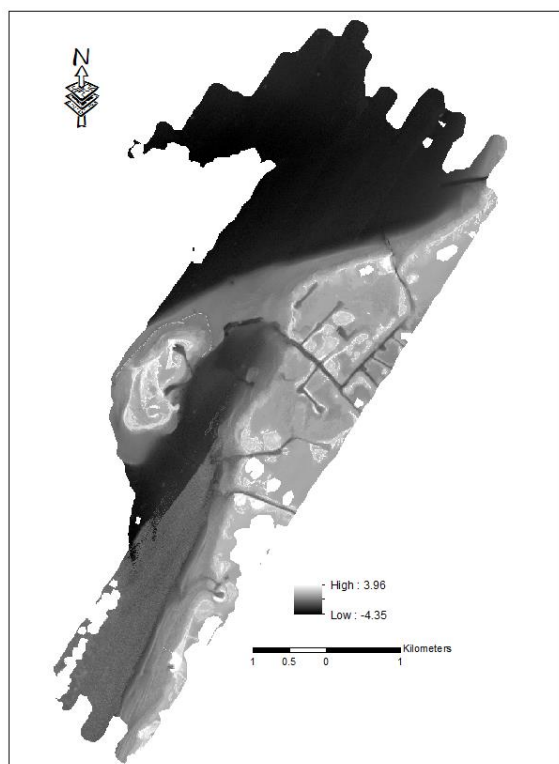
(b)



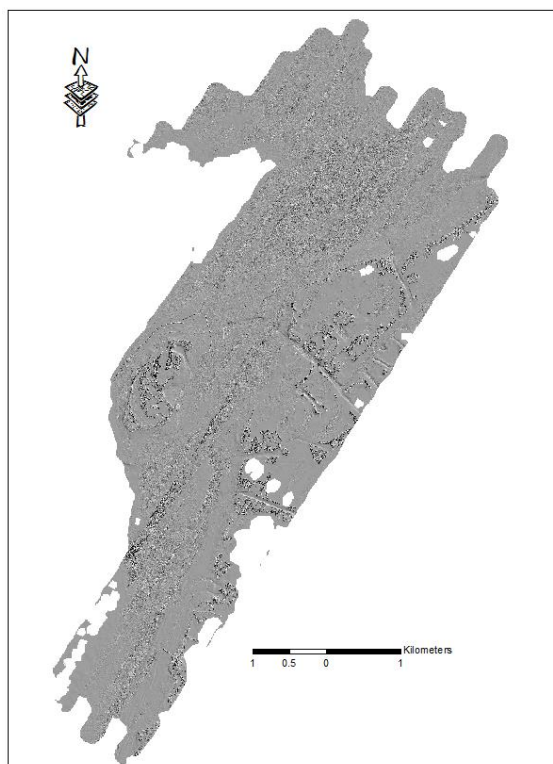
(c)

(d)

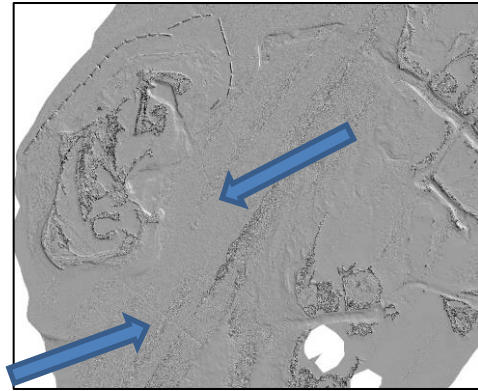
Figure 5.6. (a) DEM (cell size =1) color coded by elevation (brighter = higher elevation) and (b) shaded relief derived from multilevel B-spline interpolation. (c) In this method four major pipelines are apparent. The GLO shapefile is overlaid on the shaded relief as ground truth (d).



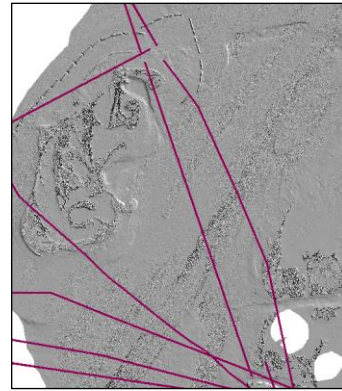
(a)



(b)

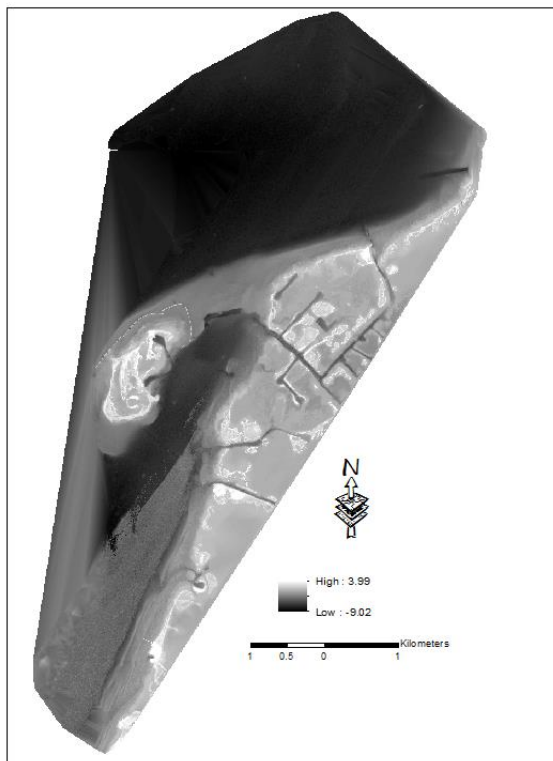


(c)

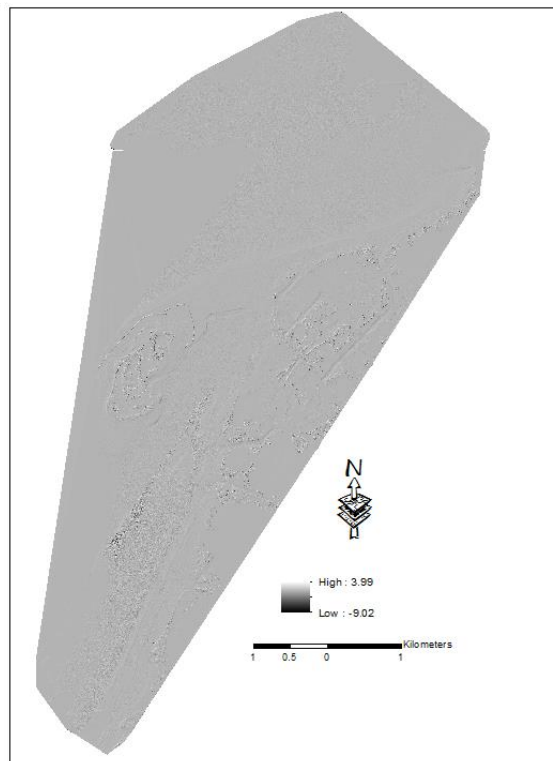


(d)

Figure 5.7. DEM (cell size=1) color coded by elevation (brighter = higher elevation) and (b) shaded relief (2D Delaunay TIN). In this method two major pipelines are apparent (c). The GLO shapefile is overlaid on the shaded relief as ground truth (d).



(a)



(b)

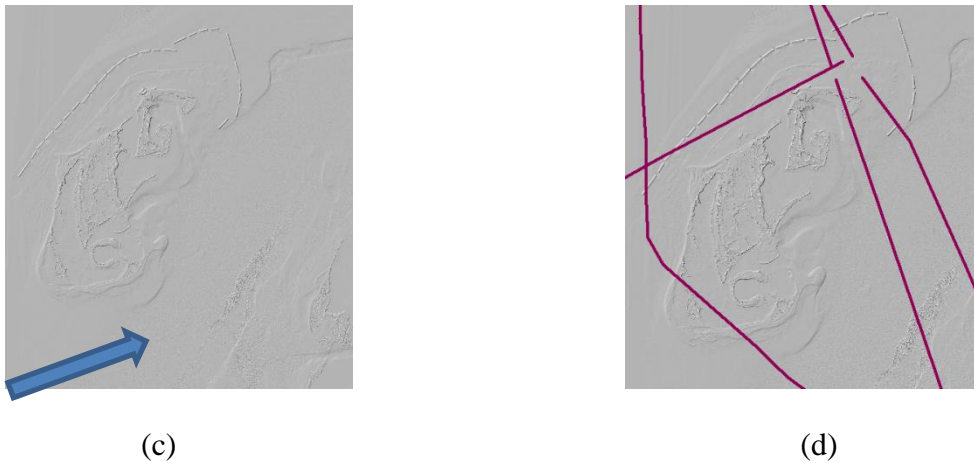


Figure 5.8. DEM (cell size=1) color coded by elevation (brighter = higher elevation) and (b) shaded relief (IDW). In this method one major pipeline is apparent (c). The GLO shapefile is overlaid on the shaded relief as ground truth (d).

5.1.2 Aerial digital imagery

Another component of this study was to examine the use of imagery to detect submerged pipelines. In this section the results of sun glint correction and edge detection methods are illustrated.

5.1.2.1 Sun glint removal

Image enhancement is applied to the airborne images as a preprocessing approach prior to any further image processing. As mentioned in the methodology, two algorithms in sun glint correction were evaluated: Hedley et al. (2005) and Lyzenga et al. (2006). Sun glint contamination can cause substantial loss in data fidelity below the water surface. In fact, these methods can generally only correct moderate glint and large errors may still remain in the brightest glint areas. The Hedley et al. (2005) method uses the minimum NIR in its calculations while the Lyzenga uses mean NIR. The results are shown in Figure 5.9. Both methods have been successful in increasing the proportion of data below the surface that can be retrieved from shallow water. Hedley et al. (2005) loses less data compare to Lyzenga et al. (2006) in the

airborne imagery, because it subtracts minimum NIR from the image and Lyzenga et al. (2006) subtracts the average of NIR in the image.

Figure 5.9 shows some samples of glint corrected images by the two methods.

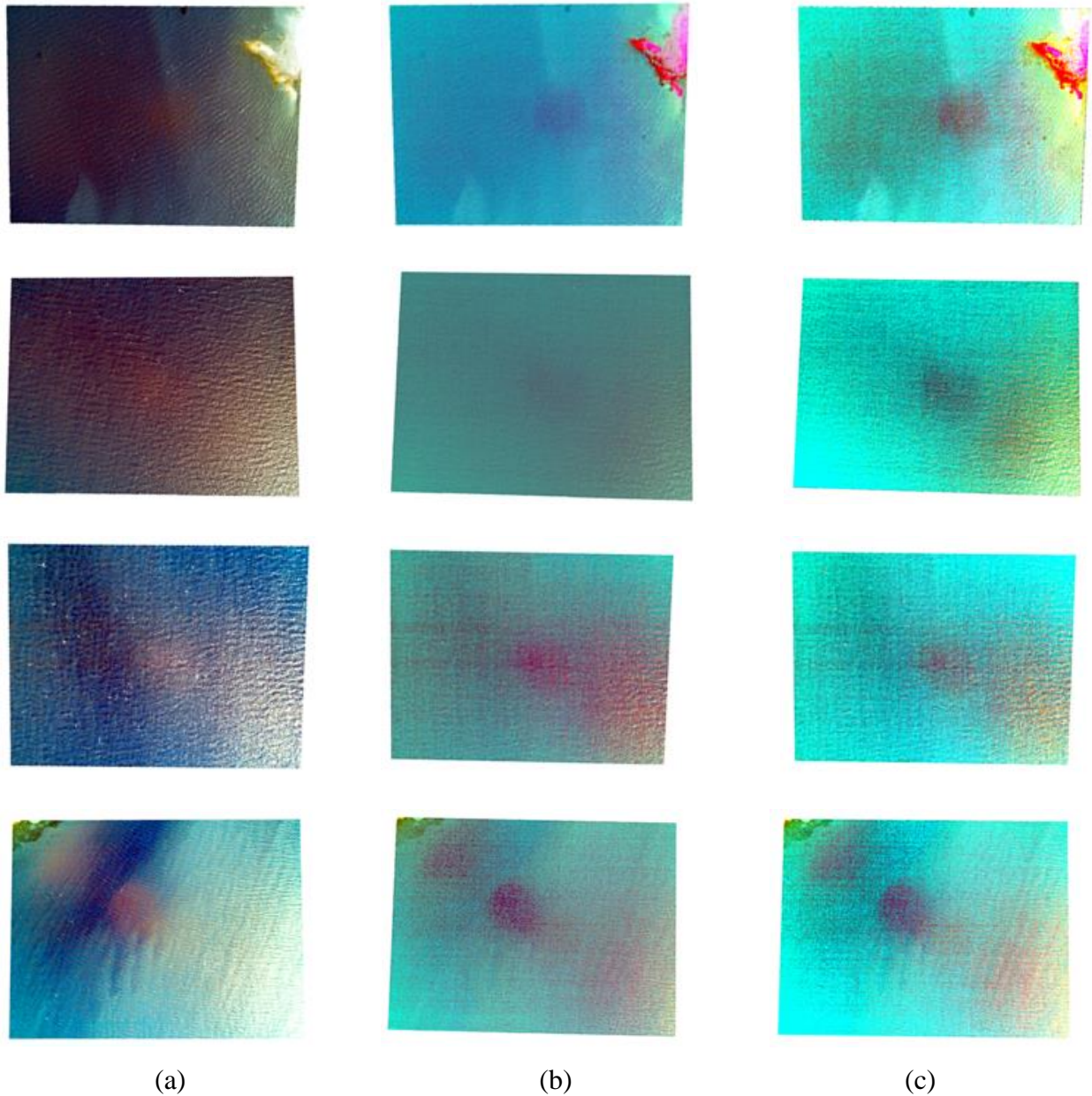


Figure 5.9. (a) Original Image, (b) Deglint Image (Hedley et al., 2005), (c) Deglint Image (Lyzenga et al., 2006) (image size 355 x 267 meters)

Because the sun glint occurs when sun radiation is directly reflected to the sensor over the water surface, the behavior of the radiation is examined in a sample image which covers shallow water in Shamrock Island Cove before and after glint correction for each method. The diagram below shows the effect of glint removal on the sample image based on a digital number value and wavelength of the three bands (NIR, Green, and Red). The result shows that the brightness decreases when glint is removed from the image due to the subtraction of digital number values from the imagery. Figures 5.10 shows that the Hedley et al. (2005) has lower radiance compare to the Lyzenga et al. (2006) (Fig. 5.10).

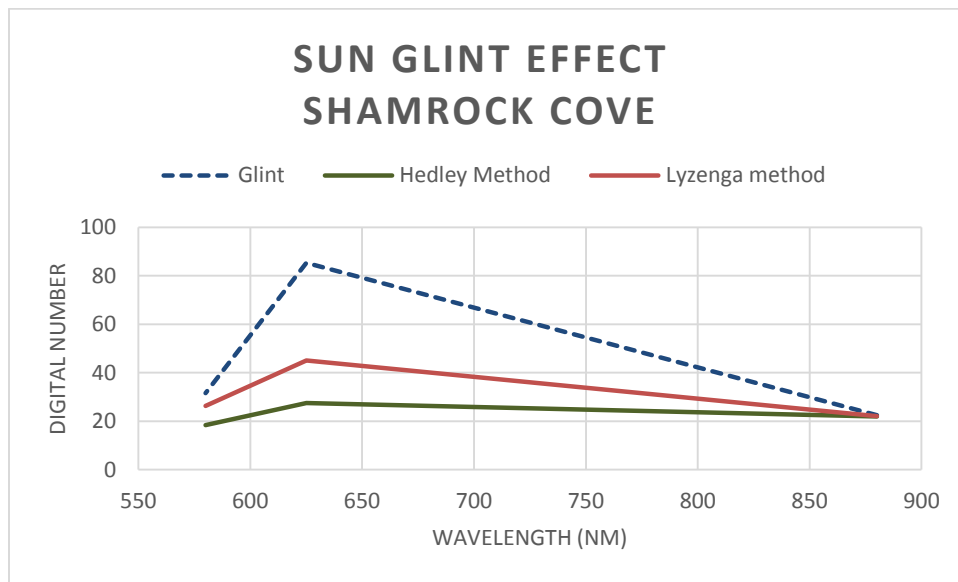


Figure 5.10. Spectral analysis-Sun glint removal effect for average across several pixels in a sample image

The remaining glint in the Hedley method is lower, because the NIR values are taken towards the minimum value while the mean NIR is used in the Lyzenga method. In other words, based on the Figure 5.10 the remaining brightness which is glint reflection of Hedley et al. (2005) is lower than the Lyzenga method. However, both methods are used for further processing on this data set. The mosaic of the deglint images is shown in Figure 5.11.

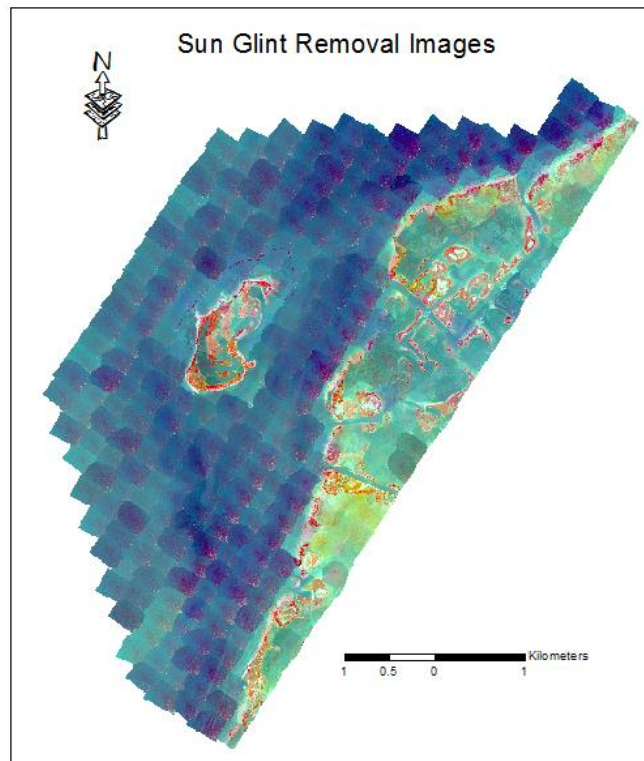


Figure 5.11. Deglint mosaic data set

A shapefile was created in ArcGIS and the submerged pipelines manually delineated based on visual inspection in the original and sun glint corrected imagery. Sun glint corrected imagery provided better visualization to detect the pipes. However, the number of the detected pipes were the same. In both data sets 125 pipes were delineated.

In the other section of this study, these two methods were examined on edge detection image processing and UAS-SfM imagery to assess the effectiveness of the sun glint correction.

5.1.2.2 Edge detection

In edge detection, three different methods of edge detection were examined to detect the submerged pipelines including Sobel, Prewitt, and Canny. Each of which was run over the images and the output is the image with two colors which correspond to the edges and the background. Each method was assessed based on some parameters including detected edges,

noise, localization or displacement from center, and edge continuity which were described in the methodology. The GLO shapefile and imagery were used to define the ground truth. These parameters were manually measured and compared in ArcGIS.

Table 5.6 illustrates this evaluation for Sobel, Prewitt, and Canny approaches.

Table 5.5. Evaluation based on ground truth

No	Approach	Edge Detection	Noise	Localization	Edge Continuity
1	Canny(1,[1,3])	74 out of 125	Medium	0.25 m off from center	High
2	Sobel	50 out of 125	Low	0.35 m off from center	Low
3	Prewitt	50 out of 125	Low	0.35 m off from center	Low

The ground truth feature class, which was overlaid on the map, shows that Sobel and Prewitt methods work similarly to each other in terms of delineating pipelines and noise. These operators can only delineate the pipelines up to 40%, although their noise is less than the Canny method (Fig. 5.12). The Canny method depends on its parameters in delineating the features. In other words, decreasing “ σ ” would show more details, and changing thresholds would change edge linking. Different values of parameters in Table 2.2 were examined and optimal values were chosen which are $\sigma = 1$, Low T =1, and High T= 3 which would help to get more than 60% of pipelines by trial and error for setting parameter values. Figure 5.13 shows the result of Canny method.

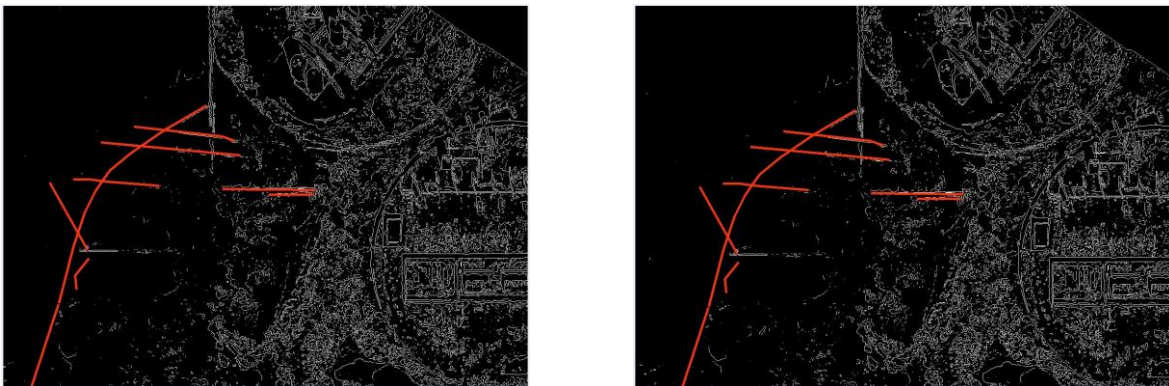


Figure 5.12. Ground truth: Sobel edge detection (Left); Prewitt edge detection (Right); the red lines in both pictures show the ground truth.

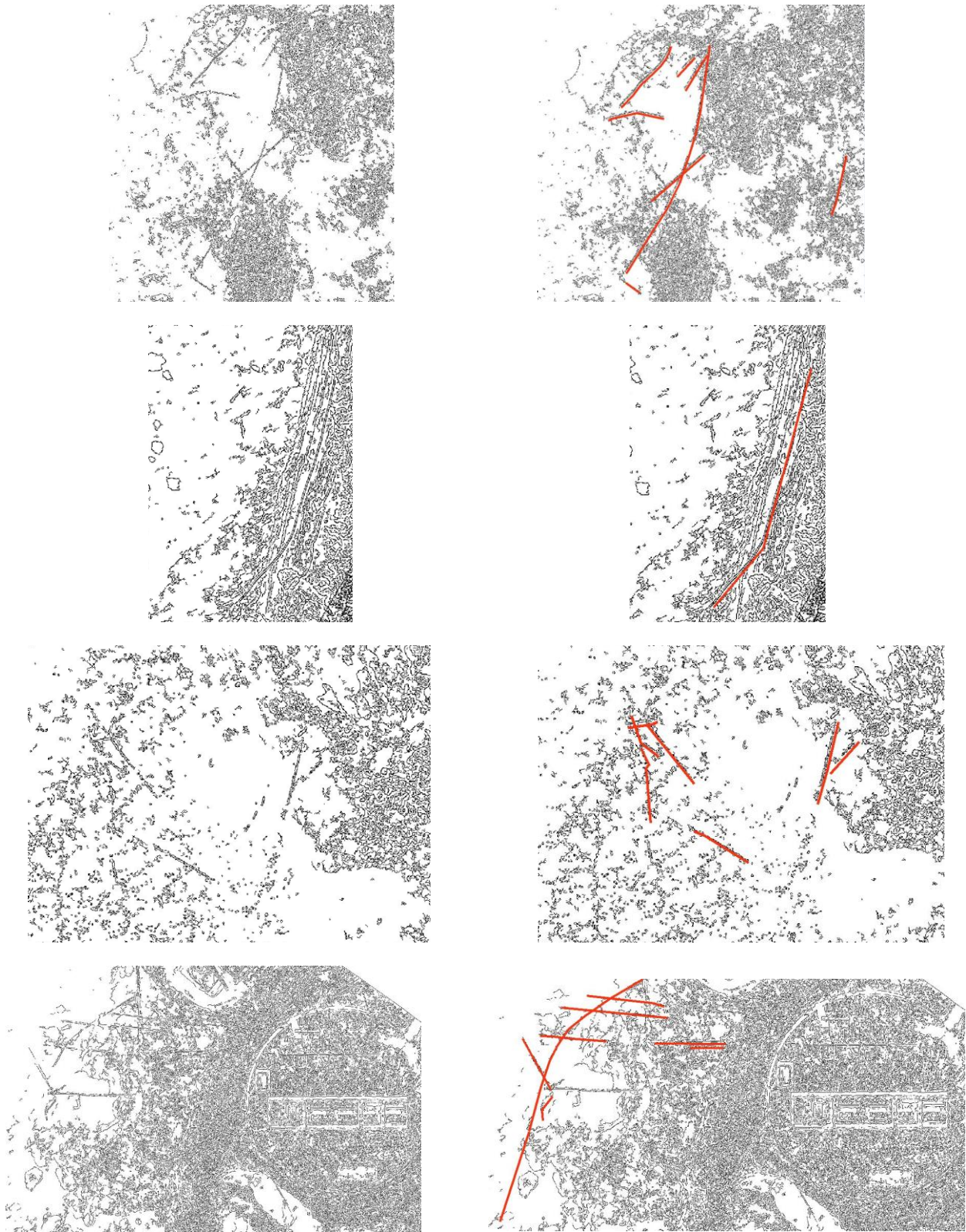


Figure 5.13. The result sample of Canny [1, 1, 3] and ground truth delineated manually

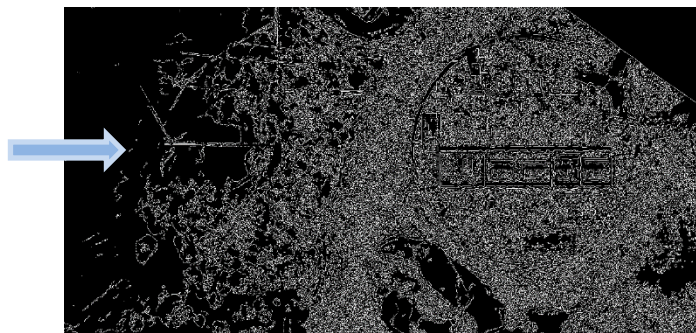
Although Sobel and Prewitt's methods created lower noise in the image, they could not find as many edges as the Canny method did. The result is shown that the output of these methods is generally similar to each other. In spite of the Canny method having more noise in its results, it can detect more edges; many of which are pipelines in this case study. Therefore, neither Sobel nor Prewitt's methods are proper for operation on this data set. The important note is that the parameter values of the Canny method in this study will not necessarily perform well on other data sets. The optimal parameter settings may vary from one data set to another. It depends on many other factors including imagery type, quality, blurring, surface type, etc.

It should be mentioned that the chance of detecting the features in clear water is better than turbid water due to deeper visible light penetration. Glint removal images did not useful for manual delineation of submerged pipelines, because there was no difference in the result. Running an edge detection operator on deglint images shows that in spite of the output having more noise than the output on raw images, it is possible to detect more edges (pipes) in glint corrected images. Deglint imagery was helpful during the edge detection image processing for this data set and resulted in the detection of more edges. By removing glint through the surface of the water, the reflection through the water column and underlying surface structure below became more apparent in the imagery. Therefore, deglint imagery was helpful in edge detection image processing for this data set and resulted in the detection of more edges.

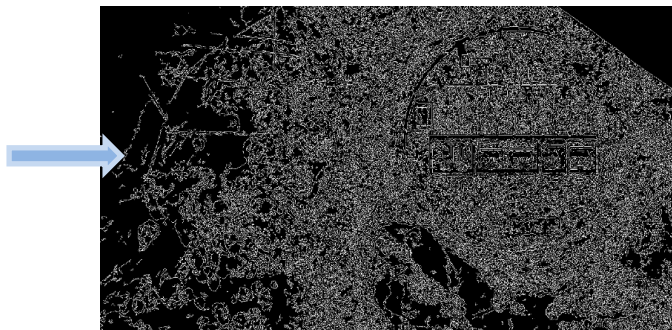
Edge detection algorithms were run over the two sun glint corrected images. Canny operator detected more edges compared to original imagery, while the result did not change for the other operators. Table 5.6 shows the result in terms of number of detected edges in all three methods. The other evaluation parameters did not change. Figure 5.14 is a sample of detected an extra edge by Canny operator.

Table 5.6. Evaluation based on ground truth-deglint imagery

No	Approach	Detected edges (Hedley 2005)	Detected edges (Lyzenga 2006)
1	Canny(1,[1,3])	85 out of 125	85 out of 125
2	Sobel	51 out of 125	50 out of 125
3	Prewitt	50 out of 125	50 out of 125



a) Edge detection (Original Image)



b) Edge detection (glint removal image)

Figure 5.14. Comparing edge detection in original and deglint image sample. The blue arrow shows the location of detected pipe. a) Original image (with glint) b) glint corrected image

5.1.3 UAS-SfM

The last component of this study is assessing the effectiveness of using sun glint correction and single band (red, green, NIR) vs original images and multiband in UAS-SfM photogrammetry. After generating single bands by splitting the multiband, each single band

(NIR, red, and green) is processed to create point cloud using Pix4D. In addition, two methods of sun glint correction are applied to the original images, and then they are processed to produce point clouds using SfM processing. Finally, all results are compared to a point cloud generated from the original imagery. All results are based on the same SfM processing workflow implemented with Pix4D as outlined in the methodology. Table 5.7 shows the results of point cloud density and number of points extracted for each method. The number of points and consequently point density were increased in glint removal methods, red, and green single bands while the point density was decreased in NIR. Table 5.8 indicates the key point matching for each method. Key point matching shows the most points matched in green band compared to all other methods. Two glint removal methods, red and green, have more key point matching amounts compared to original point clouds and NIR.

Table 5.7. Point cloud extraction in UAS-SfM processing

No	Approach	Number of Points	ΔP	Point density	Percentage
1	Original multiband	16,180,268	0	52.360 ppm ²	0
2	Hedley et al. (2005)	16,256,463	76,195	52.438 ppm ²	0.50 %
3	Lyzegna et al. 2006)	16,562,361	382,093	53.257 ppm ²	2.36 %
4	Single band-NIR	12,892,046	-3,288,222	44.443 ppm ²	-20.32 %
5	Single band-red	18,647,020	2,466,752	57.129 ppm ²	15.22 %
6	Single band-green	18,692,357	2,512,089	57.485 ppm ²	15.52 %

(ΔP = each approach – original multiband)

Table 5.8. Key point matching

No	Approach	Key point per image	Matches per calibrate image
1	Original multiband	31105	4621
2	Hedley et al. (2005)	32237	4905
3	Lyzegna et al. 2006)	32932	5233
4	Single band-NIR	29836	3777
5	Single band-red	35599	8163
6	Single band-green	39621	8859

In order to understand how the glint methods affect the UAS-SfM images, a spectral graph is drawn for known sun glint area over the water. The result shows that glint correction

causes the brightness to decrease and because of this, glint falls down dramatically in the glint area in both methods. The brightness value of the Hedley method is lower than the Lyzenga method because of using minimum NIR value in the Hedley method rather than mean NIR in the Lyzenga method (Fig. 5.15).

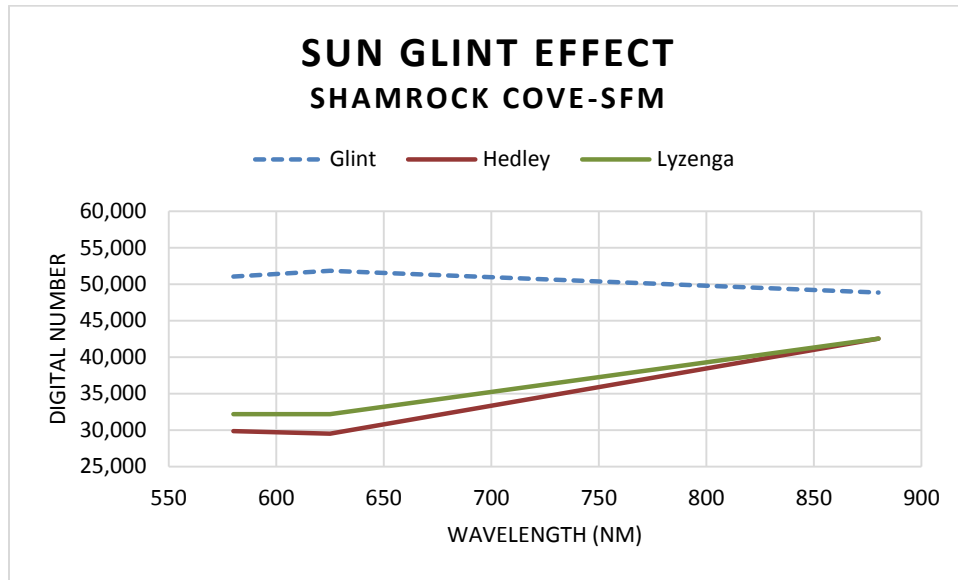


Figure. 5.15 Spectral analysis graph of UAS-SfM images for glint removal methods for the known glint area

Table 5.9 shows the calculation of statistical parameters for all methods over water. ‘Mean z’ of green single band is the lowest between all methods, which means this band can penetrate more in water column. In contrast, ‘mean z’ in glint removal methods changed very little. Therefore, there is no difference between original point cloud and these two methods in terms of penetrating in the water. NIR band has the lowest ‘mean z’, which means it could not penetrate in the water.

Table 5.9. Statistical parameters UAS-SfM product over water (unit: meter)

Water							
No	Statistical parameters	Multiband (Original)	Lyzenga 2006	Hedley 2005	Red	NIR	Green
1	'Min X'	684386.682	684386.670	684386.681	684386.681	684386.670	684386.686
2	'Max X'	684460.301	684460.283	684460.233	684460.300	684460.283	684460.177
3	'Min Y'	3072012.584	3072012.577	3072012.577	3072012.582	3072012.566	3072012.567
4	'Max Y'	3072101.696	3072101.683	3072101.693	3072101.706	3072101.714	3072101.692
5	'Min Z'	-28.489	-28.005	-28.024	-26.036	-25.679	-29.208
6	'Max Z'	-24.654	-24.399	-24.299	-24.285	-24.150	-25.123
7	'Mean X'	684418.179	684420.187	684419.284	684421.297	684421.572	684408.242
8	'Mean Y'	3072055.386	3072057.056	3072056.815	3072058.118	3072058.376	3072048.094
9	'Mean Z'	-26.875	-26.175	-26.375	-25.110	-25.038	-27.655
10	'Mode X'	684388.302	684388.892	684388.503	684428.025	684434.253	684388.092
11	'Mode Y'	3072024.813	3072027.930	3072074.960	3072059.449	3072087.704	3072052.965
12	'Mode Z'	-27.517	-26.654	-26.934	-25.369	-25.309	-28.171
13	'Median X'	684416.475	684419.722	684418.165	684421.351	684421.767	684396.532
14	'Median Y'	3072054.300	3072057.042	3072056.738	3072058.927	3072059.401	3072044.084
15	'Median Z'	-26.959	-26.214	-26.441	-25.134	-25.059	-28.023
16	'Std X'	20.554	19.947	20.103	19.482	19.428	25.671
17	'Std Y'	26.197	25.947	26.057	25.804	25.858	27.067
18	'Std Z'	0.585	0.453	0.502	0.235	0.236	0.802

It should be mentioned that studying the land is not included in the scope of this research. However, running glint algorithms over the land changed pixel values and made unwanted changes. Therefore, when the land is important in a study, it is necessary to create a mask over the land to not run these algorithms in specific areas. Table 5.10 shows these changes for each method in terms of elevation.

Table 5.10. Statistical parameters glint removal vs original multiband point cloud over land (unit: meter)

Land				
No	Statistical parameters	Multiband (Original)	Lyzenga 2006	Hedley 2005
1	'Min Z'	-24.972	-25.494	-25.753
2	'Max Z'	-21.283	-21.387	-18.856
3	'Mean Z'	-23.290	-23.233	-23.124
4	'Mode Z'	-23.132	-23.511	-23.428
5	'Median Z'	-23.302	-23.261	-23.142
6	'Std Z'	0.585	0.523	0.580

As mentioned in methodology, the outliers were removed from the multiband, the Hedley 2005 sun glint removal method, the Lyzenga 2006 method, the green, the red, and the NIR datasets over the water. Figure 5.16 through 5.21 show the distribution of height change in those datasets.

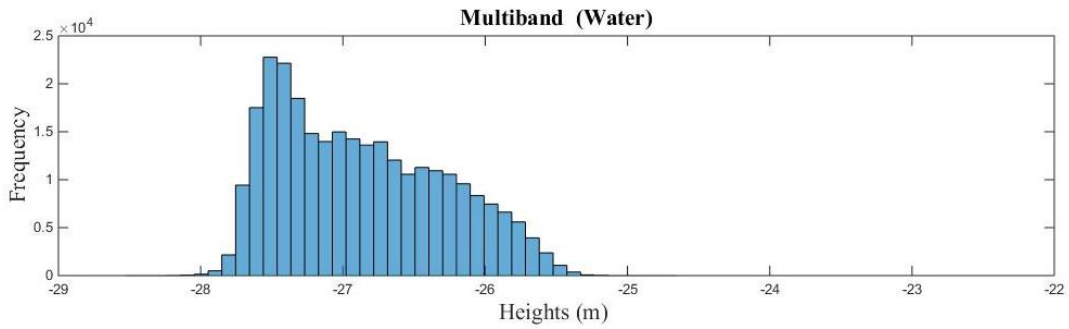


Figure 5.16. Distribution of the original multiband (water)

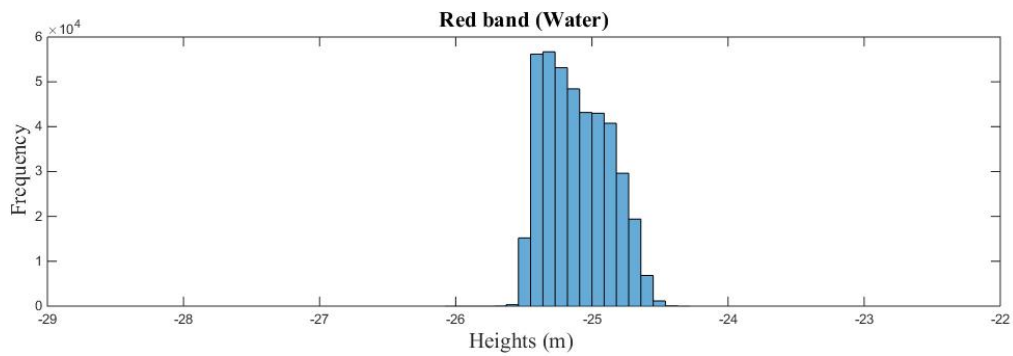


Figure 5.17. Distribution of the red band (water)

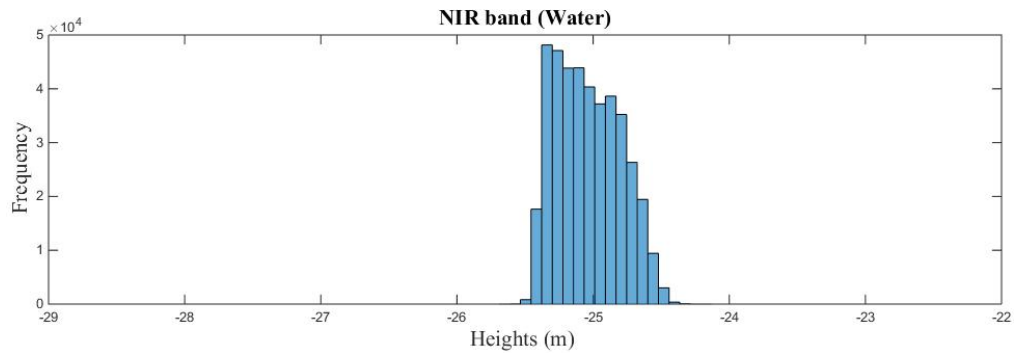


Figure 5.18. Distribution of the NIR band (water)

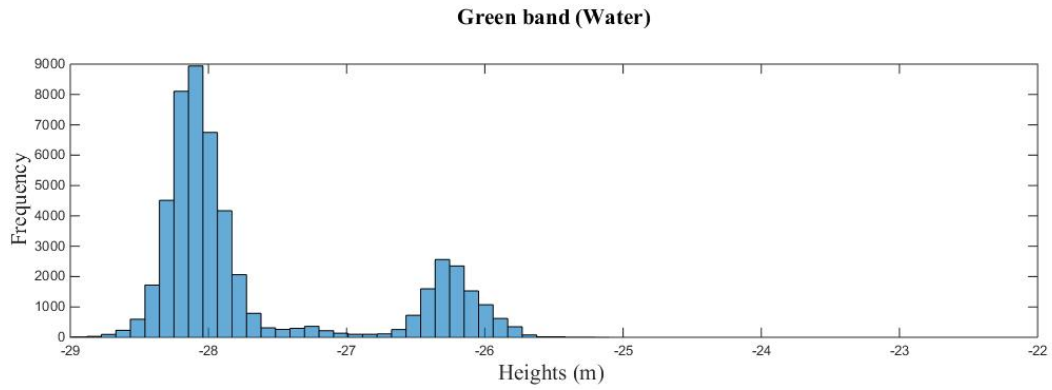


Figure 5.19. Distribution of the green band (water)

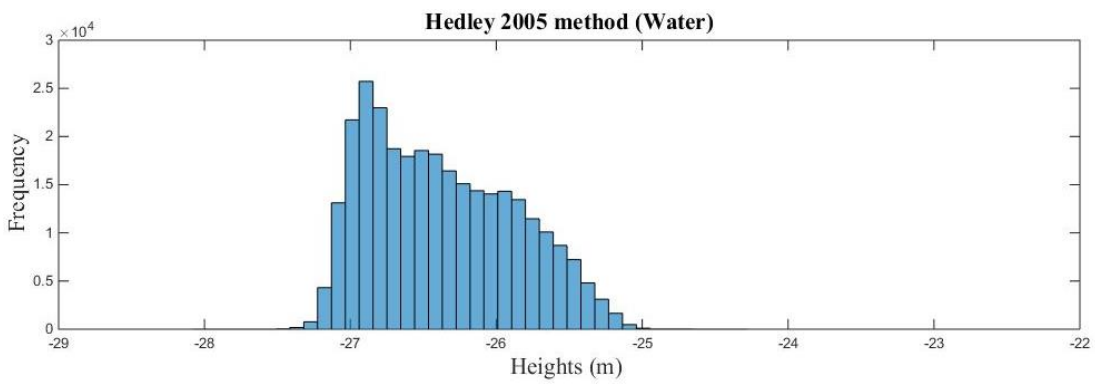


Figure 5.20. Distribution of the Hedley (water)

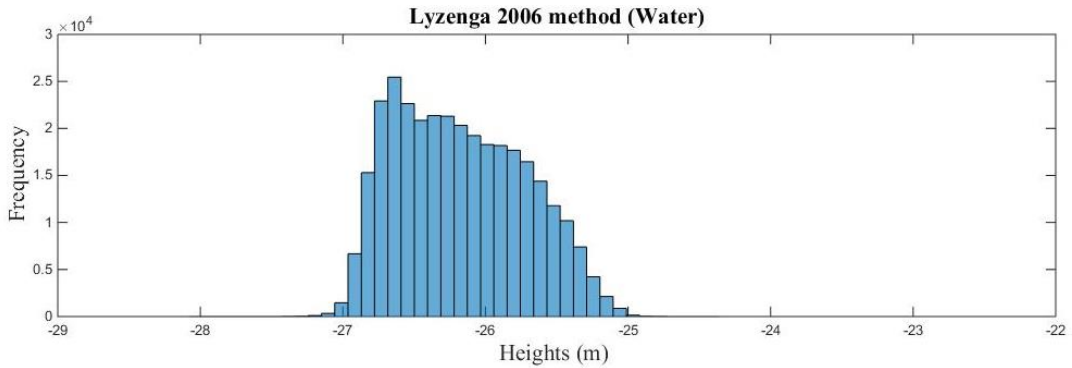


Figure 5.21. Distribution of the Lyzenga (water)

The glint removal methods results showed that number of points increased. There were some gaps in the original multiband (Fig. 5.22) which were filled in the Hedley 2005 and Lyzenga 2006 results (Fig. 5.22 & 5.23).

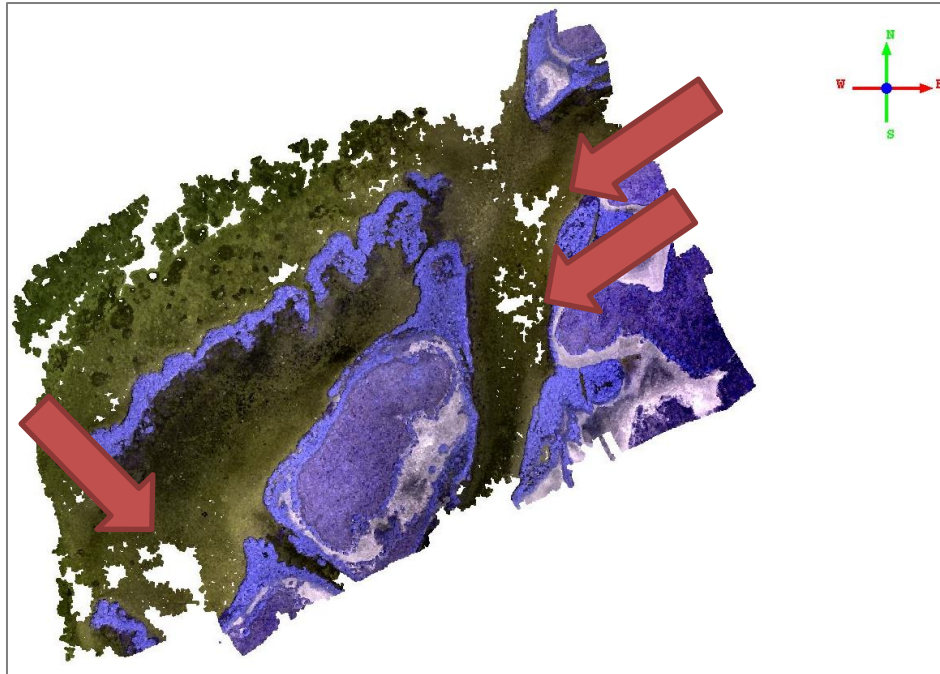


Figure 5.22. Original multiband point cloud; the arrows show the gap area because of glint

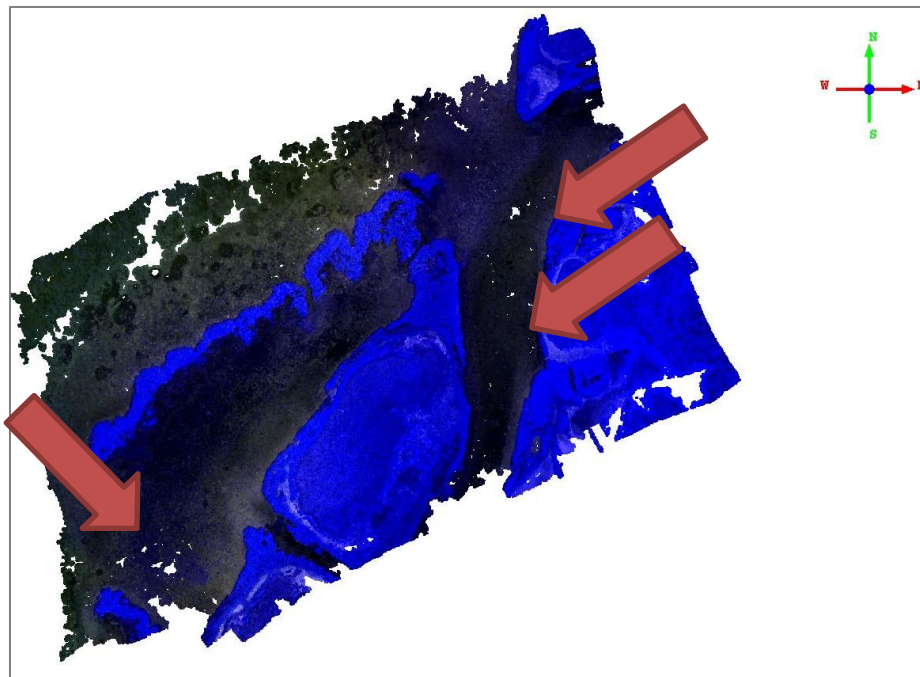


Figure 5.23. Glint corrected_ the Hedley 2005 point cloud; the arrows show the gaps were partially filled by this method

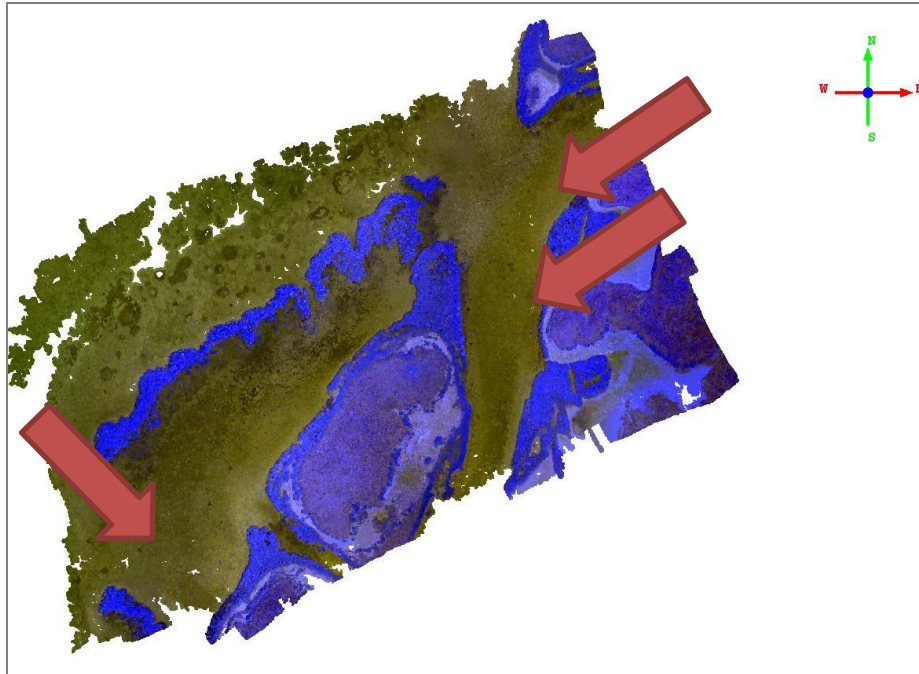


Figure 5.24. Glint corrected_ the Lyzenga 2006- point cloud; the arrows show the gaps were partially filled by this method

Multilevel B-spline interpolation method was used to create DEM from generated point clouds with a cell size of 1 m. Then, shaded relief models from all DEMs were generated with 45° altitude. Shaded reliefs were used for better visualization. Figures 5.25 through 5.30 show the outputs for each data set.

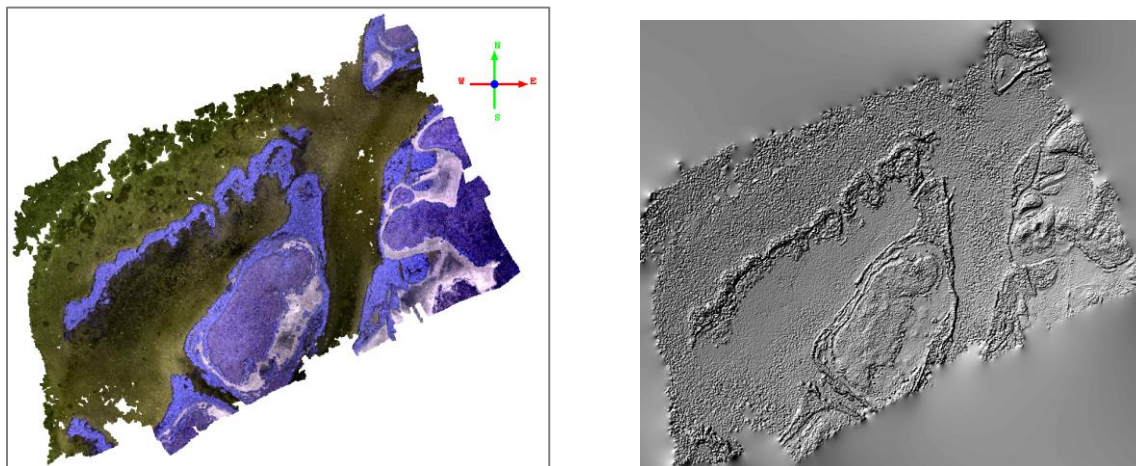


Figure 5.25. Original multiband point cloud and shaded relief

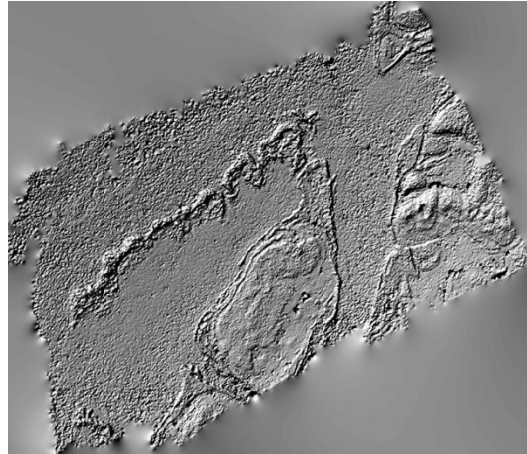
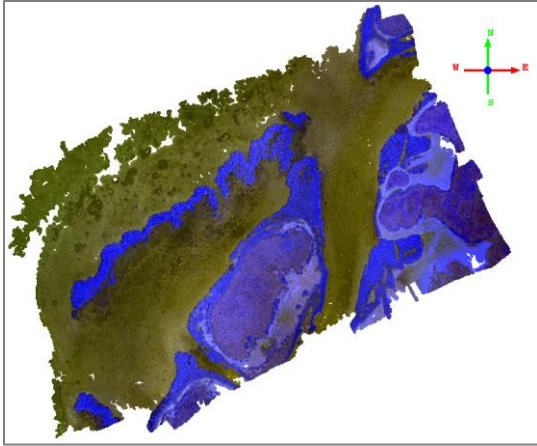


Figure 5.26. Glint corrected_ the Lyzenga 2006- (point cloud and shaded relief)

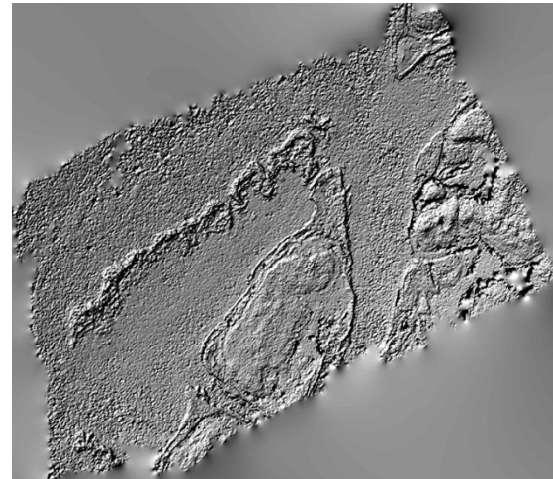
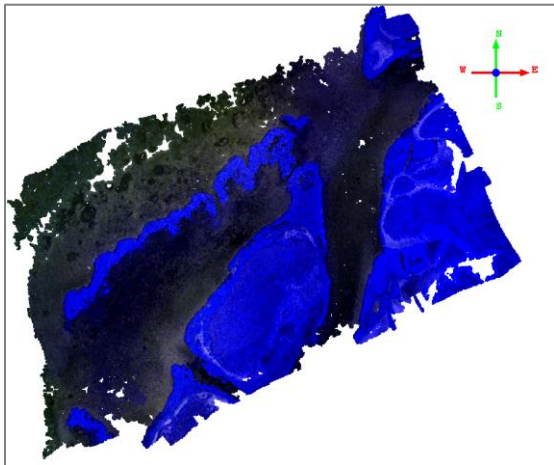


Figure 5.27. Glint corrected_ the Hedley 2005- (point cloud and shaded relief)

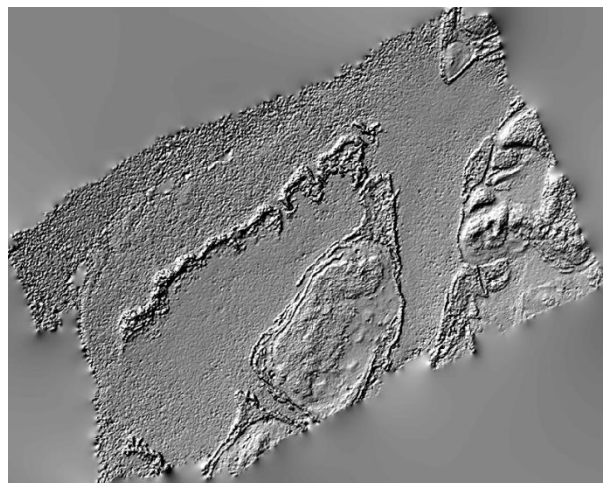
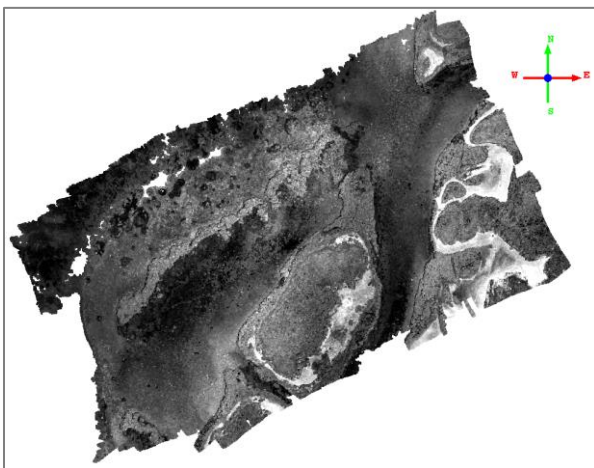


Figure 5.28. Single Band - green- (point cloud and shaded relief)

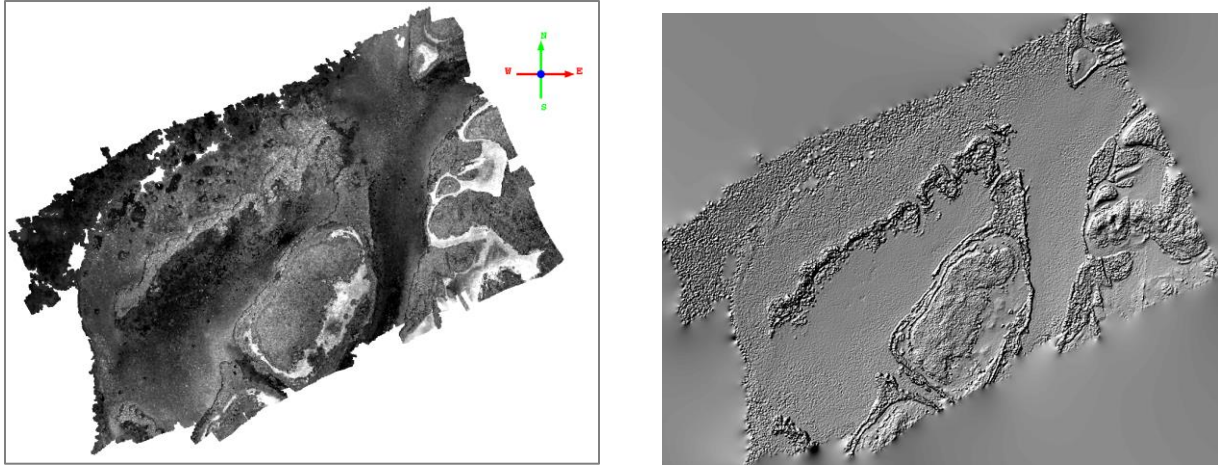


Figure 5.29. Single Band - red- (point cloud and shaded relief)

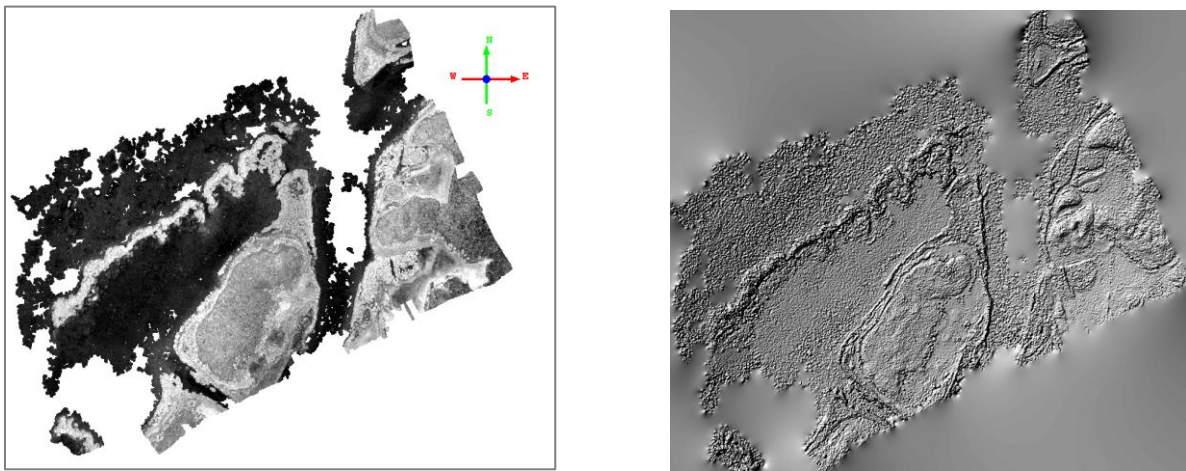
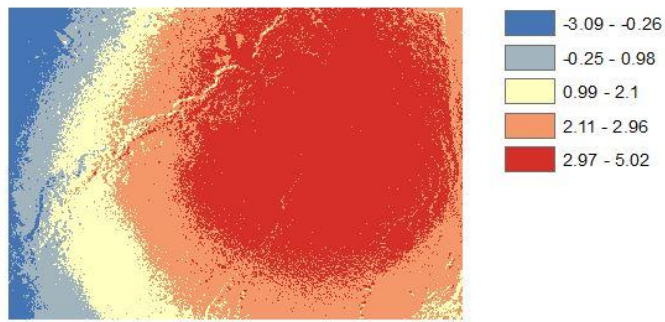


Figure 5.30. Single Band – NIR- (point cloud and shaded relief).

In order to compare DEMs with each other, the point clouds of each data set were clipped (380m x 260m) in water and then DEMs were generated. Multiband original DEM was considered as reference and the others compared to it. In addition, green single band DEM was compared to red and NIR DEMs as well. Green single band was set as reference. For example, in Figure 5.31 (NIR – green) means the green band subtracted from the NIR band. The green band is the base and NIR is compared to it. Positive numbers in the color bar means the reference which is the green band here is higher. Map algebra in ArcGIS was used to perform this step. Figure 5.31 through Figure 5.37 show the results.



MIN	MAX	MEAN	STD
-3.09	5.02	2.37	1.25

Figure 5.31. Comparing DEM results (NIR – Green) – unit: meter



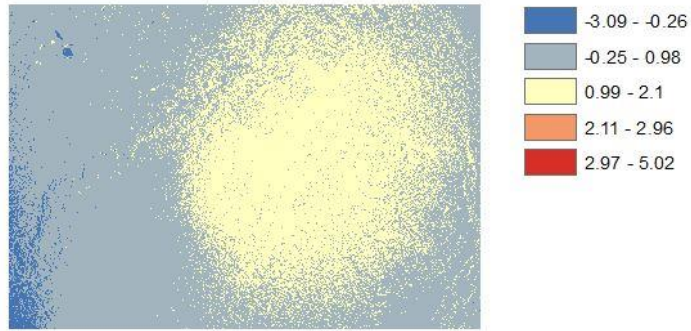
MIN	MAX	MEAN	STD
-2.55	2.12	-0.58	0.42

Figure 5.32. Comparing DEM results (Green – Original multiband) – unit: meter



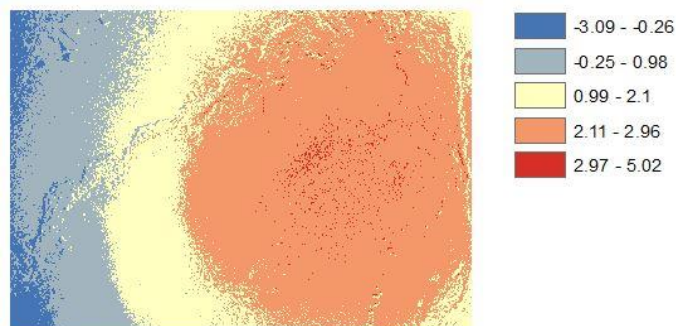
MIN	MAX	MEAN	STD
-1.33	1.84	0.41	0.24

Figure 5.33. Comparing DEM results (Hedley – Original multiband) – unit: meter



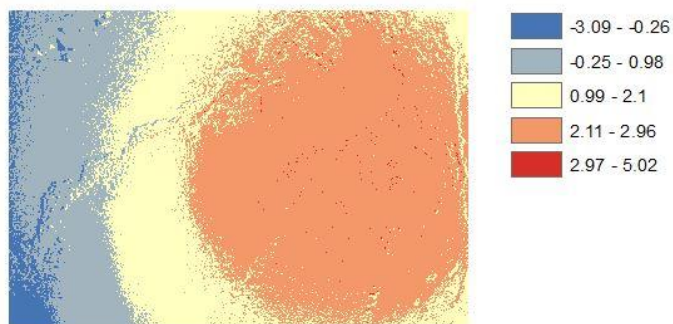
MIN	MAX	MEAN	STD
-1.72	2.56	0.77	0.39

Figure 5.34. Comparing DEM results (Lyzenga – Original multiband) – unit: meter



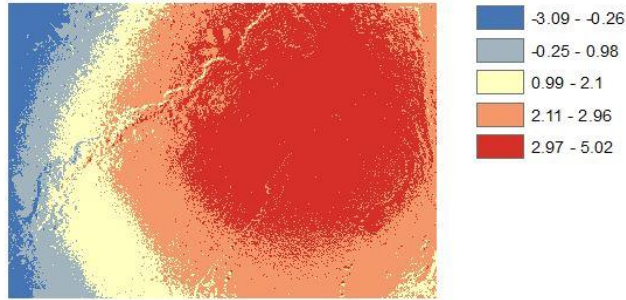
MIN	MAX	MEAN	STD
-1.33	1.84	0.41	0.24

Figure 5.35. Comparing DEM results (NIR – Original multiband) – unit: meter



MIN	MAX	MEAN	STD
-2.20	3.71	1.72	0.95

Figure 5.36. Comparing DEM results (Red – Original multiband) – unit: meter



MIN	MAX	MEAN	STD
-2.81	4.90	2.30	1.21

Figure 5.37. Comparing DEM results (Red – Green) – unit: meter

5.2 Discussion

Based on the results, the outputs showed that four major pipes with 8” to 12” diameter were detected by processing bathymetric lidar data and generating DEMs by B-spline interpolation (red arrows point to the pipes in Fig. 5.24). The TIN method detected 2 pipes and IDW could find only one pipe. Other pipes, which were located near shoreline, were not detected by the lidar approach. Existing features at the level of the pipes, the size of the pipes, and the turbidity of the water can interfere with detecting pipes through DEM. Also, pulse length of the lidar is a limiting factor in resolving water surface from bottom. As water depth becomes shallower the signal from the surface and features on bottom gets convolved reducing discrimination. If some features like sea grass, mud, or reef exist near or at the level of the pipes, there is not enough height difference to be distinguished in the DEM. Small pipes also could not be detected with this data set because of the point density of the lidar data and consequently the resolution of the DEM. The last but not the least important factor is the turbidity of water, which impedes laser penetration through the water column. Edge detection image processing detected more pipes but not the ones in the deep water, because edge detection methods work based on visibility (visible bands). The pipes that were either in deeper water or were not visible due to

high turbidity could not be detected by this approach. Therefore, the visible submerged pipes in the shoreline were detected (blue arrows point to the pipes in Fig. 5.38).

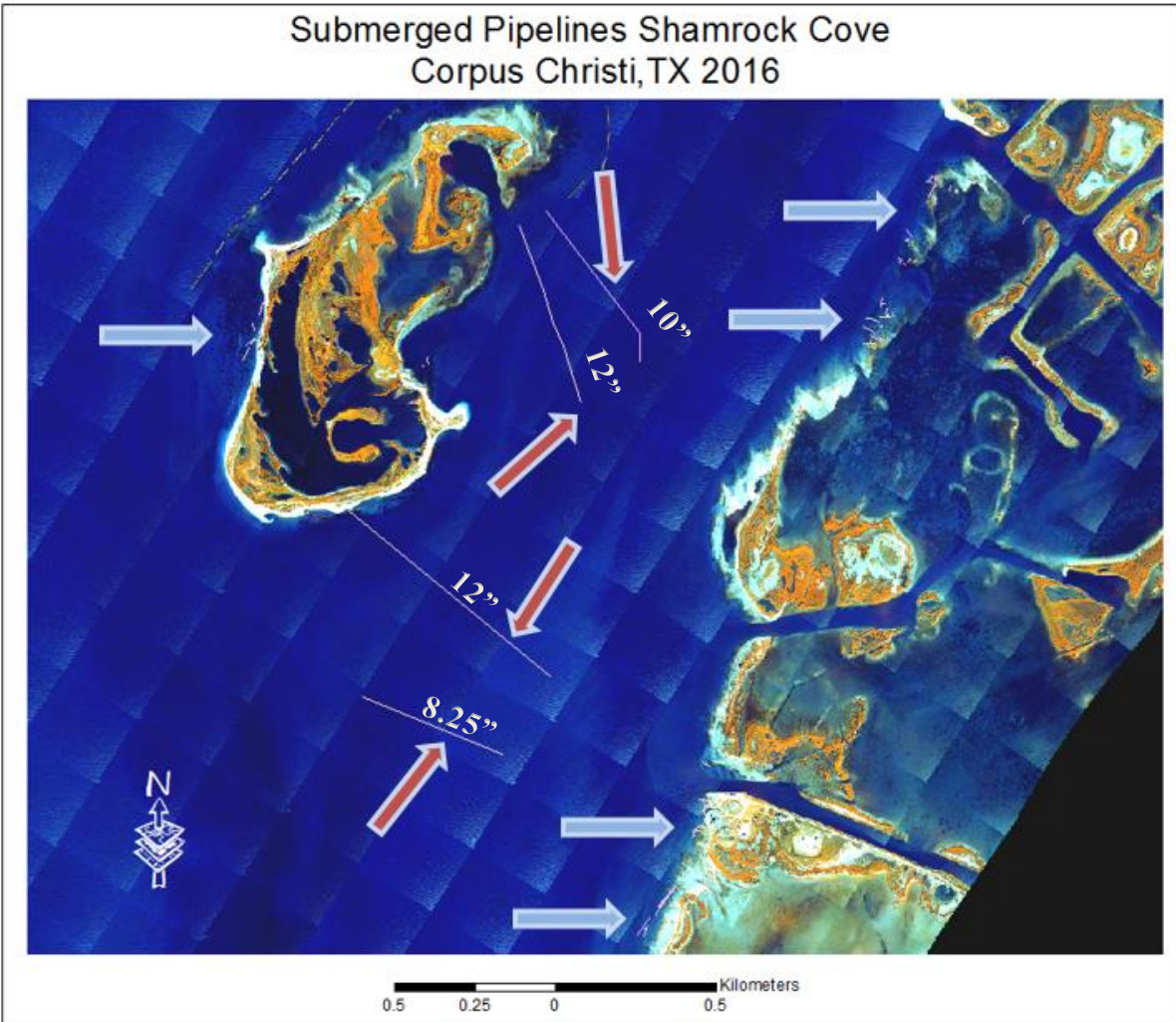


Figure 5.38. Final result, red arrows are detected by DEM and blue arrows are detected by edge detection. The size of the pipelines is provided by GLO agent.

As mentioned above, turbidity of the water is one of the impeding parameters in edge detection methods. The other issue with the edge detection methods discussed in this study, was the existence of noise (unwanted edges) in the output. The existing noise decreased the effectiveness of the edge detection methods. Edge detection methods could perform better if the existing noise was removed in one way or another. Based on the results, the performance of the Canny operator was better than the Sobel and Prewitt methods in terms of detecting the edges.

The bathymetric lidar dataset itself was deemed to be not as useful as anticipated in terms of point cloud filtering to automate pipeline delineation. It is due to inherent limitations in current bathymetric lidar system resolution power when trying to delineate small pipeline structures (e.g. < 6 cm) of size below the laser footprint. Nonetheless, the bathymetric lidar still proved useful in detecting larger submerged pipelines, and in fusion with the aerial imagery proved to be a value added product. One of the other advantages of fusion of lidar and aerial imagery in this study was to cover and complete each other's deficiency.

In this study, two methods were used to remove the sun glint from high resolution aerial imagery, which were the Hedley et al. (2005) and the Lyzenga et al. (2006). These two methods rest on the assumption that all NIR radiation is absorbed by water, and hence the water-leaving radiance shall be zero. The accuracy of that assumption depends on the local conditions; for example in shallow or turbid water NIR radiation may be reflected into the air by the seabed or sediment before absorption. The only difference between the methods of Hedley et al. (2005) and Lyzenga et al. (2006) is how they handled the water-leaving NIR which is required to apply the correction. Based on the result, sun glint removal image preprocessing did not succeed in manually delineating the submerged pipelines as anticipated. However, the results of the Canny method edge detection image processing were improved in terms of detecting more edges after sun glint correction, while in the Sobel and Prewitt methods, the results did not change.

In the last part of this study, UAS-SfM photogrammetry was used to examine the effectiveness of sun glint corrected imagery single band (green, red, NIR) vs original multiband imagery. The results showed that using sun glint correction increased the point density compared to original multiband. The glint removal methods decreased the brightness in the image specifically in the glint area which caused more penetration in water column and consequently

more points extracted. The point density of point clouds extracted by the Lyzenga method data set was higher than the Hedley et al. (2005) method. In terms of key feature matching, the number of key feature matching increased in the sun glint corrected methods compared to multiband original. Therefore, they had a better 3D reconstruction performance compared to original multiband. Feature matching is one of the advantages of SfM photogrammetry compared to conventional photogrammetry.

Based on the statistical parameters which were calculated for the water portion of the study area, the green band between all three single bands (red, green, and NIR) had the lowest amounts in 'mean Z', 'min Z', 'mode Z', and 'median Z'. This happened because the green band is the least absorbed by water and could penetrate deeper in water. Therefore, using only green single band in the processing gave a better estimation of the sea floor. In contrast, NIR band had the highest amounts in 'mean Z', 'min Z', 'mode Z', and 'median Z'. This means that the NIR was absorbed by water and cannot travel deeper in the water.

Results achieved in the DEM comparison showed that the green band stood deeper than the NIR and red bands. Therefore, the green single band had the best depth estimation in all three bands. There is not many differences between the original multiband and the glint removal methods in terms of elevation. Therefore, using sun glint removal methods increased point density without any major affecting on the elevation.

UAS-SfM is a cost effective method due to its platform compared to other aerial approaches. Typically this method is not affected by cloud cover due to lower flight altitudes. Because of generating the point clouds from the imagery, there is no canopy penetration. In contrast, the manned aerial methods contain wide spectral capabilities including lidar. In contrast to manned aerial photogrammetry, UAS-SfM has a small single-flight coverage because of

limitation in flight altitude and duration. So, it is proper for small and medium size projects. UAS-SfM, cannot be replaced by other methods, but it does fill the existing gap between other approaches.

CHAPTER 6

CONCLUSION

This work is an effort to evaluate active and passive airborne surveying techniques for mapping submerged structures in shallow water. Three different airborne surveying techniques including bathymetric lidar, airborne high resolution imagery, and SfM photogrammetry using a small UAS were examined for bathymetric mapping and submerged structure delineation in shallow coastal water. In each category, multiple methods were treated in order to find the optimum method. In the first section, three different interpolation algorithms including IDW, 2D Delaunay TIN, and multilevel B-Spline were used to create a DEM from bathymetric lidar data. In order to assess the vertical accuracy of interpolation methods the RMSE of each algorithm was calculated. The results show that multilevel B-Spline was the most accurate between these three algorithms. In addition, based on visual inspection and ground truth, four main pipelines were extracted from the DEM by the multilevel B-Spline method. In contrast, IDW and 2D Delaunay could show one and two main pipelines, respectively. Other pipelines could not be distinguished in this approach because of their size and their surroundings.

Image enhancement methods including sun glint correction were examined to improve the quality of the imagery in terms of penetrating through the water column. Two main approaches of glint correction were examined, based on NIR reflectance capture. The Hedley et al. (2005) and the Lyzenga et al. (2006) algorithms were described in this study. These methods could correct moderate glint but large errors remained in the brightest glint areas. The glint becomes minimized by using these two methods. There is no unique method that can be applied to all imagery data sets. In other words, a technique which works on one imagery data set may not work on the other. Sun glint correction is an important step in image processing of high

resolution imagery, which minimizes or removes the sun glint effects to derive more accurate water-leaving radiances.

In order to delineate the submerged pipelines, edge detection image processing was applied to the imagery data set. Three different methods were examined on the imagery. Canny method performed better than the Sobel and the Prewitt methods. The edge detection algorithms were run over the glint corrected images. The result showed that the possibility of detecting pipes in the glint corrected images were more than original images.

In the last part of this study, image preconditioning methods including glint correction and single vs. original multiband input were examined on UAS-SfM photogrammetry results over shallow water. The results showed that using sun glint correction methods improved the product of the SfM point cloud in terms of point density and number of points. For example, there were some gaps in the original imagery SfM point cloud which was affected by the sun glint effect. However, these gaps were partially filled after the glint correction algorithm was applied over the images. When single band vs. multiband was examined, the results showed that the green band provided best performance in terms of penetration depth.

Overall, there is not a perfect approach to use for all projects. It is necessary to evaluate different methods in order to find a suitable fit for the particular problem and should be performed in a case-by-case basis.

CHAPTER 7

CHALLENGES AND FUTURE WORK

In the first section of this study, the bathymetric lidar point clouds were examined to perform classification or filtering with the aim to extract the submerged pipelines. The given bathymetric lidar point clouds could not be used to extract submerged pipelines directly in terms of filtering the point cloud, because of low point density in bathymetry and resulting in not enough data to extract submerged pipeline. In addition, due to inherent limitations in current bathymetric lidar system resolution power, it is recommended that future surveys targeted for this objective plan as best as possible for ideal water conditions in terms of visibility, employ more scan overlap, and fly at minimum allowed altitudes with as high a pulse rate as is functional for dense sampling and high signal-to-noise. Development of automated approaches and improved methods to better exploit the bathymetric lidar data for detection of submerged pipelines is a work in progress. For instance, after generating the DSM and DEM of the study area, the normalized DSM ($DSM - DEM$) is extracted and all features including submerged structures and vegetation are separated. Then, some segmentation methods are applied to filter vegetation from submerged structures, like shape features method using some linear characteristic (for example ratio of length to width) which results in a separation of linear features from others. In the last step, another filtering is needed to classify pipelines from other submerged features based on either elevation or connectivity of the features.

It is recommended to examine the Kriging interpolator to create a DEM in order to map the submerged bottom and structures with bathymetric lidar data. Kriging is a statistical spatial interpolation method as opposed to deterministic spatial interpolation, like the methods examined

here, and considered the best linear unbiased estimator (BLUE) in a mean square error sense under certain conditions (Mitas, & Mitasova, 1999).

In terms of assessing the accuracy of the interpolation methods, GPS data were mostly collected on land and few in water. In order to have a better evaluation of their accuracy, it is necessary to provide more control points and observations in the water.

Avoiding sun glint by choosing appropriate place and time for data collection is the best way to deal with sun glint. For example, applying Mount (2005) method helps to determine the time of image acquisition in the calm and rough sea. Mount's method uses sun angle, sensor field of view and wind speed, from which a glint prediction can be made based on a simplified model of the sea surface state. In addition to the sun glint, there are other routes that radiance can reach a remote sensing detector including water-leaving radiance, sky glint, and whitecaps on the water surface (Fig. 7.1). Water-leaving radiance is transmitted through the atmosphere and the air-water interface followed by scattering or reflection below the water surface and transmitted back through the atmosphere to the detector. Sky glint is scattered from the atmosphere to the water surface (not sun) and then reflected to the sensor. These radiance routes may have an effect on the results either airborne imagery or UAS-SfM photogrammetry images in one way or another. Therefore, applying some approaches is desired to remove these effects and then to assess the effectiveness of these corrections on the results.

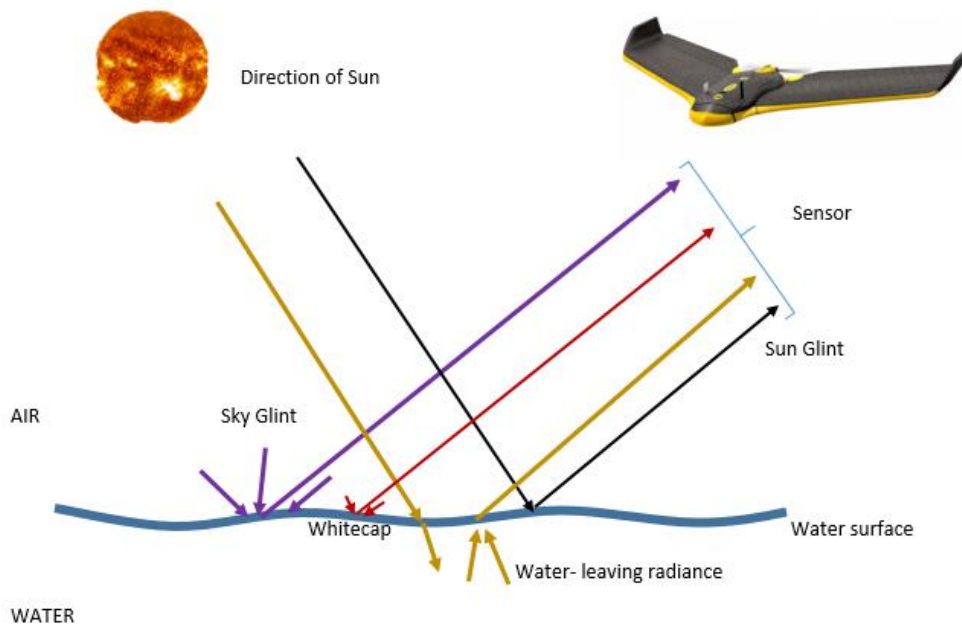


Figure 7.1. Schematic view of rays. It shows different ways of rays can reach a sensor

In future research, it would be interesting to investigate the existing noise or unwanted edges in the product of edge detection. In the output of the edge detection, there is a lot of noise that needs to be removed from the final product to have a clean result. Some approaches should be applied to remove this noise from the product as future work. For example, the images are converted from raster to vector, and then the vector feature classes are classified based on their lengths. In this approach, noise still remains in the final product, but they are fewer than in the original one. However, this approach is not automated and can be time consuming. Noise reduction algorithms including kernel anisotropic diffusion (KAD) (Yu, Wang, and Shen, 2008) and adaptive Gaussian filter (Deng & Cahill, 1993) can be applied and examined to get rid of noise in the final output. In addition, the edge detection methods can be examined to detect breaklines and linear features using a DEM. Intensity is changed by increasing or decreasing the elevation in the DEM. Some elements of generating a DEM can affect an edge detection including type of classification (in terms of either number of class or color), cell size, and slope.

Different setting of these elements should be tested to create a DEM, and then use them in edge detection operators as an input.

NIR camera was used for image acquisition in UAS-SfM photogrammetry section. Although NIR cannot penetrate the water surface, only the two bands red and green could penetrate into the water. In contrast, when a standard RGB camera is used to collect data, three bands can penetrate into the water, green, blue, and red, the former being most penetrating capable and the latter being less penetrating. However, using a standard RGB camera cannot provide the possibility of glint correction via conventional glint removal algorithms due to the need for NIR reflectance. Using a polarized filter on RGB cameras is recommended to assess the sun glint effect in the images. In addition, flight planning including path and direction of flight relative to incoming sun glint, flight height, and wind speed should be examined to reducing the glint.

ACKNOWLEDGEMENT

National Oceanic and Atmospheric Administration (NOAA);

Texas General Land Office (TGLO) and Coastal Management Program (CMP);

TGLO Contract No. 15-050-000-8395.

Views expressed here are the authors' and do not necessarily reflect those of NOAA or TGLO.

REFERENCES

- AAMHatch, 2006. Airborne Laser Scanning Technical Specifications, <http://www.aamhatch.com.au> (accessed 27 Sept. 2006)
- Ackermann, J., Völger, P., & Wiegner, M. (1999). Significance of multiple scattering from tropospheric aerosols for ground-based backscatter lidar measurements. *Applied optics*, 38(24), 5195-5201.
- Basu, M. (2002). Gaussian-based edge-detection methods-a survey. *IEEE Transactions on Systems, Man, and Cybernetics, Part C*, 32(3), 252-260.
- Canny, J. (1986). A computational approach to edge detection. *IEEE Transactions on pattern analysis and machine intelligence*, (6), 679-698.
- Chen, Q. (2007). Airborne lidar data processing and information extraction. *Photogrammetric engineering and remote sensing*, 73(2), 109.
- Chew, L. P. (1989). Constrained delaunay triangulations. *Algorithmica*, 4(1-4), 97-108.
- Cichocinski, P., & Basista, I. (2013). THE COMPARISON OF SPATIAL INTERPOLATION METHODS IN APPLICATION TO THE CONSTRUCTION OF DIGITAL TERRAIN MODELS. *International Multidisciplinary Scientific GeoConference: SGEM: Surveying Geology & mining Ecology Management*, 1, 959.
- Deng, G., & Cahill, L. W. (1993, October). An adaptive Gaussian filter for noise reduction and edge detection. In *Nuclear Science Symposium and Medical Imaging Conference, 1993., 1993 IEEE Conference Record*. (pp. 1615-1619). IEEE.
- Doneus, M., Doneus, N., Briese, C., Pregesbauer, M., Mandlbürger, G., & Verhoeven, G. (2013). Airborne laser bathymetry—detecting and recording submerged archaeological sites from the air. *Journal of Archaeological Science*, 40(4), 2136-2151.

- Doxani, G., Papadopoulou, M., Lafazani, P., Tsakiri-Strati, M., & Mavridou, E. (2013). Sun glint correction of very high spatial resolution images. Thales, in Honor of Prof. Emeritus Michael E. Contadakis, 329-340.
- Eugenio, F., Marcello, J., & Martin, J. (2015). High-Resolution Maps of Bathymetry and Benthic Habitats in Shallow-Water Environments Using Multispectral Remote Sensing Imagery. *Geoscience and Remote Sensing, IEEE Transactions on*, 53(7), 3539-3549.
- Everaerts, J. (2008). The use of unmanned aerial vehicles (UAVs) for remote sensing and mapping. *The International Archives of the Photogrammetry, Remote Sensing and Spatial Information Sciences*, 37, 1187-1192.
- Gao, W., Zhang, X., Yang, L., & Liu, H. (2010, July). An improved Sobel edge detection. In *Computer Science and Information Technology (ICCSIT), 2010 3rd IEEE International Conference on* (Vol. 5, pp. 67-71). IEEE.
- Gatziolis, D., & Andersen, H. E. (2008). A guide to LIDAR data acquisition and processing for the forests of the Pacific Northwest (pp. 1-32). US Department of Agriculture, Forest Service, Pacific Northwest Research Station.
- Guenther, G. C., LaRocque, P. E., & Lillycrop, W. J. (1994, October). Multiple surface channels in Scanning Hydrographic Operational Airborne Lidar Survey (SHOALS) airborne lidar. In *Ocean Optics XII* (pp. 422-430). International Society for Optics and Photonics.
- Guenther, G. C., Cunningham, A. G., LaRocque, P. E., & Reid, D. J. (2000, June). Meeting the accuracy challenge in airborne lidar bathymetry. In *Proceedings of EARSeL-SIG-Workshop LIDAR, Dresden/FRG* (pp. 16-17).
- Giessel J. Z. (2015). *2D and 3D mapping of littoral zone with UAS and Structure from Motion photogrammetry* (master's thesis). Texas A&M University Corpus Christi. viii, 76 p.

- Goodman, J. A., Lee, Z., & Ustin, S. L. (2008). Influence of atmospheric and sea-surface corrections on retrieval of bottom depth and reflectance using a semi-analytical model: a case study in Kaneohe Bay, Hawaii. *Applied Optics*, 47(28), F1-F11.
- Heath, M. D., Sarkar, S., Sanocki, T., & Bowyer, K. W. (1997). A robust visual method for assessing the relative performance of edge-detection algorithms. *Pattern Analysis and Machine Intelligence, IEEE Transactions on*, 19(12), 1338-1359.
- Hedley, J. D., Harborne, A. R., & Mumby, P. J. (2005). Technical note: Simple and robust removal of sun glint for mapping shallow-water benthos. *International Journal of Remote Sensing*, 26(10), 2107-2112.
- Hochberg, E. J., Andrefouet, S., & Tyler, M. R. (2003). Sea surface correction of high spatial resolution Ikonos images to improve bottom mapping in near-shore environments. *IEEE transactions on geoscience and remote sensing*, 41(7), 1724-1729.
- Islam, M. S., Bonner, J. S., Ojo, T. O., & Page, C. (2011). A mobile monitoring system to understand the processes controlling episodic events in Corpus Christi Bay. *Environmental monitoring and assessment*, 175(1-4), 349-366.
- Irish, J. L., & White, T. E. (1998). Coastal engineering applications of high-resolution lidar bathymetry. *Coastal Engineering*, 35(1), 47-71.
- Irish, J. L., & Lillycrop, W. J. (1999). Scanning laser mapping of the coastal zone: the SHOALS system. *ISPRS Journal of Photogrammetry and Remote Sensing*, 54(2), 123-129.
- Jebara, T., Azarbayejani, A., & Pentland, A. (1999). 3D structure from 2D motion. *Signal Processing Magazine, IEEE*, 16(3), 66-84.

- Jupp, D. L. B. (1988, September). Background and extensions to depth of penetration (DOP) mapping in shallow coastal waters. In Proceedings of the Symposium on Remote Sensing of the Coastal Zone (pp. IV-2).
- Kang, C. C., & Wang, W. J. (2007). A novel edge detection method based on the maximizing objective function. *Pattern Recognition*, 40(2), 609-618.
- Kay, S., Hedley, J. D., & Lavender, S. (2009). Sun glint correction of high and low spatial resolution images of aquatic scenes: A review of methods for visible and near-infrared wavelengths. *Remote Sensing*, 1(4), 697-730.
- Khoshelham, K., Nardinocchi, C., Frontoni, E., Mancini, A., & Zingaretti, P. (2010). Performance evaluation of automated approaches to building detection in multi-source aerial data. *ISPRS Journal of Photogrammetry and Remote Sensing*, 65(1), 123-133.
- Klemas, V. (2011). Beach profiling and LIDAR bathymetry: an overview with case studies. *Journal of Coastal Research*, 27(6), 1019-1028.
- Klemas, V. (2013). Remote sensing of emergent and submerged wetlands: an overview. *International journal of remote sensing*, 34(18), 6286-6320.
- Kumpumäki, T., Ruusuvoori, P., Kangasniemi, V., & Lipping, T. (2015). Data-Driven Approach to Benthic Cover Type Classification Using Bathymetric LiDAR Waveform Analysis. *Remote Sensing*, 7(10), 13390-13409.
- LaRocque, P. E., & West, G. R. (1999). Airborne laser hydrography: an introduction. In Proc. ROPME/PERSGA/IHB Workshop on Hydrographic Activities in the ROPME Sea area and Red Sea (Vol. 4, pp. 1-15).
- Leatherman, S.P., 2003. Shoreline Change Mapping and Management Along the U.S. East Coast. *Journal of Coastal Research*, Vol., No. Special Issue 38, pp. 5-13.

- Lee, D. T., & Lin, A. K. (1986). Generalized Delaunay triangulation for planar graphs. *Discrete & Computational Geometry*, 1(3), 201-217.
- Lee, S., Wolberg, G., & Shin, S. Y. (1997). Scattered data interpolation with multilevel B-splines. *IEEE transactions on visualization and computer graphics*, 3(3), 228-244.
- Liu, X. (2008). Airborne LiDAR for DEM generation: some critical issues. *Progress in Physical Geography*, 32(1), 31-49.
- Lowe, D. G. (2004). Distinctive image features from scale-invariant keypoints. *International journal of computer vision*, 60(2), 91-110.
- Lyzenga, D. R. (1978). Passive remote sensing techniques for mapping water depth and bottom features. *Applied optics*, 17(3), 379-383.
- Lyzenga, D. R. (1985). Shallow-water bathymetry using combined lidar and passive multispectral scanner data. *International Journal of Remote Sensing*, 6(1), 115-125.
- Lyzenga, D. R., Malinas, N. P., & Tanis, F. J. (2006). Multispectral bathymetry using a simple physically based algorithm. *IEEE Transactions on Geoscience and Remote Sensing*, 44(8), 2251.
- Mancini, F., Dubbini, M., Gattelli, M., Stecchi, F., Fabbri, S., & Gabbianelli, G. (2013). Using Unmanned Aerial Vehicles (UAV) for high-resolution reconstruction of topography: The structure from motion approach on coastal environments. *Remote Sensing*, 5(12), 6880-6898.
- Mitas, L., & Mitasova, H. (1999). Spatial interpolation. *Geographical information systems: principles, techniques, management and applications*, 1, 481-492.
- Montagna, P. A., and Ritter, C. (2006). "Direct and indirect effects of hypoxia on benthos in Corpus Christi Bay, Texas, USA." *J. Exp. Mar. Biol. Ecol.*, 330(1), 119–131

- Mount, R. (2005). Acquisition of Through-water Aerial Survey Images. *Photogrammetric Engineering & Remote Sensing*, 71(12), 1407-1415.
- Nayegandhi, A., Brock, J. C., & Wright, C. W. (2009). Small-footprint, waveform-resolving lidar estimation of submerged and sub-canopy topography in coastal environments. *International Journal of Remote Sensing*, 30(4), 861-878.
- Padmavathi, G., Muthukumar, M., & Thakur, S. K. (2010, August). Implementation and Comparison of different segmentation algorithms used for underwater images based on nonlinear objective assessments. In *Advanced Computer Theory and Engineering (ICACTE)*, 2010 3rd International Conference on (Vol. 2, pp. V2-393). IEEE.
- Pan, Z., Fernandez-Diaz, J.C., Glennie, C.L., Starek, M. 2014. Comparison of Bathymetry and Seagrass Mapping with Hyperspectral Imagery and Airborne Bathymetric LiDAR in a Shallow Estuarine Environment. *Journal of Selected Topics in Applied Earth Observations and Remote Sensing*, Vol 8.
- Pizarro, O., Eustice, R. M., & Singh, H. (2009). Large area 3-D reconstructions from underwater optical surveys. *Oceanic Engineering, IEEE Journal of*, 34(2), 150-169.
- Quadros, N. D., Collier, P. A., & Fraser, C. S. (2008). Integration of bathymetric and topographic LiDAR: a preliminary investigation. *The International Archives of the Photogrammetry, Remote Sensing and Spatial Information Sciences*, 36, 1299-1304.
- Remondino, F., Barazzetti, L., Nex, F., Scaioni, M., & Sarazzi, D. (2011). UAV photogrammetry for mapping and 3d modeling—current status and future perspectives. *International Archives of the Photogrammetry, Remote Sensing and Spatial Information Sciences*, 38(1), C22.

- Rodríguez-Cuenca, B., & Alonso, M. C. (2014). Semi-automatic detection of swimming pools from aerial high-resolution images and LiDAR data. *Remote Sensing*, 6(4), 2628-2646.
- Rubo Zhang, Jing Liu, "Underwater Image Segmentation with Maximum Entropy based on ParticleSwarm Optimization (PSO)", Proceedings of the First International Multi-Symposiums on Computer and Computational Sciences (IMSCCS'06) published in IEEE societypp.7695-2581-2006
- Seif, A., Salut, M. M., & Marsono, M. N. (2010, November). A hardware architecture of Prewitt edge detection. In *Sustainable Utilization and Development in Engineering and Technology (STUDENT)*, 2010 IEEE Conference on (pp. 99-101). IEEE.
- Sekovski, I., Stecchi, F., Mancini, F., & Del Rio, L. (2014). Image classification methods applied to shoreline extraction on very high-resolution multispectral imagery. *International Journal of Remote Sensing*, 35(10), 3556-3578.
- Shafait, F., Keysers, D., & Breuel, T. M. (2008, January). Efficient implementation of local adaptive thresholding techniques using integral images. In *Electronic Imaging 2008* (pp. 681510-681510). International Society for Optics and Photonics.
- Shrivakshan, G. T., & Chandrasekar, C. (2012). A comparison of various edge detection techniques used in image processing. *IJCSI International Journal of Computer Science Issues*, 9(5), 272-276.
- Siebert, S., & Teizer, J. (2014). Mobile 3D mapping for surveying earthwork projects using an Unmanned Aerial Vehicle (UAV) system. *Automation in Construction*, 41, 1-14.
- Simms, A. R., Anderson, J. B., Rodriguez, A. B., & Taviani, M. (2008). Mechanisms controlling environmental changes within an estuary: Corpus Christi Bay, Texas. In J. B. Anderson

- & A. B. Rodriguez (Eds.), Response of upper gulf coast estuaries to Holocene climate change and sea-level rise (GSA Special Paper, Vol. 443, pp. 121–146).
- Snavely, N., Seitz, S. M., & Szeliski, R. (2008). Modeling the world from internet photo collections. *International Journal of Computer Vision*, 80(2), 189-210.
- Strickland, R. N., & Chang, D. K. (1990, September). Adaptable edge quality metric. In *Lausanne-DL tentative* (pp. 982-995). International Society for Optics and Photonics.
- Su, H., Liu, H., & Heyman, W. D. (2008). Automated derivation of bathymetric information from multi-spectral satellite imagery using a non-linear inversion model. *Marine Geodesy*, 31(4), 281-298.
- Tamari, S., Mory, J., & Guerrero-Meza, V. (2011). Testing a near-infrared Lidar mounted with a large incidence angle to monitor the water level of turbid reservoirs. *ISPRS Journal of Photogrammetry and Remote Sensing*, 66(6), S85-S91.
- Tan, H. L., Gelfand, S. B., & Delp, E. J. (1989). A comparative cost function approach to edge detection. *IEEE Transactions on Systems, Man, and Cybernetics*, 19(6), 1337-1349.
- Vahtmäe, E., & Kutser, T. (2007). Mapping bottom type and water depth in shallow coastal waters with satellite remote sensing. *J. Coast. Res*, 50, 185-189.
- Vala, M. H. J., & Baxi, A. (2013). A review on Otsu image segmentation algorithm. *International Journal of Advanced Research in Computer Engineering & Technology*, 2(2), 387-389.
- Wang, C. K., & Philpot, W. D. (2007). Using airborne bathymetric lidar to detect bottom type variation in shallow waters. *Remote Sensing of Environment*, 106(1), 123-135.
- Wedding, L. M., Friedlander, A. M., McGranaghan, M., Yost, R. S., & Monaco, M. E. (2008). Using bathymetric lidar to define nearshore benthic habitat complexity: Implications for

- management of reef fish assemblages in Hawaii. *Remote Sensing of Environment*, 112(11), 4159-4165.
- Westoby, M. J., Brasington, J., Glasser, N. F., Hambrey, M. J., & Reynolds, J. M. (2012). 'Structure-from-Motion' photogrammetry: A low-cost, effective tool for geoscience applications. *Geomorphology*, 179, 300-314
- Wolf, P. R., & Dewitt, B. A. (2000). *Elements of Photogrammetry: with applications in GIS* (Vol. 3). New York: McGraw-Hill.
- Woodget, A. S., Carbonneau, P. E., Visser, F., & Maddock, I. P. (2015). Quantifying submerged fluvial topography using hyperspatial resolution UAS imagery and structure from motion photogrammetry. *Earth Surface Processes and Landforms*, 40(1), 47-64.
- Wozencraft, J., & Millar, D. (2005). Airborne lidar and integrated technologies for coastal mapping and nautical charting. *Marine Technology Society Journal*, 39(3), 27-35.
- Ying-Dong, Q., Cheng-Song, C., San-Ben, C., & Jin-Quan, L. (2005). A fast subpixel edge detection method using Sobel–Zernike moments operator. *Image and Vision Computing*, 23(1), 11-17.
- Yu, J., Wang, Y., & Shen, Y. (2008). Noise reduction and edge detection via kernel anisotropic diffusion. *Pattern Recognition Letters*, 29(10), 1496-1503.
- Zhang, R., & Liu, J. (2006, June). Underwater image segmentation with maximum entropy based on Particle Swarm Optimization (PSO). In *Computer and Computational Sciences, 2006. IMSCCS'06. First International Multi-Symposiums on* (Vol. 2, pp. 360-636). IEEE.
- Zhang, S. H., Qu, X. W., Ma, S. J., Yang, Z. R., & Kong, L. F. (2012). A dense stereo matching algorithm based on triangulation. *Journal of Computational Information Systems*, 8, 283-292.

APPENDIX 1

```
% % % % % % % % % TEXAS A&M UNIVERSITY- CORPUS CHRISTI % % % % % % % % %  
% % % % % % % % % % % % % % % % % % % % % % % % % % % % % % % % % % % % % %  
% % % % % % % % % % % % % % % % % % % % % % % % % % % % % % % % % % % % % %  
% % % % % % % % % % % % % % % % % % % % % % % % % % % % % % % % % % % % % %
```

```
% read the image file  
function rasterGlint(path, filename)  
rgbtif=imread([path '\img\' filename '.jpg']);  
% split the image to its components  
nir=rgbtif(:,:,1);  
green=rgbtif(:,:,3);  
red=rgbtif(:,:,2);  
clear rgbtif  
  
% convert float to double  
redd=double(red);  
nird=double(nir);  
greend=double(green);  
% set zero for no data  
nogreendata=greend==0;  
noreddata=redd==0;  
% calculate the regression between NIR and red band  
rednirlm=fitlm(nird(~noreddata),redd(~noreddata));  
% choose the coefficient  
biR=rednirlm.Coefficients.Estimate(2);  
% find the minimum NIR value in the image  
minir=min(nird(~noreddata));  
% calculate the amount of glint in red band  
nredd=redd-biR.*(nird-minir);  
% convert to 16 bit  
intnred=int16(nredd);  
  
% same process for green band  
greennirlm=fitlm(nird(~nogreendata),greend(~nogreendata));  
  
biG=greennirlm.Coefficients.Estimate(2);  
minir=min(nird(~nogreendata));  
  
ngreend=greend-biG.*(nird-minir);  
intngreen=int16(ngreend);  
  
% define matrix for out put  
newraster1=uint16(zeros(x,y));
```

```

newraster2=uint16(zeros(x,y));

newraster3=uint16(zeros(x,y));

newraster=uint16(zeros(x,y,3));

newraster1(~noreddata)=nird(~noreddata);
newraster2(~noreddata)=intnred(~noreddata);
newraster3(~nogreendata)=intngreen(~nogreendata);

% mix three band
newraster(:,1)=newraster1;
newraster(:,2)=newraster2;
newraster(:,3)=newraster3;
%
% define output path and write the image
out= [path '\Deglint_SfM\ filename '.jpg'];
imwrite(newraster,out,'jpg');
end

%%%%%%%%%TEXAS A&M UNIVERSITY CORPUS CHRISTI%%%%%%%%%
%%%%%%%%% SINGLE BAND SPLITING%%%%%%%%%
%%%%%%%%%      BEHROKH NAZERI      %%%%%%%%%%

function SingleBandSfM(path, filename)
rgbtif=imread([path filename]);

nir=rgbtif(:,3);
green=rgbtif(:,2);
red=rgbtif(:,1);
clear rgbtif

newraster=red;
out= [path '\Band1_SfM\ filename ];
%imwrite(newraster,out,'jpg','BitDepth',8);
imwrite(newraster,out,'tif');
end

```

```

%% TEXAS A&M UNIVERSITY CORPUS CHRISTI
%% Edge detection
%% BEHROKH NAZERI
a= imread('C:\Users\bnazeri\Documents\Projects\Shamrock\DataIn\raw images\shamrock-
selected\dir01\1434.tif');
%% bw1=edge(a);
subplot(2,2,1);imshow(a);title('input image');
b=rgb2gray(a);
c= edge(b,'canny');
subplot(2,2,2);imshow(c);title('Canny');
d= edge(b,'sobel');
subplot(2,2,3);imshow(d);title('Sobel');
e= edge(b,'prewitt');
subplot(2,2,4);imshow(e);title('prewitt');
f= edge(b,'log');
imwrite(d,'C:\Users\bnazeri\Documents\Projects\Shamrock\thesis\Imagery\Edge
Detection\SobelImages\1434sobel.tif','tif');
imwrite(e,'C:\Users\bnazeri\Documents\Projects\Shamrock\thesis\Imagery\Edge
Detection\prewittImages\1434prewitt.tif','tif');
%imwrite(e,'C:\Users\bnazeri\Documents\Projects\Shamrock\thesis\Imagery\Edge
Detection\LOGImages\G1434LOG_5.tif','tif');

```

```

%% Canny

```

```

sig = 3;
mLow = .5;
mHigh = 1;

```

```

img = imread('C:\Users\bnazeri\Documents\Projects\Shamrock\DataIn\raw images\shamrock-
selected\dir01\1434.tif');

```

```

if (ndims(img)==3)
    img =double(rgb2gray(img));
end

```

```

dG=dgauss(sig);

```

```

[dummy, filterLen] = size(dG);
offset = (filterLen-1)/2;

```

```

sy = conv2(img, dG , 'same');

```

```

sx = conv2(img, dG, 'same');

[m, n]=size(img);

% crop off the boundary parts...the places where the convolution was partial
sx = sx(offset+1:m-offset, offset+1:n-offset);
sy = sy(offset+1:m-offset, offset+1:n-offset);

% norm of gradient
sNorm = sqrt( sx.^2 + sy.^2 );

% direction of gradient
sAngle = atan2( sy, sx ) * (180.0/pi);

% handle divide by zero....
sx(sx==0) = 1e-10;
sSlope = abs(sy ./ sx);

% sAorig = sAngle;

% for us, x and x-pi are the same....
y = sAngle < 0;
sAngle = sAngle + 180*y;

% bin the angles into 4 principal directions
% 0-45 45-90 90-135 135-180

binDist = [-inf 45 90 135 inf];

[dummy, b] = histc(sAngle, binDist);

sDiscreteAngles = b;
[m, n] = size(sDiscreteAngles);

% each pixel is set to either 1,2,3 or 4
% set the boundary pixels to 0, so we don't count them in analysis...
sDiscreteAngles(1,:) = 0;
sDiscreteAngles(end,:) = 0;
sDiscreteAngles(:,1) = 0;
sDiscreteAngles(:,end) = 0;

sEdgepoints = zeros(m,n);

sFinal = sEdgepoints;

lowT = mLow * mean(sNorm(:));

```

```

highT = mHigh * lowT;

thresh = [ lowT highT];

gradDir = 1;
indxS = find(sDiscreteAngles == gradDir);
slp = sSlope(indxs);

gDiff1 = slp.*(sNorm(indxs)-sNorm(indxs+m+1)) + (1-slp).*(sNorm(indxs)-sNorm(indxs+1));

% interpolate between (-1,-1) and (-1,0)
% gDiff2 = Gy/Gx*(magtd(0,0) - magtd(-1,-1)) + (1- Gy/Gx)*(magtd(0,0)-magtd(-1,0))
gDiff2 = slp.*(sNorm(indxs)-sNorm(indxs-m-1)) + (1-slp).*(sNorm(indxs)-sNorm(indxs-1));

okIndxs = indxS( gDiff1 >=0 & gDiff2 >= 0);
sEdgepoints(okIndxs) = 1;

% gradient direction: 45-90 i.e. gradDir =2
gradDir = 2;
indxS = find(sDiscreteAngles == gradDir);
invSlp = 1 ./ sSlope(indxs);
% interpolate between (1,1) and (0,1)
% gDiff1 = (Gx/Gy)*(magtd(0,0) - magtd(1,1)) + (1- Gx/Gy)*(magtd(0,0)-magtd(0,1))
gDiff1 = invSlp.*(sNorm(indxs)-sNorm(indxs+m+1)) + (1-invSlp).*(sNorm(indxs)-
sNorm(indxs+m));

% interpolate between (-1,-1) and (0,-1)
% gDiff2 = (Gx/Gy)*(magtd(0,0) - magtd(-1,-1)) + (1- Gx/Gy)*(magtd(0,0)-magtd(0,-1))
gDiff2 = invSlp.*(sNorm(indxs)-sNorm(indxs-m-1)) + (1-invSlp).*(sNorm(indxs)-
sNorm(indxs-m));

okIndxs = indxS( gDiff1 >=0 & gDiff2 >= 0);
sEdgepoints(okIndxs) = 1;

% gradient direction: 90-135 i.e. gradDir =3
gradDir = 3;
indxS = find(sDiscreteAngles == gradDir);
invSlp = 1 ./ sSlope(indxs);

% interpolate between (-1,1) and (0,1)
% gDiff1 = (Gx/Gy)*(magtd(0,0) - magtd(-1,1)) + (1- Gx/Gy)*(magtd(0,0)-magtd(0,1))
gDiff1 = invSlp.*(sNorm(indxs)-sNorm(indxs+m-1)) + (1-invSlp).*(sNorm(indxs)-
sNorm(indxs+m));

% interpolate between (1,-1) and (0,-1)

```

```

% gDiff2 = (Gx/Gy)*(magtd(0,0) - magtd(1,-1)) + (1 - Gx/Gy)*(magtd(0,0)-magtd(0,-1))
gDiff2 = invSlp.*(sNorm(indxs)-sNorm(indxs-m+1)) + (1-invSlp).*(sNorm(indxs)-
sNorm(indxs-m));

okIndxs = indxs( gDiff1 >=0 & gDiff2 >= 0);
sEdgepoints(okIndxs) = 1;

% gradient direction: 135-180 i.e. gradDir =4
gradDir = 4;
indxs = find(sDiscreteAngles == gradDir);
slp = sSlope(indxs);

% interpolate between (-1,1) and (-1,0)
% gDiff1 = Gy/Gx*(magtd(0,0) - magtd(-1,1)) + (1 - Gy/Gx)*(magtd(0,0)-magtd(-1,0))
gDiff1 = slp.*(sNorm(indxs)-sNorm(indxs+m-1)) + (1-slp).*(sNorm(indxs)-sNorm(indxs-1));

% interpolate between (1,-1) and (1,0)
% gDiff2 = Gy/Gx*(magtd(0,0)-magtd(1,-1)) + (1 - Gy/Gx)*(magtd(0,0)-magtd(1,0))
gDiff2 = slp.*(sNorm(indxs)-sNorm(indxs-m+1)) + (1-slp).*(sNorm(indxs)-sNorm(indxs+1));

okIndxs = indxs( gDiff1 >=0 & gDiff2 >= 0);
sEdgepoints(okIndxs) = 1;

%HYSTERESIS PART...

sEdgepoints = sEdgepoints*0.6;
x = find(sEdgepoints > 0 & sNorm < lowT);
sEdgepoints(x)=0;
x = find(sEdgepoints > 0 & sNorm >= highT);
sEdgepoints(x)=1;

%sFinal(sEdgepoints>0)=1;

oldx = [];
x = find(sEdgepoints==1);
while (size(oldx,1) ~= size(x,1))
    oldx = x;
    v = [x+m+1, x+m, x+m-1, x-1, x-m-1, x-m, x-m+1, x+1];
    sEdgepoints(v) = 0.4 + sEdgepoints(v);
    y = find(sEdgepoints==0.4);
    sEdgepoints(y) = 0;
    y = find(sEdgepoints>=1);

```

```
sEdgepoints(y)=1;
x = find(sEdgepoints==1);
end

x = find(sEdgepoints==1);

sFinal(x)=1;

figure(1);
imagesc(sFinal); colormap(gray); axis image;
imwrite(sFinal,'C:\Users\bnazeri\Documents\Projects\Shamrock\thesis\Imagery\Edge
Detection\CannyImages\Canny_Threshold\1434Canny_3_.5_1.tif','tif');
```